EVALUATION OF DOUBLE-MOMENT REPRESENTATION OF WARM-RAIN AND ICE HYDROMETEORS IN BULK MICROPHYSICAL PARAMETERIZATION

by

Chao Lin

A thesis submitted to the faculty of
The University of Utah
in partial fulfillment of the requirements for the degree of

Master of Science

Department of Atmospheric Sciences

The University of Utah

December 2014

The University of Utah Graduate School

STATEMENT OF THESIS APPROVAL

The thesis of **Chao Lin**

has been approved by the following supervisory committee members:

Zhaoxia Pu	, Chair	**07/14/2014** Date Approved
Steven K. Krueger	, Member	**07/14/2014** Date Approved
Gerald G. Mace	, Member	**07/14/2014** Date Approved

and by **Kevin D. Perry** , Chair/Dean of

the Department/College/School of **Atmospheric Sciences**

and by David B. Kieda, Dean of The Graduate School.

ABSTRACT

The influence of double-moment representations of warm-rain and ice hydrometeors on the numerical simulations of a Mesoscale Convective System (MCS) over the Southern Great Plains (SGP) during the Midlatitude Continental Convective Clouds Experiment (MC3E) has been investigated. The Weather Research and Forecasting (WRF) model is used to examine the sensitivity of numerical simulations of a MCS to three different microphysical schemes, including the WRF single-moment 6-class (WSM6), WRF double-moment 6-class (WDM6), and Morrison double-moment (MORR) schemes. Simulations are validated with surface Mesonet, the National Centers for Environmental Prediction (NCEP) Stage IV rainfall dataset, Next Generation Radar (NEXRAD), and University of North Dakota (UND)-Citation aircraft observations. A cloud classification algorithm is also applied for evaluating the simulated MCS structures.

It is found that the simulated structure, lifecycle, cloud coverage, precipitation, and microphysical properties of the convective systems, as well as their associated cold pools, are sensitive to microphysical schemes. Compared with the NCEP Stage IV rainfall and NEXRAD observations, the WDM6 simulation produces the structure and extent of the MCS very well, while WSM6 produces a less organized convection structure with a shorter lifetime. Both simulations heavily underestimate the precipitation amount and the radar echo top and have unrealistic cloud component ratios. With MORR

schemes, the model performs well in predicting the lifetime, cloud coverage, echo top, and precipitation.

The differences in the convection properties among the simulations occur mainly because the double-moment representations of warm-rain and ice hydrometeors have a strong influence on convective cloud properties that determine the hydrometeor drag and cold pool characteristics, in terms of intensity, size, and depth.

In contrast, the comparison between simulated microphysical properties and UND-Citation observations illustrates that double-moment representations of ice hydrometeors (MORR) do not improve the prediction of the ice hydrometeor properties, suggesting that uncertainties in microphysical schemes could still be a productive area of future research.

CONTENTS

ACKNOWLEDGEMENTS

I would like to thank my advisor, Dr. Zhaoxia Pu, for her guidance, support, and a lot of help during this study. I also would like to thank my committee members, Dr. Gerald Mace and Dr. Steve Krueger, for their valuable comments.

All the people in the Department of Atmospheric Sciences, especially my colleagues Shixuan and Jianjun, are greatly acknowledged for their friendship. More importantly, my family and friends in China have been very supportive during my study.

I am grateful to the National Center for Atmospheric Research (NCAR) Weather Research and Forecasting (WRF) model development group for their efforts that made the community model available. The computing support from the Center for High Performance Computing (CHPC) at the University of Utah is also greatly acknowledged.

Oklahoma Mesonet data were obtained from the Atmospheric Radiation Measurement (ARM) Program sponsored by the U.S. Department of Energy, Office of Science, Office of Biological and Environmental Research, Climate and Environmental Sciences Division.

This study is supported by the Office of Science (BER), U.S. Department of Energy Grant No. DE-SC0007060 (Principal Investigator: Dr. Zhaoxia Pu).

CHAPTER 1

INTRODUCTION AND BACKGROUND

1.1 Mesoscale Convective Systems

Mesoscale convective systems (MCSs) are thunderstorm regions, which may be round or linear in shape, on the order of 100 kilometers or more across in one direction but smaller than extratropical cyclones. MCSs are important for regional and global precipitation and water cycles. They are also an important link between atmospheric convection and larger-scale atmospheric circulations (Houze 2004). From a weather forecasting perspective, MCSs are very significant systems as they are associated with heavy precipitation. Accurate quantitative precipitation predictions associated with these strong MCSs have been a particularly difficult problem (Fritsch and Carbone 2004). The prediction of the exact timing, location, and intensity of convective systems is even more difficult. These difficulties arise from our inadequate understanding of MCSs and the inability of typical numerical models to accurately represent the physical processes associated with them (Liu and Xue 2008). Thus, it is of great interest to improve our understanding of MCSs.

Many previous studies have revealed the features of a typical MCS (Houze 1989; Biggerstaff and Houze 1991). Commonly, an MCS consists of many individual cells that interact with each other. The coexistence of mature, dissipating older cells and

developing newer cells makes the lifecycle of a MCS longer than that of an individual convective cell. According to its structure and evolution, one entire MCS lifecycle can be categorized into several different stages, including initiation, development, maturity, and dissipation (Engerer et al. 2008).

The strong convective precipitation region, moderate homogeneous stratiform precipitation region, large anvil shield, system-wide mesoscale flow (ascending front-to-rear flow and descending rear-to-front flow), and morphological features (radar echo boundary) have been comprehensively discussed in Houze (2004). These components determine the distributions of precipitation and thermodynamic properties. In addition, the mesoscale internal flows (ascending front-to-rear flow and descending rear-to-front flow) are related to the sustenance of the MCS size and the development of cold pools. They are also important factors in determining the appearance and behavior of a MCS. According to its structural features, three major aspects of a MCS, including (1) precipitation and cloud features, (2) mesoscale flows, and (3) cold pools, will be discussed in the following sections.

1.1.1 Precipitation and Cloud Features

MCS clouds consist of a precipitating region and a nonprecipitating anvil region. Precipitation in a MCS is generally considered to be of two clearly distinguishable types: heavy precipitation in the convective region and moderate homogeneous precipitation in the stratiform region (Ogura and Chen 1977; LeMone et al. 1984). Stratiform rain accounts for much of the rain area and ~40% of the total precipitation (Schumacher and Houze 2003). Over the life cycle of a MCS, rain evolves from more convective to more

stratiform (Houze 1989; Futyan and Del Genio 2007), accompanied by a change in diabatic heating distribution (Houze 1989). These two precipitation types can be classified based on a vertical velocity scale (Tao and Simpson 1989; Tao et al. 2000), precipitation intensity (Churchill and Houze 1984; Caniaux et al. 1994), or radar reflectivity structure (Steiner et al. 1995; Feng et al. 2011).

Convective and stratiform precipitation comes from convective and stratiform clouds, respectively. Convective and stratiform clouds differ both dynamically and thermodynamically. Hydrometeor growth mechanisms are different for these two types of clouds. Aircraft observations confirm that the ice particles in convective clouds grow largely by riming, while deposition and aggregation are the primary growth mechanisms in stratiform regions (Churchill and Houze 1984). The corresponding latent heating profiles are also quite different for the two regions (e.g., Leary and Houze 1979; Houze 1982; Tao et al. 1989). The convective region exhibits net heating at all levels, while the stratiform shows net heating only aloft and net cooling in the lower troposphere. In addition, solar and infrared radiative heating can modify the latent heating profiles, especially during the long lifetime of MCSs (Houze 2004).

In addition to the convective and stratiform clouds, the nonprecipitating anvil region is also important to the MCS. Del Genio et al. (2012) stated that even though the stratiform rain region and anvil contribute little to water vapor feedback (Del Genio et al. 1991), they are important in cloud feedback because of their effect on vertical motions (Yao and Del Genio 1999; Zelinka and Hartmann 2010). The radiative heating profile in stratiform and anvil clouds can stabilize/destabilize different altitudes and affect vertical motion (Jensen and Del Genio 2003).

1.1.2 Mesoscale Flows

An MCS exhibits system-wide mesoscale flows (upward front-to-rear flow and downward rear-to-front flow). These are important for the sustenance of cloud coverage and precipitation distribution. Front-to-rear relative flow originates ahead of the surface gust front from the low levels to the high levels in the rear. Modeling studies (e.g., Fovell and Ogura 1988; Tao et al. 1993) and thermodynamic retrievals (e.g., Hauser et al. 1988) have proven the existence of the advection of positively buoyant air from the convective region in the front-to-rear relative flow at middle and upper levels. The advection transports hydrometeors rearward from the convective line to the stratiform and anvil regions. They eventually contribute to the precipitation in the stratiform region and to the sustenance of large coverage of the anvil region (Smull and Houze 1985; Rutledge and Houze 1987).

Rear-to-front inflow is a layer of low-potential-temperature air that enters the MCS from the rear below the trailing anvil and stratiform clouds and descends toward the leading convective line (Houze 2004). It is commonly recognized that the rear-to-front flow is a gravity wave response to heating in the convective region (Schmidt and Cotton 1990; Pandya and Durran 1996), while sublimation, melting, and evaporation of precipitation particles enhance the midlevel inflow that descends when it comes under the trailing stratiform cloud deck (Smull and Houze 1987; Lafore and Moncrieff 1989).

1.1.3 Cold Pool

The cold pool is one of the most distinctive features of a well-organized MCS. It is the evaporatively cooled area of downdraft air that spreads out horizontally under a

precipitating cloud (Engerer et al. 2008). The boundary between a cold pool and its environment is called the outflow boundary. It is a primary mechanism for the maintenance and organization of multicell thunderstorms and deep convection systems (Thorpe et al. 1982; Rotunno et al. 1988; Szeto and Cho 1994). The leading edge of the outflow boundary is termed the gust front. Many investigators (e.g., Wakimoto 1982; Droegemeier and Wilhelmson 1987; Muller and Carbone 1987) have indicated that gust fronts play an important role in thunderstorm dynamics. The speed of a gust front is governed by the density difference between the cold pool and its environment, as well as cold pool depth (Wakimoto 1982).

The gust front maintains a thunderstorm by forcing warm, moist air upward (Purdom 1976; Wilson and Schreiber 1986), or by triggering new convection cells because of the low-level convergence (Engerer et al. 2008). One study has shown that the lifting of air along mesoscale-sized cold pool boundaries can produce moist unstable layers of more than 100 hPa in depth that influence the internal structure of a convective system (Bryan and Fritsch 2000).

In addition, the interaction between the surface outflow and the low-level shear produces much-deeper and less inhibited lifting than is possible without the low-level shear, making it easier for new cells to form and grow as old cells decay. Subsequent interaction between the cold outflow and the ambient shear can initiate new convection and promote long-lasting, organized convective systems (Thorpe et al. 1982; Rotunno et al. 1988).

1.2 Microphysical Parameterization

As stated in the previous section, the prediction of the exact timing, location, and intensity of convective systems is difficult, mainly because of the uncertainties in representing important physical processes in numerical models (Liu and Xue 2008). With increase computing power, cloud-resolving models (CRMs) have become an important tool for studying MCSs and clouds. Cloud-resolving models are generally defined as models with horizontal grid spacing small enough (~1km) to be able to explicitly simulate individual clouds, but large enough to represent cloud systems (Randall et al. 2003). CRMs show promise for improving the skill of MCS forecasting, because they can better resolve the dynamic and thermodynamic structure of MCSs. However, there are still uncertainties in CRMs, especially in the physical processes that have been parameterized at the subgrid scale (Bryan and Morrison 2012). Since microphysical processes are some of the most important processes, microphysical parameterization (MP) is an important source of uncertainties in MCS simulation. MP controls the formation and dissipation of cloud droplets and ice crystals, and influences precipitation prediction. It is an important component in cloud, weather, and climate models (Morrison 2010). In addition, microphysical processes interact with other processes, such as dynamic, turbulence, and radiative transfers. Therefore, improving MP is an important way to eliminate uncertainties in CRM simulations.

Numerous cloud MP schemes have been developed in numerical weather prediction (NWP) models to account for the complicated nature of cloud and precipitation systems (Morrison 2010; Han et al. 2013). Specifically, these MP schemes vary in the number of hydrometeor species and the treatments of the size distribution of

each hydrometeor species.

Earlier MP schemes, such as the Kessler scheme (Kessler 1969), are simple and include only warm-rain hydrometeors (water vapor, rainwater, and cloud water). In the mesoscale community Weather Research and Forecasting (WRF) model, the WRF single-moment 3-class Microphysics Scheme (WSM3) represents this kind of MP scheme. Ice microphysical processes have important impacts on MCS dynamics and surface precipitation due to the slower fall speeds of snow compared to rain and extra latent heating (cooling) released from freezing (melting). Complexity is added to MP schemes by including additional ice categories, such as cloud ice, hail, and graupel, which reflects the importance of ice processes in convection evolution (Fovell and Ogura 1988; McCumber et al. 1991; Liu et al. 1997). The works of Lin et al. (1983) and Rutledge and Hobbs (1983) have been central in the representations of cloud and precipitation processes in current bulk microphysical parameterizations (Thompson et al. 2008; Morrison et al. 2009; Lim and Hong 2010; Mansell et al. 2010). Many recent MP schemes include both warm-rain and ice hydrometeors.

Microphysical schemes are divided into two types, according to their treatments of hydrometeor particle size distribution. The bin scheme uses dozens, even hundreds of particle size bins to represent the size spectra of different hydrometeor particles (Li et al. 2009). The bulk MP scheme (BMP), assumes that hydrometeor size distributions follow specific functional forms for both single-moment (1M hereafter, predicting only mixing ratio) and multiple-moment representations of hydrometeor distribution (Milbrandt and Yau 2005a,b; Morrison et al. 2009; Phillips et al. 2007). Specifically, double-moment

schemes (2M hereafter) predict both mixing ratios and number concentrations for various hydrometeor species.

Bin microphysical schemes are computationally expensive and thus have limited weather and climate forecast applications. Therefore, BMPs are more practical for Numerical Weather Prediction (NWP) models, especially for 1M schemes because they are computationally efficient and simple in terms of their treatment of microphysical processes. On the other hand, 2M schemes increase the degrees of freedom, and thereby allow more flexible treatment of particle size distribution (Bryan and Morrison 2012).

1.2.1 Single-Moment Schemes

A single-moment (1M) scheme predicts only mixing ratios. Number concentrations are diagnosed from prior assumptions and the predicted mixing ratios. They are relatively computationally efficient compared with 2M schemes.

Cloud and precipitation particle size distributions are represented by gamma distributions:

$$N(D) = N_0 D^{\mu} e^{-\lambda D} \tag{1.1}$$

where N_0, λ, and μ are the intercept number, slope, and shape parameters of the size distribution, respectively, and D is the particle diameter.

Among most 1M schemes, N_0 is specified for each hydrometeor species. Note that although most 1M schemes use a constant value for N_0, it is not an intrinsic feature of these schemes (Morrison et al. 2009); some MP schemes allow N_0 to vary as a function

of predicted cloud or thermodynamic variables. For instance, the WRF Single-Moment 6-class (WSM6) and WRF Double-Moment 6-class (WDM6) schemes assume that N_0 of snow (N_{0s}) is a function of temperature following Hong et al. (2004):

$$N_{0s} = 2 \times 10^6 \exp[0.12(T_0 - T)] \tag{1.2}$$

Thompson et al. (2008) allow variable N_0 for snow and graupel.

After N_0 and μ are specified, the slope λ can be determined from the predicted mixing ratio q:

$$q = \int_0^\infty \frac{\pi}{6} \rho_i N_{0i} D^{3+\mu} e^{-\lambda D} \, dD \tag{1.3}$$

$$\lambda = \left[\frac{\pi \rho_i N_0 \Gamma(\mu + 4)}{6 q_i} \right]^{\frac{1}{\mu+4}} \tag{1.4}$$

where *i* represents one specific kind of hydrometeor species (rain, snow, ice, graupel, etc.), rho_i is the density of one specific hydrometeor species, Γ is the Euler gamma function, and the shape parameter μ is always set to be 0 for the precipitation species (i.e., rain, snow, and graupel), as well as cloud ice. After q, λ, and $\mu$are specified, particle size distributions can be calculated through equation (1.1).

The continuity equation for each hydrometeor species is:

$$\frac{\partial q_i}{\partial t} = -\vec{V}\nabla_3 q_i - \frac{q_i}{\rho}\frac{\partial}{\partial z}(\rho V_i + S_i) \tag{1.5}$$

where the first and second terms represent the 3-dimensional (3D) advection and sedimentation of hydrometeors, respectively. V is the air velocity, V_i is the terminal velocity for the specific hydrometeor species, and S_i represents the sources and sinks of the specific type of hydrometeor (Hong and Lim 2006).

Note that not all of the 1M schemes use the same assumptions in the M-D (mass-diameter) V-D (velocity-diameter) relationships and other parameters, such as raindrop breakup, and collection efficiency (Hong and Lim 2006; Lim and Hong 2010). In addition, different schemes vary significantly in their treatments of the source and sink terms. Different hydrometeor species are involved in conversion processes, such as evaporation (from rainwater to water vapor), melting (from snow/graupel to rainwater), sublimation (from snow/graupel to water vapor), freezing (from cloud water to cloud ice), and accretion (from cloud water to rain) (Lin et al. 1983; Hong et al. 2004; Morrison and Grabowski 2008; Mansell et al. 2010), etc. Models treat these conversions as instantaneous processes, meaning many thresholds should be used in the MP schemes; for instance, the Morrison scheme requires a minimum mixing ratio of 0.1g/kg for rain and snow to produce graupel from collision between them. The threshold values vary in

different schemes (Morrison et al. 2009).

1.2.2 Double-Moment Schemes

Double-moment schemes predict both mixing ratio and number concentration for each hydrometeor species. Then, the slope parameter λ and intercept number N_0 are derived from the predicted number concentration N and mixing ratio q by equations (1.6) and (1.7).

$$\lambda = \left[\frac{cN\Gamma(\mu + d + 4)}{q\Gamma[\mu + 1]} \right]^{\frac{1}{d}} \tag{1.6}$$

In this equation, the parameters c and d are given by the assumed power-law mass-diameter (M-D) relationship of the hydrometeors for each species, where $m=cD^d$ (Morrison et al. 2009). In many schemes, d=3 (sphere) and c varies from 0.1 g cm^{-3} for snow, to 0.05-0.89 g cm^{-3} for graupel, or 0.7-09 g cm^{-3} for hail (Pruppacher et al. 1998). d equals 3 is not an intrinsic feature in models. More recently, schemes have been developed that assume d~2 for ice hydrometeor particles (Morrison and Grabowski 2008; Thompson et al. 2008; Mibrandt and Cowan 2010), which is believed to be close to values derived from observations and theoretical studies (Morrison 2010) (WRF Workshop). For the schemes used in this study, all particles are assumed to be spheres for

simplicity, with a bulk particle density for the various ice species given by Reisner et al. (1998). The intercept parameter can be calculated by the equation (1.7).

$$N_0 = \frac{N\lambda^{\mu+1}}{\Gamma(\mu+1)} \tag{1.7}$$

Combining equations (1.6) and (1.7), through the predicted number concentration N and mixing ratio q, N_0 and λ can be computed. Then, the particle size distributions can be specified by equation (1.1).

In addition to the continuity equation for the mixing ratio, 2M schemes add another prediction equation (1.8) for number concentration N.

$$\frac{\partial N_i}{\partial t} = -\vec{V}\nabla_3 N_i - \frac{N_i}{\rho}\frac{\partial}{\partial z}(\rho V_i + S_i) \tag{1.8}$$

Because 1M predicts only the mixing ratio, the number concentration is a diagnosed variable, and only mass-weighted fall speed is predicted. In contrast, 2M schemes incorporate the number concentration fall speed. The mass fall speed is always larger than the number (N) fall speed, which enables 2M schemes to capture the size sorting process. In addition, some phenomena are also unique in -2M schemes, such as the increase in rain number concentration due to melting (from snow/graupel to rain),

which is equal to the decrease in the snow and graupel number concentrations. It is not treated in 1M schemes since they do not predict the particle number concentration (Morrison et al. 2009).

Since 2M schemes increase the degrees of freedom and allow for a more flexible treatment of particle size distributions (Bryan and Morrison 2012), they potentially improve the calculation of microphysical processes, relative to the use of 1M schemes (Morrison et al. 2009). Computational expense is an obvious disadvantage of 2M schemes, but the increase in computational power in recent years mitigates this disadvantage.

1.2.3 Evaluation of the Performance of MP Schemes

Numerous studies have evaluated the performance of different MP schemes in convective system simulations and have improved the currently available schemes. For instance, Wu et al. (2013) tested the sensitivity of simulated squall lines to 2ice schemes (ice, snow, i.e., WSM5 and GCE-2ice schemes) and 3ice schemes ice, snow, graupel/hail, i.e., WDM6, GCE-3ice) and compared the simulations with radar and surface data. Results demonstrated that the 3ice (including graupel/hail) schemes increased precipitation intensity, as well as updraft and downdraft intensity, and produced a positive dBZ bias. 3ice schemes produced stronger reflectivity in the convective region than 2ice schemes, while 2ice schemes generated stronger reflectivity in stratiform regions.

Hail or graupel could be a particularly important species because it influences the quantity and type of precipitation received on the ground in many types of midlatitude

thunderstorms (Gilmore et al. 2004), and because the melting of hail/graupel is the largest source of rainwater in 2D midlatitude squall line simulations (Fovell and Ogura 1988). Among 3ice schemes, the use of hail or graupel as dense riming ice also impacts simulations significantly. Bryan and Morrison (2012) demonstrated that simulations with graupel as dense ice produced unrealistically wide convective regions, while simulations with hail produced better convection properties (precipitation, cold pool, and cloud structure). At the same time, Gilmore et al. (2004) also noted that simulations with hail tend to produce more accumulated precipitation than those with graupel.

In order to improve and simplify MP schemes, recent work has attempted to move away from the paradigm of separating ice into different species. Instead, particle type has been allowed to vary as a function of the riming and vapor deposition ice-mixing ratios or process rates, which are predicted or diagnosed separately (Stoelinga et al. 2007; Morrison and Grabowski 2008; Lin and Colle 2011). For example, the Stony-Brook University Lin (SBU-LIN) scheme in the WRF model represents a continuous spectrum from pristine ice particles to heavily rimed particles and graupel using one prognostic variable rather than two variables (snow and graupel). It is more computationally efficient due to the reduced number of parameterized microphysical processes compared with six-category BMPs.

A common problem in many bulk microphysical schemes used in cloud-resolving models is the high positive dBZ bias in the middle and upper troposphere in the simulated convective systems. Lang et al. (2011) modified some snow/graupel riming parameters, adding rime splintering, immersion freezing, and contact nucleation and thereby converting less rimed snow to graupel in the Rutledge and Hobbs bulk scheme in order to

reduce this positive dBZ bias. The sensitivity study demonstrated that strong echoes in the middle and upper troposphere were reduced in a weakly organized continental case and an oceanic mesoscale convective system (MCS), while peak reflectivities remained too high for the MCS.

Recent studies have suggested that numerical simulations with 2M schemes can better simulate stratiform precipitation and convection-induced cold pool characteristics because of more realistic predictions of evaporative cooling rates, distribution of hydrometeor number concentrations, and mixing ratios (Morrison et al. 2009; Lim and Hong 2010; Weverberg and Vogelmann 2012). However, detailed evaluation of 2M schemes has not yet been conducted in the community WRF model using observations with detailed MCS cloud components.

In addition, 1M and 2M represent the two common ways of representing of the microphysical processes in BMPs. Among the available 2M schemes in the WRF model, some are partial 2M, as they treat some hydrometeors as two-moment species while others are still 1M species. For example, the Thompson scheme (Thompson et al. 2008) represents rainwater as a 2M specie; the WDM6 treats warm-rain hydrometeors as 2M species and ice hydrometeors as 1M species. Meanwhile, some 2M schemes are full 2M and represent all hydrometeors (including warm-rain and ice hydrometeors) as 2M species.

Obviously, the major difference between the partial and full 2M schemes is the representation of the ice species. It is well known that the uncertainties in microphysics parameterizations arise mainly from the treatment of ice processes. Therefore, the important question here is: Are the full 2M treatments of hydrometeor necessary for

better prediction of MCSs? In fact, this is controversial. Some previous studies have found that using double-moments for rain only can produce the same results as using a full 2M scheme (Morrison et al. 2009). In contrast, Weverberg and Vogelmann (2012) pointed out that the simulations of surface precipitation and cold pools depend on a 2M representation not only of rain, but also of all precipitating hydrometeors. A comprehensive evaluation of the convection structure, precipitation, and dynamics as well as hydrometeor properties is becoming very important for determining the necessity of 2M representations of ice hydrometeors.

In light of the previous studies, it is important to raise these questions: What is the relative performance of 1M versus partial 2M and full 2M schemes in accurately predicting MCSs with the WRF model? How important are ice processes in predicting MCSs?

1.3 Scope of This Study

In order to address the questions above, in this study, we choose an MCS case that occurred over the Southern Great Plains (SGP) of the United States to evaluate the 1M and 2M schemes. The case was selected because MCSs are very important mesoscale events over the SGP, as they are responsible for a large portion of the annual rainfall over this region. Specifically, we employ an advanced research version of the WRF (WRF-ARW) model to in our study.

In order to evaluate the necessity of 2M schemes for accurate prediction of MCSs and also to account for the complexity of MP, three MP schemes, including 1M, partial 2M, and full 2M schemes, are selected in this study. Specifically, they are the WRF

WSM6 (Hong and Lim 2006), the WDM6 scheme, and the Morrison double-moment scheme (MORR hereafter, Morrison et al. 2009). A radar reflectivity-based cloud classification algorithm (Feng et al. 2011) is used to classify the convection system into different cloud categories. Surface Mesonet observations, Next Generation Radar (NEXRAD) 3-dimensional (3D) radar reflectivity, and the National Centers for Environmental Prediction (NCEP) Stage-IV precipitation dataset are also used for the evaluation. The simulated ice phase hydrometeor properties are compared with the University of North Dakota (UND)-Citation aircraft dataset, because UND-Citation aircraft provides a direct measurement of ice hydrometeors.

The evaluation results with details of the numerical simulations and verification are presented in Chapter 2. Additional sensitivity experiments are summarized in Chapter 3. Chapter 4 discusses the comparison between the simulations and UND-Citation dataset. A summary and concluding remarks are provided in Chapter 5.

CHAPTER 2

EVALUATION OF DOUBLE-MOMENT BMP SCHEMES

2.1 The Weather Research and Forecasting Model

The Weather Research and Forecasting (WRF) model is a mesoscale community NWP system. It is designed to serve both operational forecasting and atmospheric research needs. The WRF model features multiple dynamic cores. This study employs the advanced research version of the WRF model (WRF ARW). The WRF ARW is based on an Eulerian solver for the fully compressible nonhydrostatic equations, is cast in flux conservation form, and uses a mass (hydrostatic pressure) vertical coordinate. The solver uses a third-order Runge-Kutta time integration scheme coupled with a split-explicit second-order time integration scheme for the acoustic and gravity-wave modes. Fifth-order upwind-biased advection operators are used in the fully conservative flux divergence integration; second- to sixth-order schemes are run-time selectable. The WRF ARW carries multiple physical options for cumulus, microphysics, planetary boundary layer (PBL), and radiation physical processes. Details of the model are provided in Skamarock et al. (2008).

2.2 Data and Method

The data used in this paper include NEXRAD 3D radar reflectivity, Stage IV hourly precipitation data and surface Mesonet accumulate precipitation, temperature at 1.5 m of height, relative humidity, and winds at 10 m height at 5 min intervals.

2.2.1 NEXRAD Radar Observation

Radar reflectivity data are obtained from three NEXRAD radars (KTLX, KINX, KVNX) that cover most of the Oklahoma region. The radars operate at the wavelength of 10 cm (S band) in a preprogrammed sequence of 360 azimuthal sweeps at various elevation angles (Klazura and Imy 1993).

2.2.2 Oklahoma Mesonet Data

Surface data are obtained from the Oklahoma Mesonet. Mesonet is a network of automated weather stations designed to observe mesoscale meteorological phenomena (Brock et al. 1995). Oklahoma Mesonet includes 127 stations that cover the entire Oklahoma region. In this study, temperature, humidity, and wind data are used to identify the dryline.

2.2.3 Stage IV Precipitation Data

The NCEP stage-IV precipitation dataset contains precipitation analyses obtained from approximately 150 high-resolution Doppler NEXRADs and about 5500 hourly rain gauge reports over the continental United States (Baldwin and Mitchell 1996; Lin and Mitchell 2005). The datasets are from the regional hourly/6-hourly multisensor

(radar+gauges) precipitation analyses produced by the 12 River Forecast Centers (RFCs) over Contiguous United Stated (CONUS); some quality controls are done at RFCs. See more detail online at http://www.emc.ncep.noaa.gov/mmb/ylin/pcpanl/.

2.2.4 Radar Reflectivity-Based Cloud Classification

The radar-based cloud classification algorithm is developed following the work by Steiner and Feng (Steiner et al. 1995; Feng et al. 2011). This algorithm can classify the convection system into convective cores (CC), stratiform rain (SR), and non-precipitating transitional anvil cloud (ACtrans) and anvil cloud (AC) from 3D radar reflectivity observations. Among the products: The convective core is chartered by strong upward motion, intense precipitation; Stratiform rain (SR) is known for its widespread homogenous precipitation and weak horizontal reflectivity gradient. Transitional anvil is a transitional stage from precipitating SR to nonprecipitating anvil clouds, the cloud base below 3 km and top above 6 km. Anvil clouds (AC) are represented by radar reflectivity that has an echo base above 3 km (Feng et al. 2011). Both TransAC and AC are nonprecipitating clouds. Wu et al. (2013) confirmed this cloud classification algorithm is able to separate the dynamic and thermodynamic properties of MCS.

2.3 Description of the Convective Case

In order to document and monitor 3D precipitation, clouds, winds, and moisture in an attempt to provide a holistic view of convective clouds, their environment, and associated feedbacks, the Midlatitude Continental Convective Clouds Experiment (MC3E) was conducted at Southern Great Plains (SGP) between April and June 2011. A

MC3E case (May 23-24) during MC3E was selected for this study. This event occurred between 23 May and 25 May. It was supported by upper-level trough and the low-level moisture supplied from the Gulf of Mexico. The case consisted of four mainly convective processes that interacted with each other through dynamic and thermodynamic processes. In this study, we chose the second convective process period (from 2100 UTC 23 May 2011 to 0600 UTC 24 May 2011), considering the availability of radar-derived data product.

Figure 2.1 shows that the convective system initiated at about 2100 UTC 23 May 2011 and moved out of the Oklahoma region at about 0600 UTC 24 May 2011 (Fig. 2.1 a-f). This convective system was originally formed with the isolated convective cells in the western Oklahoma region (Fig. 2.1a) under the influence of dryline and outflow boundary produced by the previous convective process in the northeastern Oklahoma. Figure 2.2 shows the surface relative humidity (shading) and temperature (contour red lines) at 1.5 meter height, and 10 meter wind vectors at 2000 UTC 23 May 2011. The dryline (Fig. 2.2) and three convective cells (as shown in Fig. 2.1a) were clearly observed from NEXRAD reflectivity, as shown in Figure 2.1a and Mesonet data. After the initiation, the convective system was strengthened in both size and intensity in the next few hours, and became a multicell mesoscale convective system with NE-SW orientation at 2300 UTC 23 May 2011 (Fig. 2.1b). This MCS then combined with the first convective process at 0000 UTC 24 May 2011 and evolved into a mature stage while the cells organized in a S-N direction. The mature stage lasted about 3-4 hours (Fig. 2.1c and d). Finally, this MCS began to dissipate about 0400UTC 24 May 2011(Fig. 2.1e) and slowly moved out of the Oklahoma region at about 0600 UTC 24 May 2011(Fig. 2.1f).

According to its structure and evolution with time, this MCS can be categorized as four different stages: initiation (2100 UTC 23 May 23, Fig. 2.1a), developing (2200 to 2300 UTC 23 May 2011, Fig. 2.1b), mature (from 0000 to 0400 UTC 24 May 2011, Fig. 2.1c and d), and dissipating (0400 UTC 24 May 2011, Fig. 2.1e and f) stages.

2.4 Experimental Design

The WRF ARW model Version 3.4.1 is employed. Three nested domains are used with outermost domain resolution at 12 km, second domain at 4 km and the inner-most domain at 1.33 km. As stated in Chapter 1, 1.33 (~1) km horizontal resolution is believed to be sufficient for simulating the convective systems and the cloud structure. Forty-six vertical sigma levels are used with more dense levels in the lower atmosphere for better resolving boundary layer processes. Figure 2.3 displays the model domains used in all simulations. The blue box denotes the verification region. Initial and boundary conditions are derived from the NCEP North American Mesoscale Model (NAM) analysis. The simulation covers the period from 0000 UTC 23 May 2011 to 1200 UTC 24 May 2011. The initial time is 20 hours before the convection initiation, which is believed to be long enough to eliminate the possible strong influence from initial conditions.

Physical parameterizations schemes include: the Kain-Fritsch cumulus scheme (Kain 2004, for the outermost domain only), the Rapid Radiative Transfer Model (RRTM; Mlawer et al. 1997) longwave, the Dudhia shortwave (Dudhia 1989) radiation scheme, the RUC (Rapid Update Cycle) (Smirnova 2000) land-surface scheme, and the Mellor-Yamada-Janjic (Eta) (Janjic 1990) Turbulent Kinetic Energy (TKE) Planetary Boundary Layer (PBL) scheme.

Three experiments with different MP schemes are made in order to examine the sensitivity of WRF simulations to different moment representations of the warm-rain and ice hydrometeors in BMP in predicting MCSs properties. These MP schemes include: the WSM6 scheme (1M), WDM6 scheme (partial 2M), and MORR (full 2M). As listed in Table 2.1, WSM6, WDM6, and MORR schemes utilize the same six hydrometeor-species, including three warm-rain species (cloud, rain, and vapor) and three ice species (ice, snow, and graupel). WSM6 is a 1M scheme, which predicts just the mixing ratios (Q) of these six kinds of hydrometeors; WDM6 predicts both Q and number concentrations (N) for warm rain hydrometeors (cloudwater and rainwater); MORR predicted both Q and N for all the precipitating hydrometeors (rainwater, snow, and graupel). For convenience, the numerical experiments with WSM6, WDM6, and MORR are hereafter respectively referred to as "WRF-WSM6", "WRF-WDM6", and "WRF-MORR".

2.5 Simulation Validations

2.5.1 Convection Structure and Evolution

Figure 2.4 shows snapshots of composite radar reflectivity at different MCS stages from various simulations. Compared with the NEXARD observations (Fig. 2.1a), all experiments (Fig. 2.4a, b, and c) predicted convection initiation successfully, although with time and location errors. At the developing stage, WRF-WSM6 (Fig. 2.4d) produced discrete radar reflectivity with multiple convective cells. The coverage of the convection system is small, which is a common problem of the WSM6 scheme, as it tends to produce an isolated intense convective core compared with other schemes (Thompson et al. 2006;

Weisman et al. 2009). WRF-WDM6 (Fig. 2.4e) predicts an organized convection system, although its area coverage is also smaller than observations. WRF-MORR (Fig. 2.4f) produced the proper area of convection coverage size. However, both WRF-WDM6 and WRF-MORR overestimated the intensity of the convective system compared with NEXRAD observation.

The differences in the simulations became more distinguishable in terms of the coverage and structure of convective system at the observed mature stage (Fig. 2.4g, h and i). Although observations (Fig. 2.1c) still show that the convective system is mature, it begins to dissipate in WRF-WSM6 (Fig. 2.4g). WRF-MORR (Fig. 2.4.i) produced a convective system that has similar coverage to the observed one (Fig. 2.1c) but with a much stronger convective core. The convective system in WRF-MORR is a squall line, slightly different from the observed multisupercell system. The error contributes to the overestimation of the precipitation amount. Compared with NEXRAD observations (Fig. 2.1c), all the simulations produce additional convective cells in northwestern Oklahoma. This is also one of the sources of overestimated precipitation amount in WRF-MORR. At the dissipation phase, WRF-MORR (Fig. 2.4l) produced realistic convection structure and coverage but performs poorly in predicting the strength of the convective system. WRF-WDM6 (Fig. 2.4k) shows clear improvement compared with WRF-WSM6 (Fig. 2.4j).

Because all simulations can correctly predict the convection initiation of MCS, but large discrepancies are found in the developing and mature stages, the rest of the study will emphasize the latter two stages.

Figure 2.5 compares vertical structures of the MCS observed by NEXRAD radar

and simulated by the WRF with different microphysical schemes at 2300 UTC 23 (developing stage) and 0100 UTC 24 May 2011 (mature stage). As illustrated in Figure 2.5a and 2.5e, the NEXRAD radar echo tops can extend up to 13 km at both developing and mature stages. The NEXRAD reflectivities range from 15 to 35 dBZ above the melting level in both the rearward and forward directions. Although WRF-MORR (Fig. 2.5.d and h) reproduces similar vertical structures to radar observations at both stages, it generates much broader moderate radar reflectivity in a range between 35 and 50 dBZ, especially in the middle and upper troposphere.

The simulations from both WRF-WSM6 (Fig. 2.5b and f) and WRF-WDM6 (Fig. 2.5c and g), however, underestimate the echo tops and only produce a small amount of the MCS structure. All the simulations exhibit high biases in the middle to upper troposphere, which is a common problem for the current bulk microphysics model (Lang et al. 2011), mainly because of the unrealistic high graupel amount in the simulations. The use of hail instead of graupel as a dense ice specie can eliminate this high bias to some extent. This will be discussed in detail in Chapter 3.

2.5.2 Length of Convective Life Cycle

As shown in Figure 2.4, the simulation with WSM6 produces the shortest convection lifetime, whereas the other two simulations predict a proper convection lifetime that agrees with the observation. During the convective evolution, old cells dissipate and new cells are triggered and develop. According to Fovell and Dailey (1995), the time series of the maximum vertical velocity is a good indicator of these cycles of cell regeneration. Figure 2.6 illustrates the maximum vertical velocities at 850hpa pressure

level, derived from the three simulations during the entire MCS period at 5 min interval. Before the MCS becomes mature (about 0000UTC 24 May 2011), maximum vertical velocities in all simulations show periodic feature. After that, WRF-WSM6 predicts steady maximum vertical velocities of small magnitude, while WRF-WDM6 and WRF-MORR produce multiple periodic peaks. The peak intensities are related to the new triggered cells ahead of the gust front in the leading-edge environment of the convective system. The peak intensity indicates for the length of the simulated convection life cycle.

2.5.3 Cloud Coverage

The convective cloud distribution reveals the internal 3D components and structure of the convective systems. A good simulation should reproduce the proper cloud components. In order to evaluate the convection structure in terms of different cloud categories, a radar-reflectivity-based deep convective system (DCS) cloud classification algorithm (Feng et al. 2011) is applied for both NEXRAD observations and WRF simulations. The cloud types include: CC and SR, the precipitating clouds, and ACtrans and AC, the nonprecipitating clouds. Figure 2.7 shows the snapshots of the classified components derived from NEXRAD observations (Fig. 2.7a and b) and WRF simulations (Fig. 2.7c to h) at developing and mature stages. In NEXRAD–derived products, a small area of convective clouds (CC) appears in the central convective system with a surrounding large stratiform (SR) area. Anvil clouds (AC) cover the outer region of convective system. Narrow but continuous transitional anvil clouds (ACtrans) appear between the stratiform and anvil cloud. Compared with NEXRAD-derived products, all simulations produce much larger CC. WRF-WSM6 (Fig. 2.7c and d) and WRF-WDM6

(Fig. 2.7e and f) both produce less SR. There are almost no ACtrans between CC and AC. In contrast, WRF-MORR (Fig. 2.7g and h)-produced cloud distribution agrees with NEXRAD-derived products reasonably, with CC in the core region, large SR surrounding CC, and clear ACtrans between SR and AC.

In order to examine the internal cloud structure, a time series of the cloud component fractions (CC, SR, ACtrans and AC against total cloud coverage) over the MCS is shown in Figure 2.8. The mean cloud fractions averaged over the whole time period are summarized in Table 2.2. Compared with the NEXRAD-derived data, all simulations overestimate the CC coverage (Fig. 2.8a). Specifically, WRF-WDM6 predicts the largest CC fraction overall (Fig. 2.8a and Table 2.2). In addition, the fraction of CC derived from NEXRAD is relative small at initiation and developing stages but increases in mature stage and then decreases at the dissipation stage. WRF-MORR captures this feature with a larger CC ratio at the mature stage and a smaller fraction at the initiation and dissipation stages, while both the WRF-WSM6 and WRF-WDM6 miss it.

The fraction of SR derived from NEXRAD is about 3 times larger than that of CC (Table 2.2). WRF-MORR (red) matches the NEXRAD-derived SR fractions well, but the ratio of SR/CC is unreasonable due to the large CC fractions; using hail instead of graupel as the dense ice specie could produce a better result for this convection case (see Chapter 3). Both WSM6 and WDM6, especially WDM6, underestimate the SR fractions. The extremely large CC fraction and small SR fraction produced by WDM6 confirm the unreasonable precipitation distribution it produces. WSM6 and WDM6 also heavily underestimate the ACtrans fraction (Fig. 2.8c), implying that both simulations produce an

unreasonable internal cloud structure. In particular, with 2M representations of warm-rain processes only, the WRF-WDM6 simulation does not reproduce a realistic cloud structure. With 2M representation of both warm-rain and ice processes, WRF-MORR produces a much better cloud structure.

2.5.4 Precipitation

To quantitatively evaluate the rainfall rate produced in the WRF simulations, hourly precipitation rates obtained from the NCEP Stage IV rainfall dataset (http://www.emc.ncep.noaa.gov/mmb/ylin/pcpanl/stage4) are used for comparison. The simulated precipitation is interpolated at Stage IV data grids for comparison. The time series of the rainfall rate is then achieved by averaging the precipitation amount over all data grids. The hourly averaged precipitation amount from both Stage IV and simulations are compared in Figure 2.9.

As shown in Figure 2.9, the precipitation peak occurs at the mature stage (during about 0100 UTC 24 May 2011) in Stage IV observations, with a small precipitation amount during the initiation and dissipation stages. The precipitation produced by WRF-MORR agrees well with this pattern, while slightly overestimating the precipitation amount at the same time. Both WRF-WDM6 and WRF-WSM6 perform poorly. WRF-WDM6 produces a large amount of precipitation (overestimation) during the dissipation stage, but heavily underestimates the precipitation amount during the mature stage. WRF-WSM6 heavily underestimates the precipitation amount over the entire MCS period. Specifically, the total accumulated apace averaged precipitation from 2000 UTC 23 to 0600 UTC 24 May 2011 observed by Stage IV is 12.6 mm, while that produced by WRF-

MORR is 14.7 mm, which overestimates the precipitation amount by 16.5%. WRF-WSM6 heavily underestimates the amount, by 43%, and WRF-WDM6 also underestimates the amount, by 14.4%.

To further examine the impact of different moment representation of warm-rain and ice hydrometeors on precipitation forecast, the quantitative precipitation forecast (QPF) skill is evaluated for different simulations. The equitable threat scores (ETS) are computed using equation (2.1):

$$ETS = \frac{A}{A + B + C} \tag{2.1}$$

For a given threshold, A represents the number of grid points that the model forecast and observation exceed the threshold; B denotes the number of grid points that the model forecast exceeds the threshold, but the observation does not; and C is the number of grid points when the model forecast does not reach the threshold, but the observation exceeds it (Wilks 1995).

Precipitation verification is performed using a NCEP Stage IV hourly rainfall dataset with three thresholds: 1 mm h^{-1}, 5 mm h^{-1}, and 10 mm h^{-1}. Time series of ETS are shown in Figure 2.10. Among all simulations, WRF-MORR shows the best ETS scores most of the time. WRF-WDM6 performs better than WRF-WSM6, especially for medium to heavy rainfall (Fig. 2.10b and c). Overall, the simulation with partial 2M (e.g., WRF-WDM6) helps the predication of precipitation. The simulation with full 2M (e.g., WRF-MORR) performs better than that with the partial 2M scheme.

2.6 Effect of Double-Moment Prediction of Rain and Ice

The evaluation results so far show that all the simulations reproduce the basic properties of the convective system such as its initiation and development. Compared with NEXRAD observations, the simulation with 1M scheme produces the most disorganized convection distribution, the shortest convection lifetime, and the lowest echo top. It also heavily underestimates the precipitation. The cloud component distributions and fractions are also unreasonable. By adding 2M representations of warm-rain hydrometeors, WRF-WDM6 shows a clear improvement in predicting the convective system by producing a proper convection lifetime and an organized convection horizontal structure. Even though the precipitation amount is larger than that in WRF-WSM6, WRF-WDM6 still underestimates the precipitation amount compared with observations. The cloud distribution and fractions are also unrealistic, and the echo top is lower than in that NEXRAD observations; The simulation with full 2M MP schemes (MORR) is a much better simulation, as it predicts the proper convection lifetime, echo tops, and cloud component distributions and fractions, as well as precipitation amount.

To better understand why the simulations produce different convection properties and to associate these properties with different moment, representations of warm-rain and ice hydrometeors on simulations of convection evolution will be further diagnosed and investigated this this section.

2.6.1 Cold Pool

As mentioned in Chapter 1, the shape and strength of the cold pool influence the eventual MCS structure, longevity, and development (e.g., James et al. 2006; Selin et al.

2013). Previous studies have shown that simulations with 2M microphysical schemes could result in a better cold pool intensity forecast than those with 1M schemes, because 2M schemes help produce a more realistic evaporation rate due to realistic particle size distributions (Morrison et al. 2009). Typically, a cold pool is indicated by temperature decreases, pressure increases, as well as local divergence. The 2-meter air temperature, sea level pressure and 10-meter wind field from simulations at the developing stage (2300 UTC 23 May 2011) are illustrated in Figure 2.11a, b, and c. Specifically, Figure 2.11a (WRF-WSM6), b (WRF-WDM6), c (WRF-MORR) indicate cold pools by the colder temperatures. It is apparent that the size and structure of cold pools correspond well with the distribution of composite radar reflectivity (Fig. 2.4d, e, and f). Figure 2.11d (WRF-WSM6), e (WRF-WDM6), and f (WRF-MORR) illustrate the temperature cross-sections and 0 dBZ radar reflectivity, which depicts the convective system edges and the melting level. The figures show that the cold pool edge matches the convection edge (about 36.3N) well in WRF-WSM6 (Fig. 2.11d), while its intensity (in terms of the temperature difference between the cold pool and its environment) is weaker than that in WRF-WDM6 (Fig. 2.11e) and WRF-MORR (Fig. 2.11f). In addition, there are apparent inversion layers at about 0.8 km height in the stratiform cloud region. The inversion layers cause discontinuity of vertical structure of the cold pool, thus prevent triggering new convective cells in WRF-WSM6. This explains at least in part why WRF-WSM6 predicts a shorter lifetime of the convective system compared with the observations.

The cold pool edge simulated by WRF-WDM6 (Fig. 2.11e) overlaps with the convection system border. Its intensity of cold pool is stronger and its size is larger than that in WRF-WSM6. Lim and Hong (2010) noted that a simulation with WDM6 showed

well-organized downdrafts with a strengthened cold pool as compared to the result with WSM6 in an idealized 2D thunderstorm simulation. WRF-MORR (Fig. 2.11f) produces a cold pool edge that is away from the radar echo edge. This is because the present of light precipitation occurred in the moving direction of the convection. The cold pool from WRF-MORR is also larger than that from WRF-WSM6 and is more homogenous. In addition, both WRF-MORR and WRF-WDM6 produced a deeper cold pool than WRF-WSM6.

2.6.2 Number Concentration, Hydrometeors, and Diabatic Cooling

A cold pool is the result from diabatic cooling by evaporation, sublimation, and melting of precipitation particles (Houze 2004). Specifically, diabatic cooling is due mainly to rainwater evaporation and the melting and sublimation of ice phase hydrometeors (i.e., graupel and snow). In order to understand the reasons for different cold pool properties among the simulations, the diabatic cooling and hydrometeor profiles in the different simulations are examined.

The evaporation, melting, and sublimation in the stratiform region all contribute substantially to the cold pool evolution (as suggested by Smull and Houze (1987) and Lafore and Moncrieff (1989)). The evaporate rate can be calculated by equation (2.2).

$$(\frac{\partial q_r}{\partial t})_{evap} = \frac{2\pi N_{0r} D_v (S-1)}{A' + B'} \times [\frac{f_1}{\lambda_r^2} + f_2 (\frac{a_r \rho}{\mu_a})^{\frac{1}{2}} S_c^{\frac{1}{3}} \frac{\Gamma(b_r/2+5/2)}{\lambda_r^{b_r/2+5/2}}] \qquad (2.2)$$

where D_v is the diffusivity of water vapor in the air, S is the liquid water saturation ratio, A' and B' are thermodynamic parameters related to the release of latent heat, a_r and b_r are

fall speed parameters for rain, μ_a is the air dynamic viscosity of air, S_c is the Schmidt number, and Γ is the Euler gamma function (Morrison et al., 2009).

In the above equation, the evaporation rate is a function of the mixing ratio and intercept parameter N_{0r}. For a given mixing ratio, larger N_{0r} causes a larger evaporation rate. The larger melting/sublimation processes of ice-phase hydrometeors behave in a similar way.

For the WSM6 scheme, N_0 for rainwater is constant at $8\times10^6/m^4$. However, WDM6 and MORR treat rainwater as double-moment species. In all three schemes, cloud and precipitation particle size distributions are represented by a gamma function:

$$N(D) = N_0 D^{\mu} e^{-\lambda D} \tag{2.3}$$

N_0, λ, and μ are the intercept, slope, and shape parameters of the size distribution, respectively, and D is the particle diameter.

In 2M moment schemes (WDM6, MORR), λ and N_0 derived from equation (2.4) and (2.5).

$$\lambda = \left[\frac{cN\Gamma(\mu+d+4)}{q\Gamma[\mu+1]}\right]^{\frac{1}{d}} \tag{2.4}$$

$$N_0 = \frac{N\lambda^{\mu+1}}{\Gamma(\mu+1)} \tag{2.5}$$

The intercept number N_0 is deduced from several parameters in equation (2.6).

$$N_0 = \frac{N\{[\frac{cN\Gamma(\mu+d+1)}{q\Gamma(\mu+1)}]^{\frac{1}{d}}\}^{\mu+1}}{\Gamma(\mu+1)} \tag{2.6}$$

The parameters c and d are given by the assumed power-law mass–diameter (m–D) relationship of the hydrometeors for each species, where $m = cD^d$, all particles are assumed to be spheres for simplicity (Morrison et al. 2009). For the precipitation species (i.e., rain, snow, and graupel), as well as cloud ice, $\mu = 0$, and for rainwater c=997kg/m^3, d=3. For graupel, c=400kg/m^3 (MORR) or 500kg/m^3 (WSM6 and WDM6), d=3.

In order to depict the diabatic cooling resulting from the rainwater evaporation in the different simulations, the rainwater mixing ratio for all simulations and the intercept number N_0 (only WRF-WDM6 and WRF-MORR) in the developing and mature stages are shown in Figure 2.12 and Figure 2.13, respectively. It is obvious that the WRF-WSM6 (Fig. 2.12a and d) produces a much smaller rainwater mixing ratio (q_r) than the other two simulations do. Compared with the simulation using fixed N_{0r} (N_0 for rainwater) in WSM6, WRF-WDM6 (Fig. 2.13a and c) and WRF-MORR (Fig. 2.13b and d) predict a decreasing trend of N_{0r} from the convective core (indicated by large dBZ value and strong upward wind in Figure 2.5) to the outer region (shown as medium or small dBZ value and weak upward or downdraft in Figure 2.5). N_0r (Fig. 2.13a and c) is larger than 8×10^6 over the entire region in WDM6. WRF-MORR (Fig. 2.13b and d) predicts larger N_0r (greater than 8×10^6) in the convective core region (which is indicated by the upward motion region at about 36.6N) and smaller N_0r (less than 8×10^6) in the outer region. The larger N_0r is located right below the melting level (in the zoomed-in

read box in Figure 2.13b and d). These regions correspond to the stratiform region indicated by the homogeneous dBZ and downward motion in Figure 2.5d and h. The larger N_0r around the melting level (indicated by a black line) is believed to be caused by the melting of graupel and snow. Because MORR treats the ice hydrometeors as 2M species, the melting process of graupel and snow can contribute to the increase of rain number concentrations and thus results in the decrease of graupel and snow number concentrations (Morrison et al. 2009). In addition, the size-sorting mechanism (which is not handled in 1M representations) allows the larger hydrometeors to fall faster than the smaller hydrometeors, resulting in more graupel and snow melting. Due to these effects, larger rainwater number (Fig. 2.13b and d) and larger rainwater mixing ratios (Fig. 2.13c and f) appeared in WRF-MORR. The change in number concentrations of graupel and snow also contributes to the abrupt change in dBZ around the melting level (as shown in Fig. 2.5d and h).

The relatively larger N_{0r} and smaller q_r from WRF-WSM6 means smaller mixing ratio of rain and small raindrops, that are easier to evaporate before they reach the ground. Thus, a discrete radar reflectivity distribution (Fig. 2.4a, d, g and j) and small dBZ value occur (Fig. 2.5b and f). This is different from WRF-WDM6, in which N_{0r} is larger than the number in WSM6, and the large q_r partly offset the influence of large N_{0r}. Very large N_0 and high q_r resulted in high evaporation rate and large amounts of rainwater that could arrive at the ground, a strong (Fig. 2.11e) and continuous cold pool that triggers new convective cells and maintains a realistic convection lifetime (Fig. 2.4 b, e, h and k and Fig. 2.6), and a larger precipitation amount (Fig. 2.9).

The sublimation and melting of ice-phase hydrometeors around the melting level

are also important for sustaining cold pools, especially deep cold pools. In this study, only graupel is analyzed, because it dominates the ice hydrometeors. Figure 2.14 shows the graupel mixing ratio (q_g) vertical cross section for the simulations. Figure 2.15 shows the graupel intercept number from WRF-MORR. Note that both WSM6 and WDM6 treat graupel as a 1M species, with a constant intercept number of N_{0g} of $4\times10^6/m^4$. From Figure 2.14, it is clear that q_g in WRF-MORR (Fig. 2.14c and f) is larger than in WRF-WSM6 (Fig. 2.14a and d) and WRF-WDM6 (Fig. 2.14b and e). The smaller graupel mixing ratio produced by WRF-WSM6 may be cause by the relatively small amount of supercooled water (Fig. 2.12a and d) above melting level for the riming processes. Due to the small amount of ice-phase hydrometers melting and sublimation around the melting level, WRF-WSM6 produces shallow and small cold pools (Fig. 2.11d). In addition, because of small precipitation amounts, WRF-WSM6 produces a cold pool air source with inadequate depth and time to trigger new cells. This seems to be the reason why WRF-WSM6 produces the shortest convection life cycle and also heavily underestimates the precipitation amounts.

N_{0g} in WRF-MORR (Fig. 2.15) also shows the decreasing trend from the convection core to the outer region. The value is much larger than 4×10^6. Graupel melting and sublimation below the melting level due to the size sorting mechanism in the SR region sustain cooling in the midtroposphere and contributes to a deep cold pool (as shown in Fig. 2.11f) that supplies continuous forcing to trigger new convective cells.

The total microphysical latent heating confirms the analysis of hydrometeors distribution. Figure 2.16 shows the cross-section of microphysics latent heating for three simulations. It is clear that diabatic cooling (blue colors) is present in the SR region

(zoomed by the black box). The cooling is less in WRF-WSM6 (Fig. 2.16a) than in the other two simulations (Fig. 2.16b and c). WRF-WDM6 (Fig. 2.16b) produces a very strong cooling in the SR region due to the very large N_{0r}. The elevated cooling region around melting level in the SR region from WRF-MORR (Fig. 2.16c) is due to the melting of graupel and snow and the large N_0r. Figure 2.16 also confirms the extension of deep cold pools in WRF-MORR (as shown in Fig. 2.11f).

2.6.3 Hydrometeors Advection

As stated in the previous section, WRF-WSM6 and WRF-WDM6 produced a relatively small percentage of stratiform cloud, while WRF-MORR shows better agreement with observations (Figs. 2.7 and 2.8). Previous observational studies claimed that hydrometeor advection is important to maintain large SR and AC regions in convective system (Biggerstaff and Houze 1991; Rutledge and Houze 1987), and these two regions are responsible for the large MCS coverage. In order to understand the reason for the differences in cloud structure produced by various simulations, hydrometeor advection is examined.

According to Houze (1989), the basic mechanism of hydrometeor advection in a typical MCS is the relative flow from the convective core to the outer region in the upper levels. Fortunately, as shown in Figure 2.5, all the experiments successfully simulated the upper-level flow from the inner core to forward and rearward (front to rear flow) regions (Fig. 2.5).

Hydrometeor advection is influenced by two main factors: one is the amount of ice-phase hydrometeors available in the core regions, and the other is the relative value of

the horizontal wind and the hydrometeors fall speed; the upper-level horizontal wind is caused by the upper-level divergence, which is a gravity wave response to the heating in the convective core. The ice-phase hydrometeors are initially produced in the convective core. In the simulations, WRF-MORR produces many more ice-phase hydrometeors (more particles as shown in Fig. 2.15 and larger mixing ratios as shown in Fig. 2.14), compared with WRF-WSM6 and WRF-WDM6. These hydrometeors act as the source of hydrometeors to be advected to produce larger SR and AC regions. This is one reason that the simulation with MORR produces larger and more realistic SR and AC region. In addition, the upper-level horizontal wind speed is larger in WRF-MORR (Fig. 2.14c and f) than in WRF-WSM6 (Fig. 2.14a and d) and WRF-WDM6 (Fig. 2.14b and e); the hydrometeor fall speed in WRF-MORR is less than in WRF-WSM6 or WRF-WDM6 due to the different graupel V-D relationship differences used in three microphysical schemes. The relatively high horizontal wind speed and small hydrometeor fall speed enable the hydrometeors to spread into a larger region. This accounts for the larger cloud coverage (as shown in Fig. 2.7 and 2.8) produced by WRF-MORR.

Table 2.1. Mass variables and number variables of the three microphysical schemes (WSM6, WDM6, MORR). Note that "c", "r", "i", "s", and "g" are abbreviations of "cloud water", "rain water", "ice", "snow", and "graupel". "Q" represents the mixing ratio. "N" is number concentration. Besides, Nn= CCN number.

Microphysical Scheme	Mass Variables	Number Variables
WSM6	Qc Qr Qi Qs Qg	
WDM6	Qc Qr Qi Qs Qg	Nn Nc Nr
Morrison 2-mom (MORR)	Qc Qr Qi Qs Qg	Nr Ni Ns Ng

Table 2.2. The mean cloud fractions averaged over the time period during 2000 UTC 23 May 2011 to 0600 UTC May 2011 and derived from NEXRAD observations and WRF simulations.

	CC	SR	ACtrans	AC
NEXRAD	0.116805	0.339358	0.196422	0.347416
WRF-WSM6	0.272633	0.237330	0.0491956	0.440842
WRF-WDM6	0.387878	0.0902116	0.0463075	0.461604
WRF-MORR	0.220521	0.356896	0.146489	0.276095

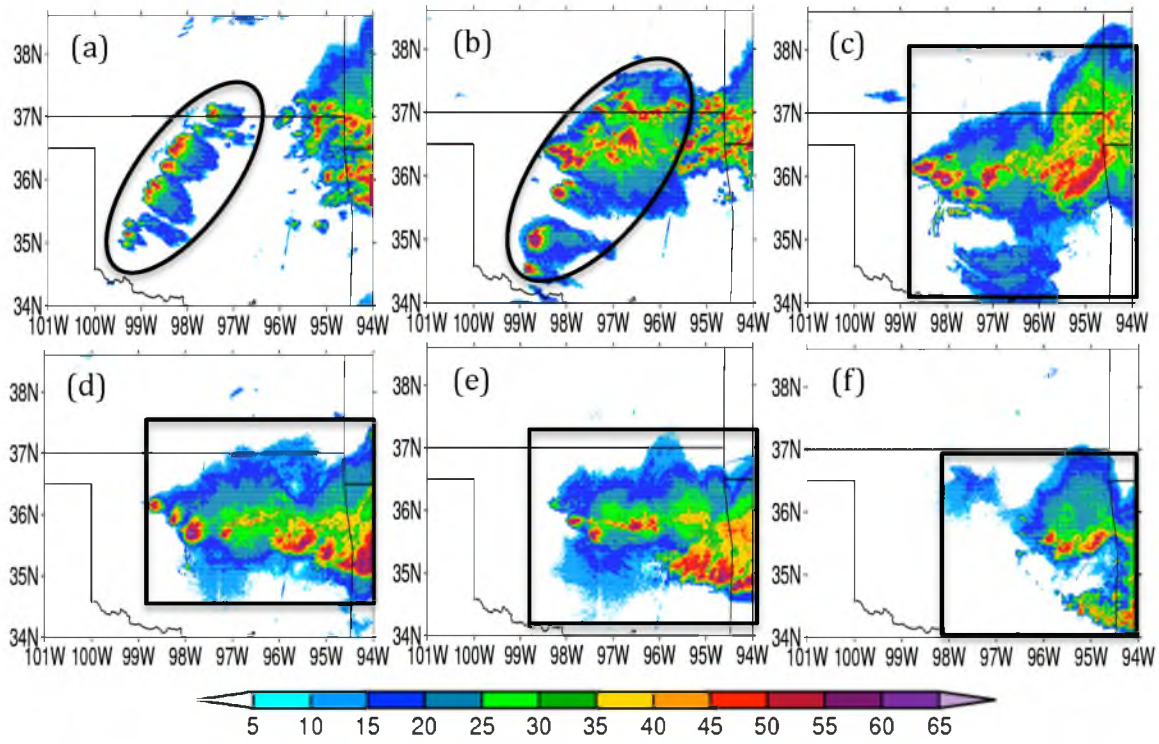

Figure 2.1. NEXRAD composite radar reflectivity observations at (a) 2100 UTC 23 May 2011, (b) 2300 UTC 23 May 2011, (c) 0100 UTC 24 May 2011, (d) 0300 UTC 24 May 2011, (e) 0400 UTC 24 May 2011, and (f) 0600 UTC 24 May 2011.

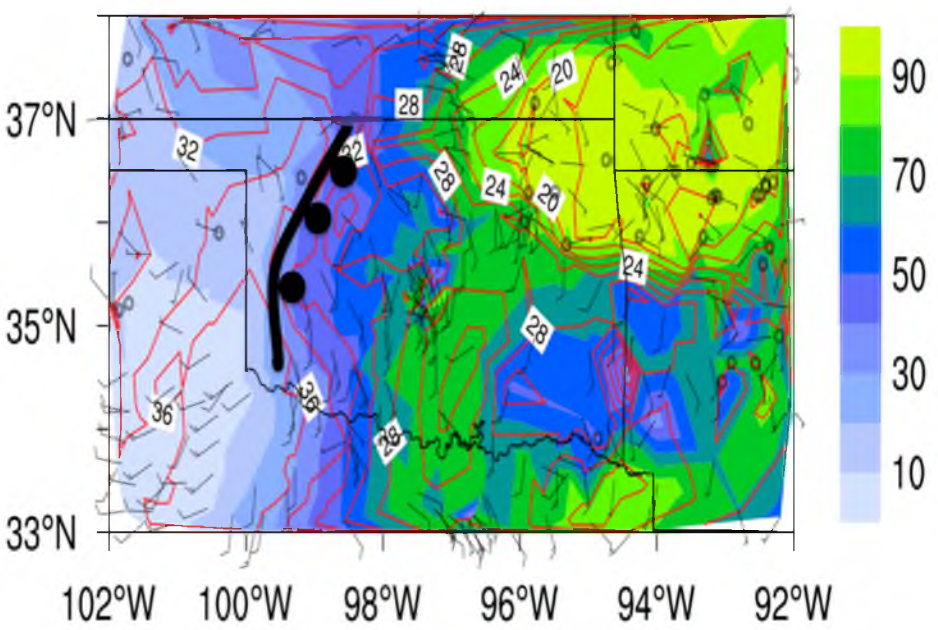

Figure 2.2. Surface wind, 1.5 m temperature (contour in °C), relative humidity (shaded, unit: %), and wind barb by Mesonet data at 2100 UTC 23 May 2011. The bold black line shows the dry line, with large black dots corresponding to the locations of three convection initiation cells.

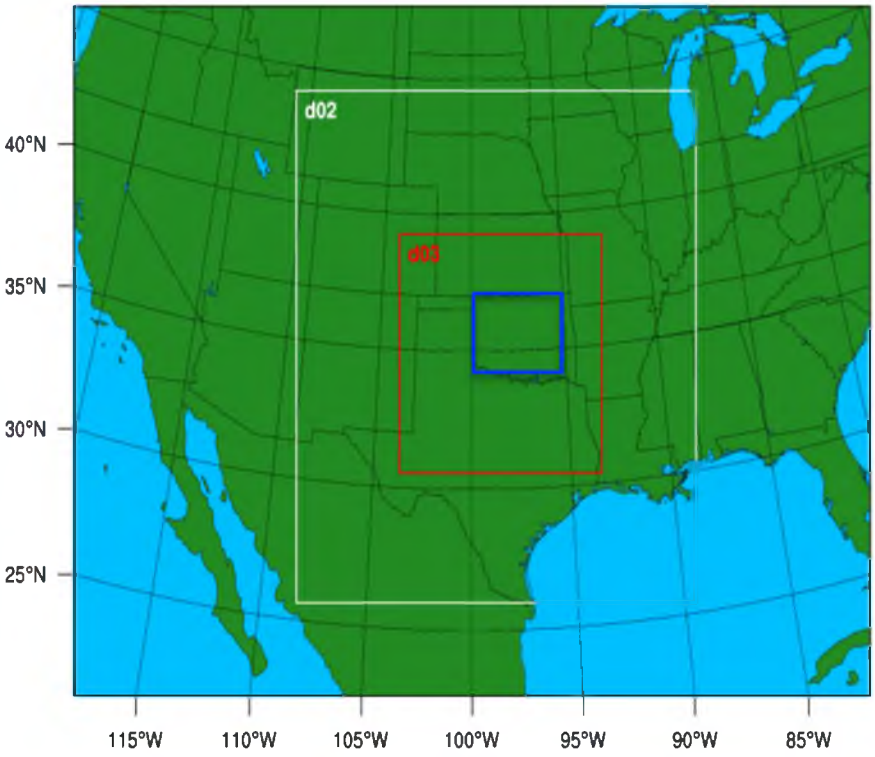

Figure 2.3. Domains used in the WRF simulations for this study. The first domain (out domain) is 12 km horizontal grid size. The second domain (labeled d02) is 4 km horizontal grid size. The horizontal grid size for the inner domain (labeled d03) is 1.33 km. The blue box zooms the domain on which evaluation was performed.

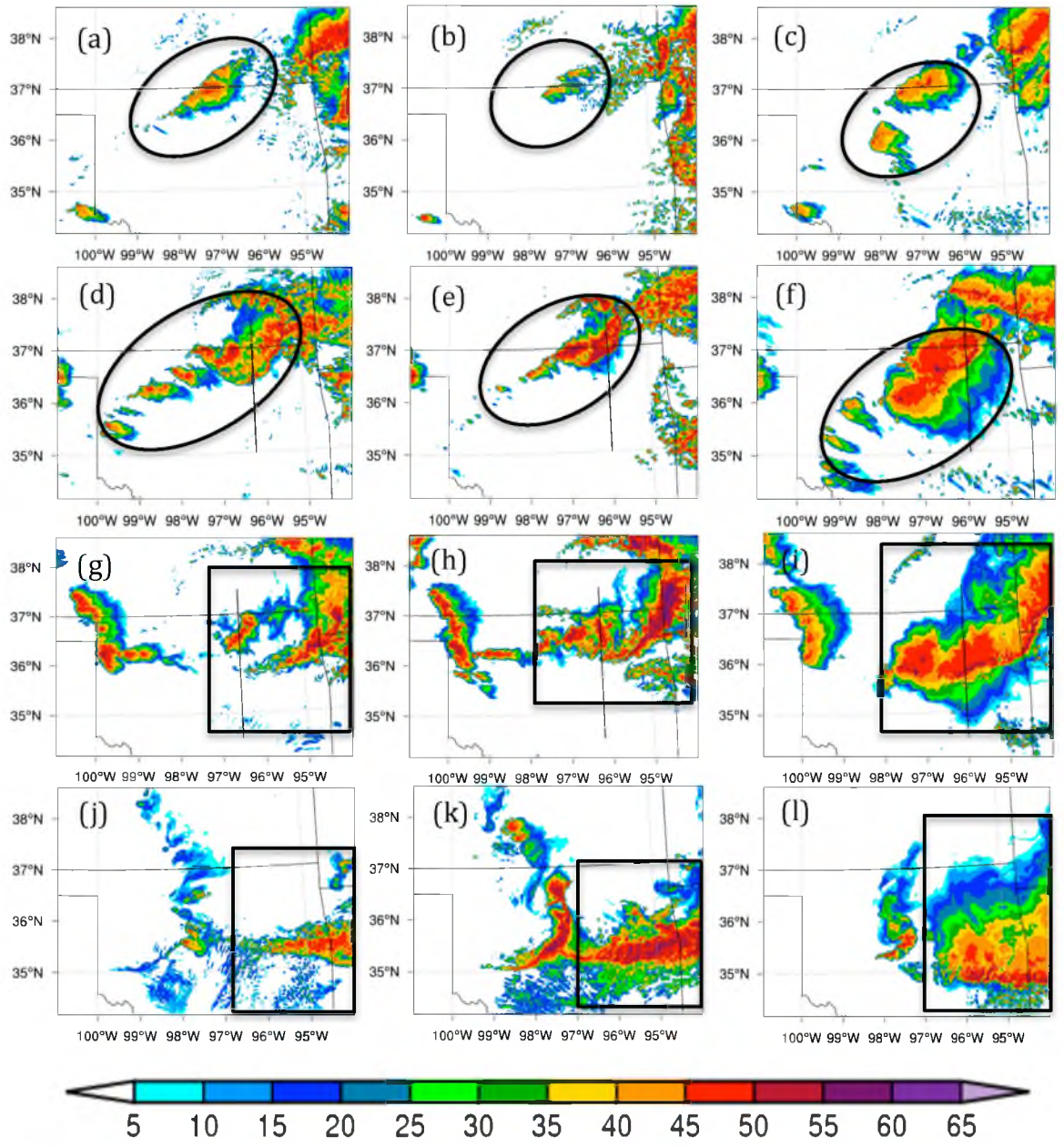

Figure 2.4. Simulated composite radar reflectivities at (a, b, c) 2100 UTC 23 May 2011; (d, e, f) 2300 UTC 24 May 2011; (g, h, i) 0100 UTC 24 May 2011; and (j, k, l) 0400 UTC 24 May 2011. (a), (d), (g), and (j) are from WRF-WSM6. (b), (e), (h), and (k) represent results from WRF-WDM6. (c), (f), (i), and (l) are from WRF-MORR.

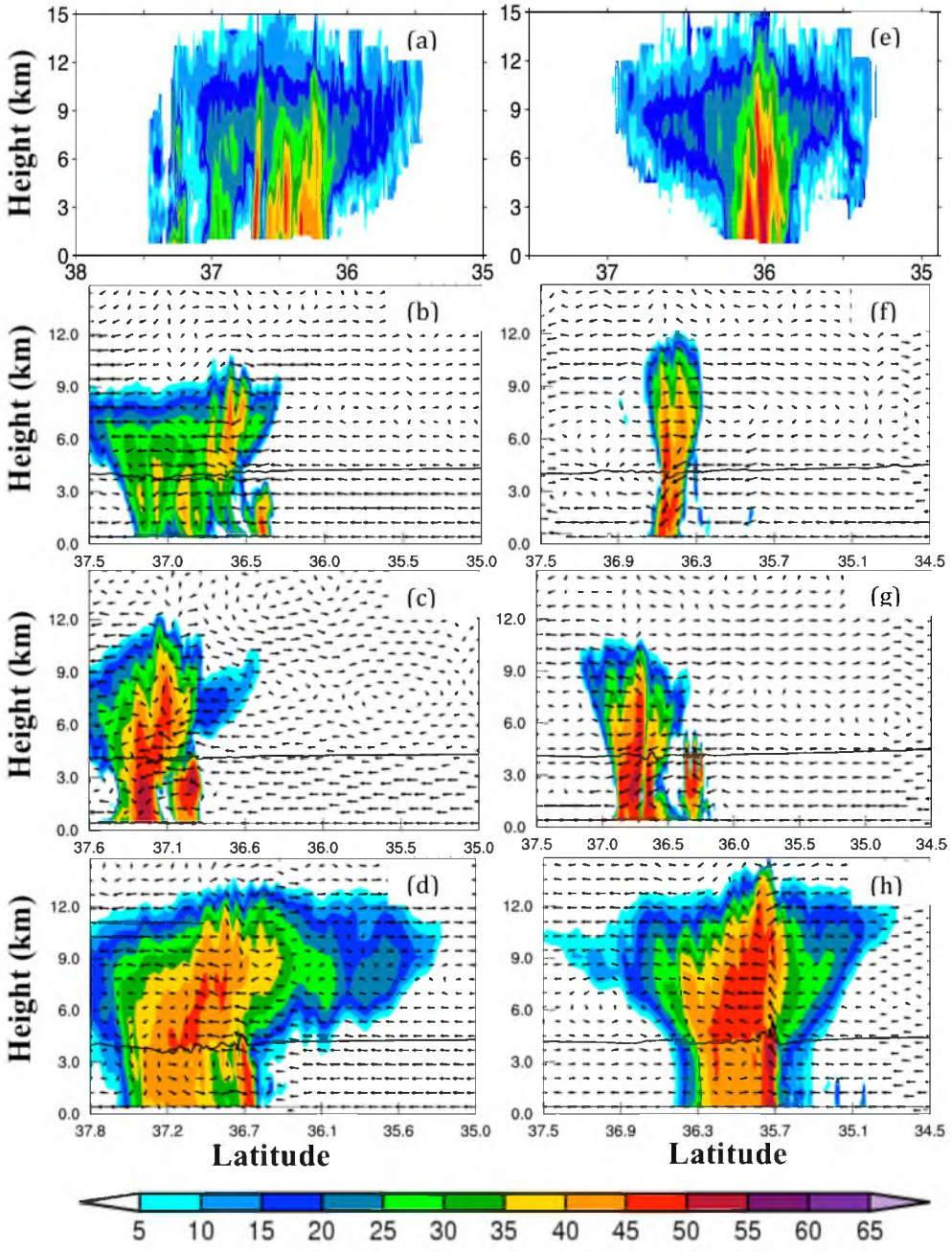

Figure 2.5. North-South vertical cross-section of radar reflectivity at 2300 UTC 23 May 2011 (a, b, c, d) and 0100 UTC 24 May 2011 (e, f, g, h)) from (a, e) NEXRAD-observations, (b, f) WRF-WSM6, (c and g) WRF-WDM6, and (d, h) WRF-MORR. The thick black lines denote melting levels.

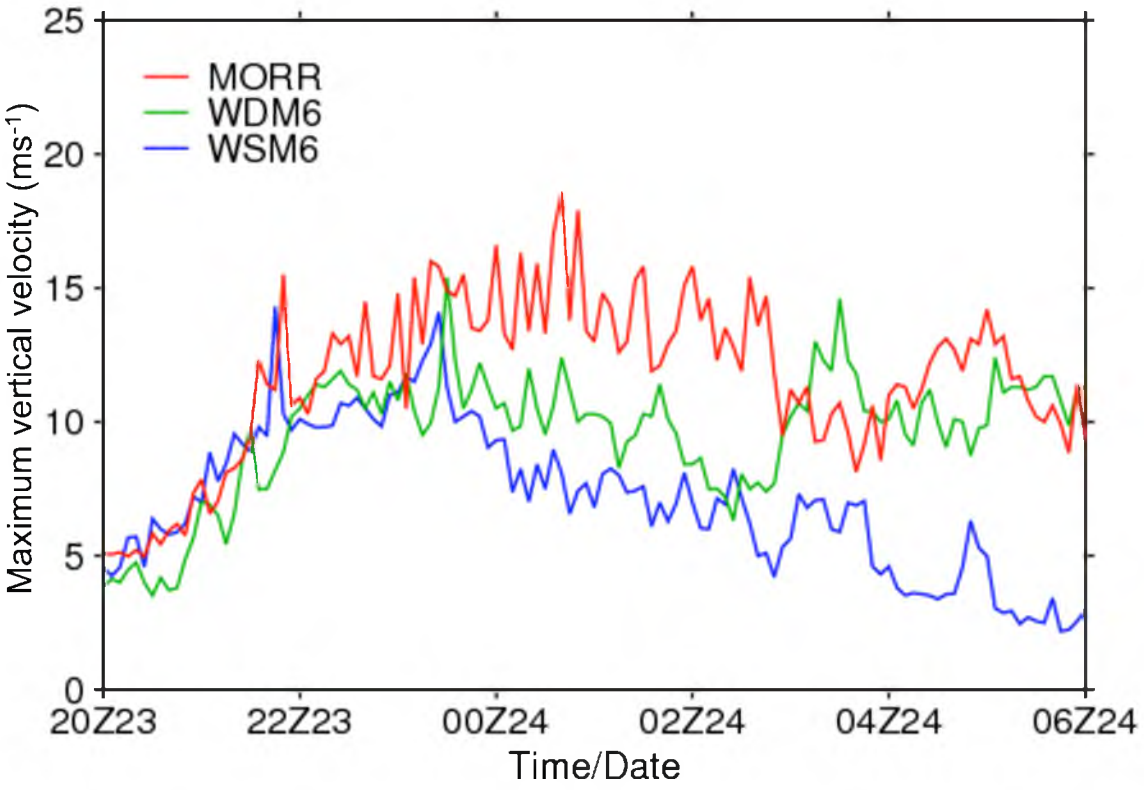

Figure 2.6. Time series of the maximum vertical air velocity (ms^{-1}) at 5 min interval during a 10-hour period (from 2000 UTC 23 May 2011 to 0600 UTC May 2011); from WRF-WSM6 (blue), WRF-WDM6 (green), and WRF-MORR (red).

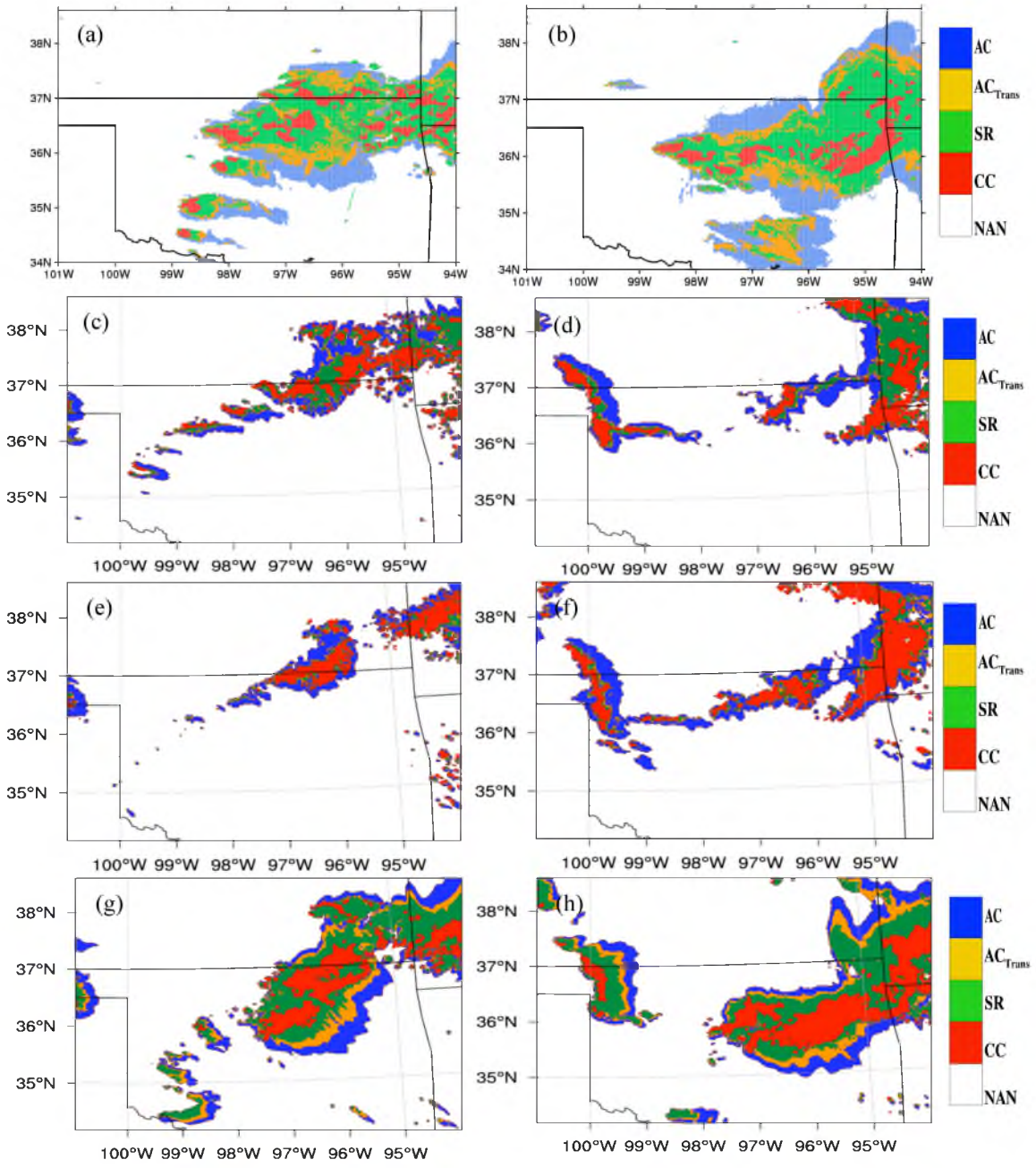

Figure 2.7. Classified three components of the convective system: Convective core (CC), Stratiform (SR) region, and Anvil clouds (AC) followed the Feng et al. (2011) method, from (a, b) NEXRAD radar observations and the WRF simulations (c, d: WSM6; e, f: WDM6; and g, h: MORR) at (a, c, e, g) 2300 UTC 23 May 2011 (b, d, f, h) and 0100 UTC 24 May 2011.

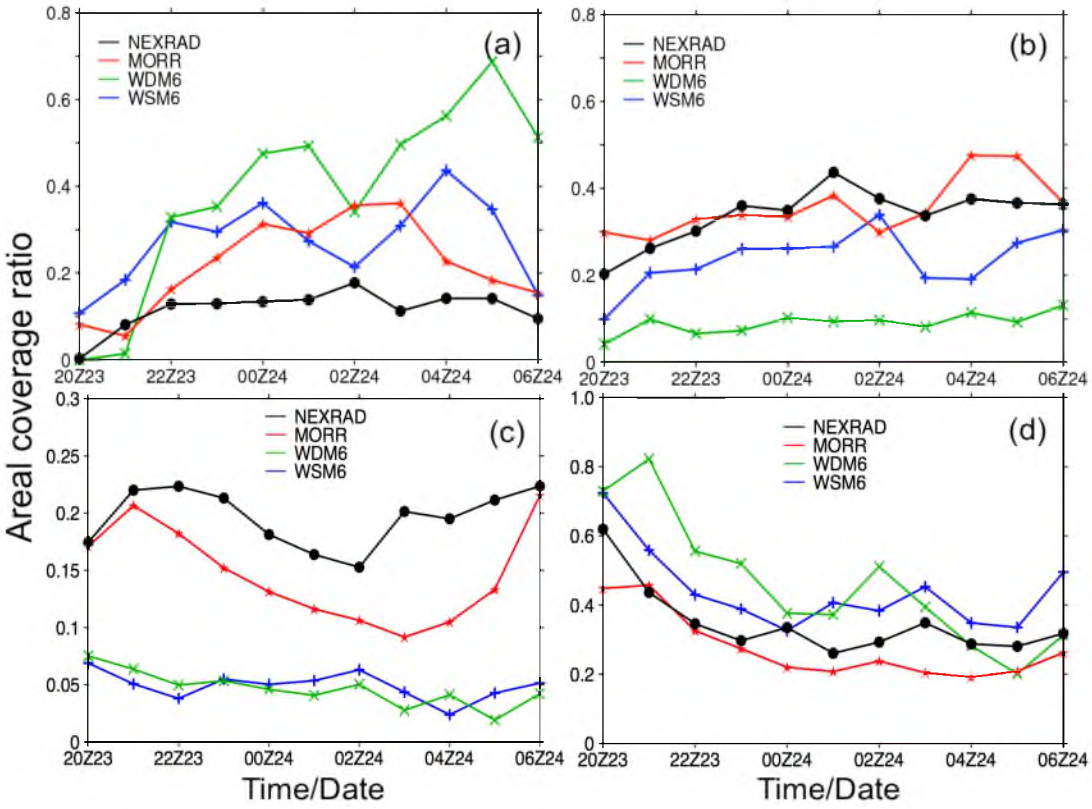

Figure 2.8. Same as Figure 2.6, except for the spatial coverage ratios (fractions) of the classified (a) convective clouds, (b) stratiform clouds, (c) transitional anvil clouds, and (d) anvil clouds to the entire MCS regions from NEXRAD observations and WRF simulations.

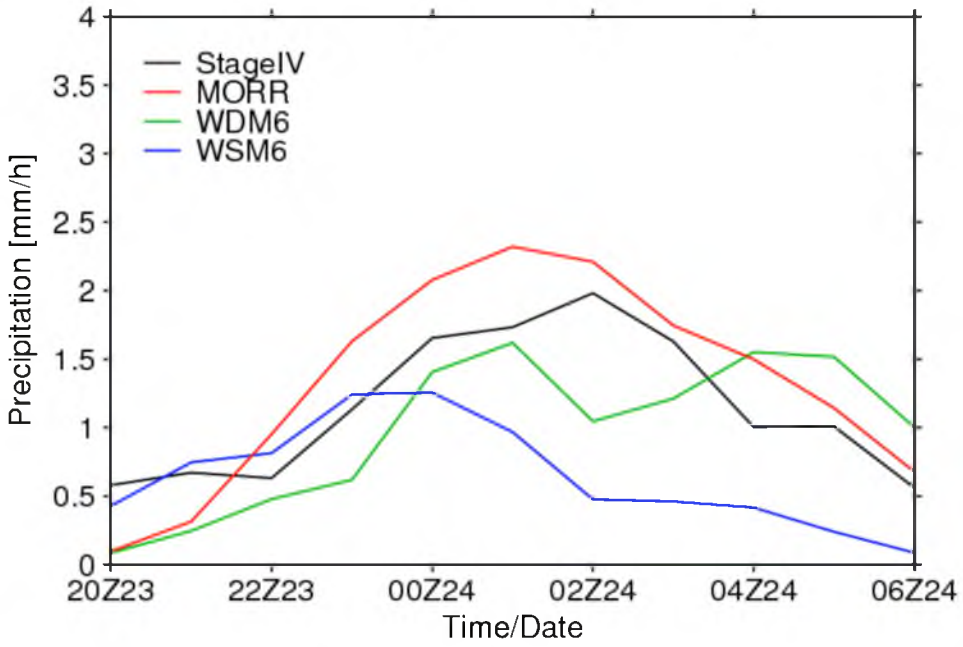

Figure 2.9. Same as Figure 2.6, except for the area averaged hourly precipitation rates (mm/hr) from NCEP Stage IV rainfall dataset (black) and WRF simulations.

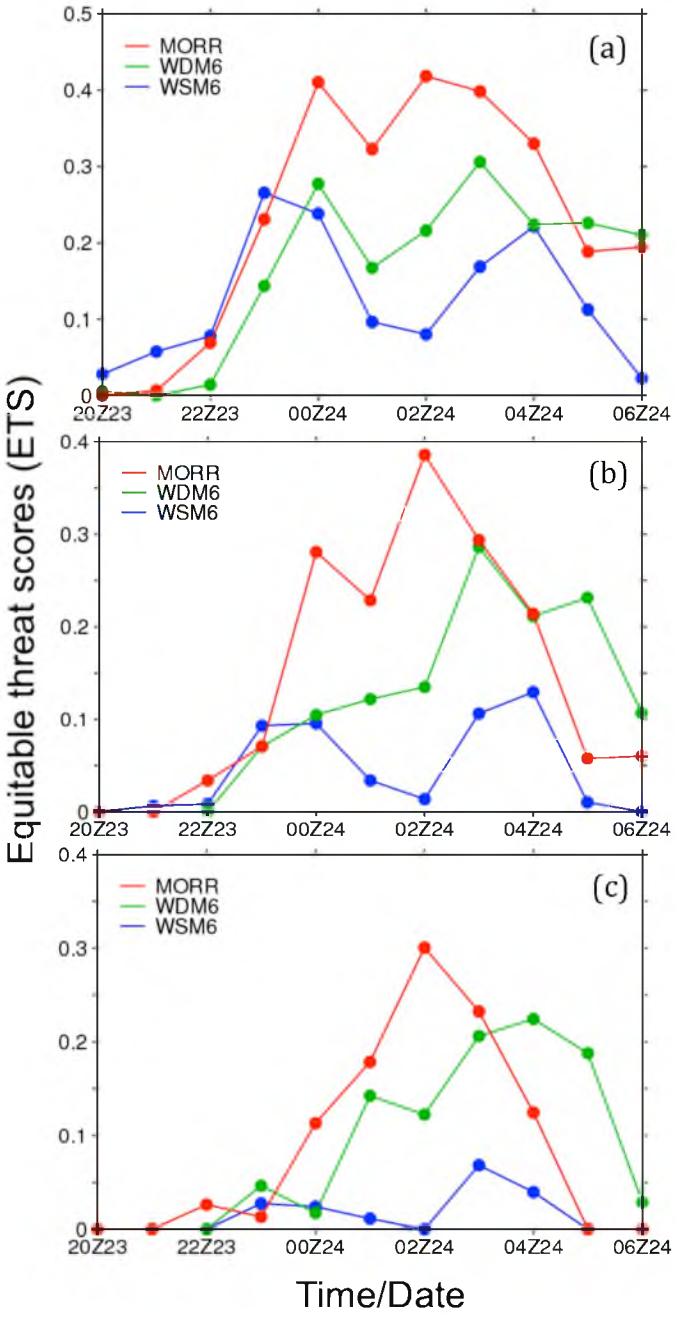

Figure 2.10. Same as Figure 2.6, except for equitable threat scores (ETS) of 1 hour accumulated precipitation from three WRF simulations with the threshold of (a) 1 mm and (b) 5 mm and (c) 10 mm.

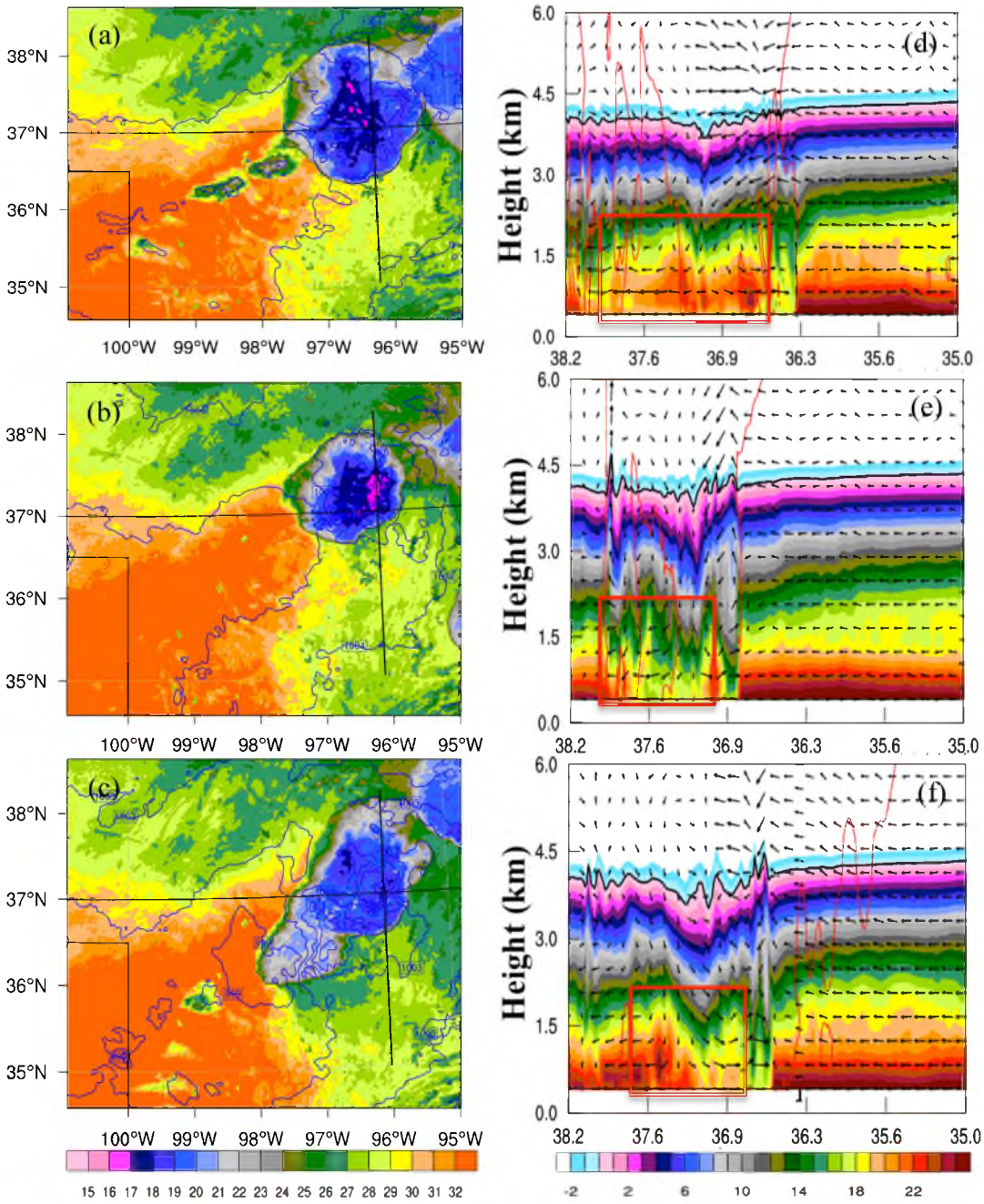

Figure 2.11. WRF simulated 2 m air temperature at 2300 UTC 23 May 2011 with (a) WRF-WSM6, (b) WRF-WDM6, and (c) WRF-MORR; (d), (e) (f) are the cross-sections of temperature along the black line showing in the left figures. The thick black lines are melting level, also with red line indicating the 0 dBZ radar reflectivity.

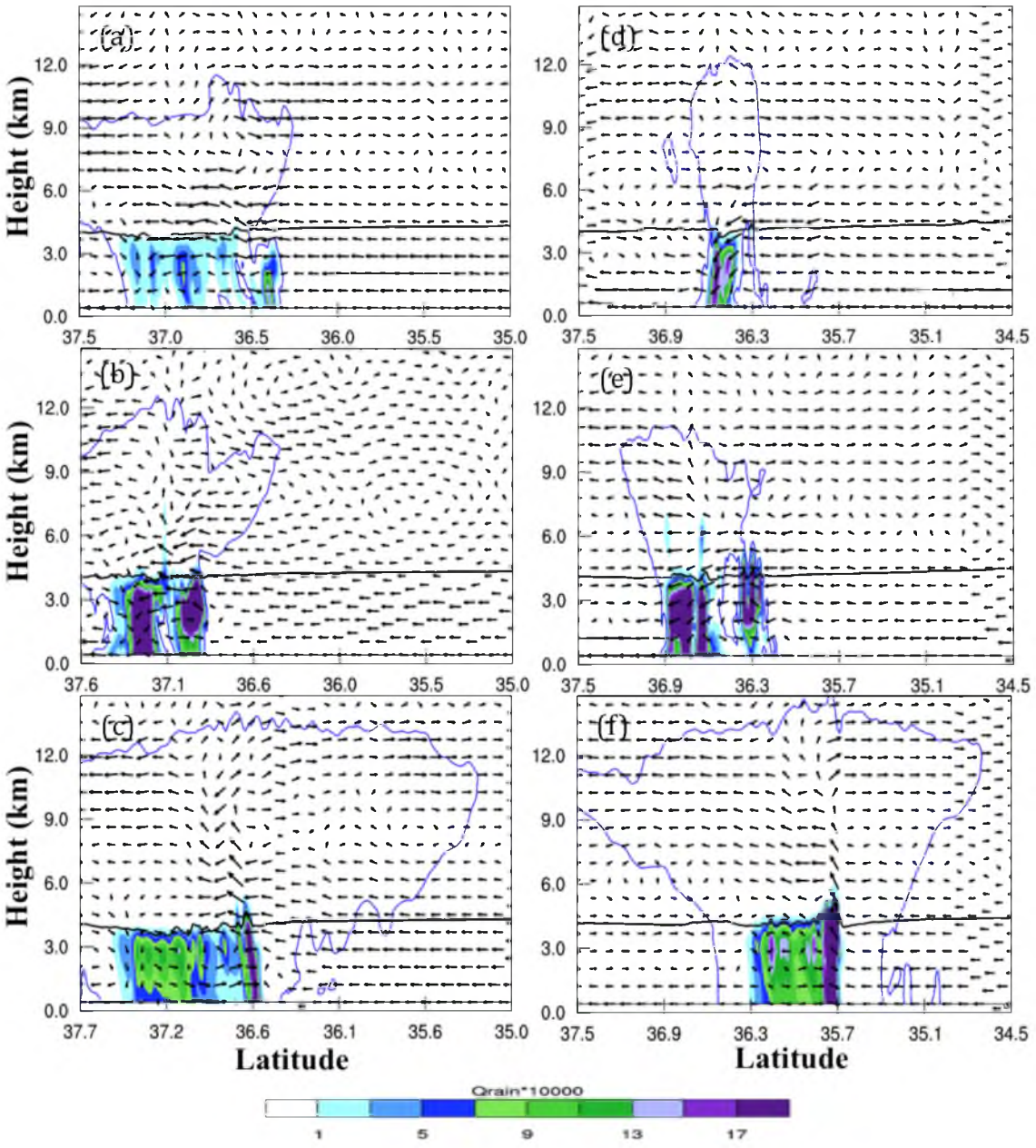

Figure 2.12. North-south cross-sections of rainwater mixing ratio along the convection system from (a, d) WRF-WSM6, (b, e) WRF-WDM6; (c, f) WRF-MORR at 2300 UTC 23 May 2011 (a, b, c) and 0100 UTC 24 May 2011 (d, e, f).

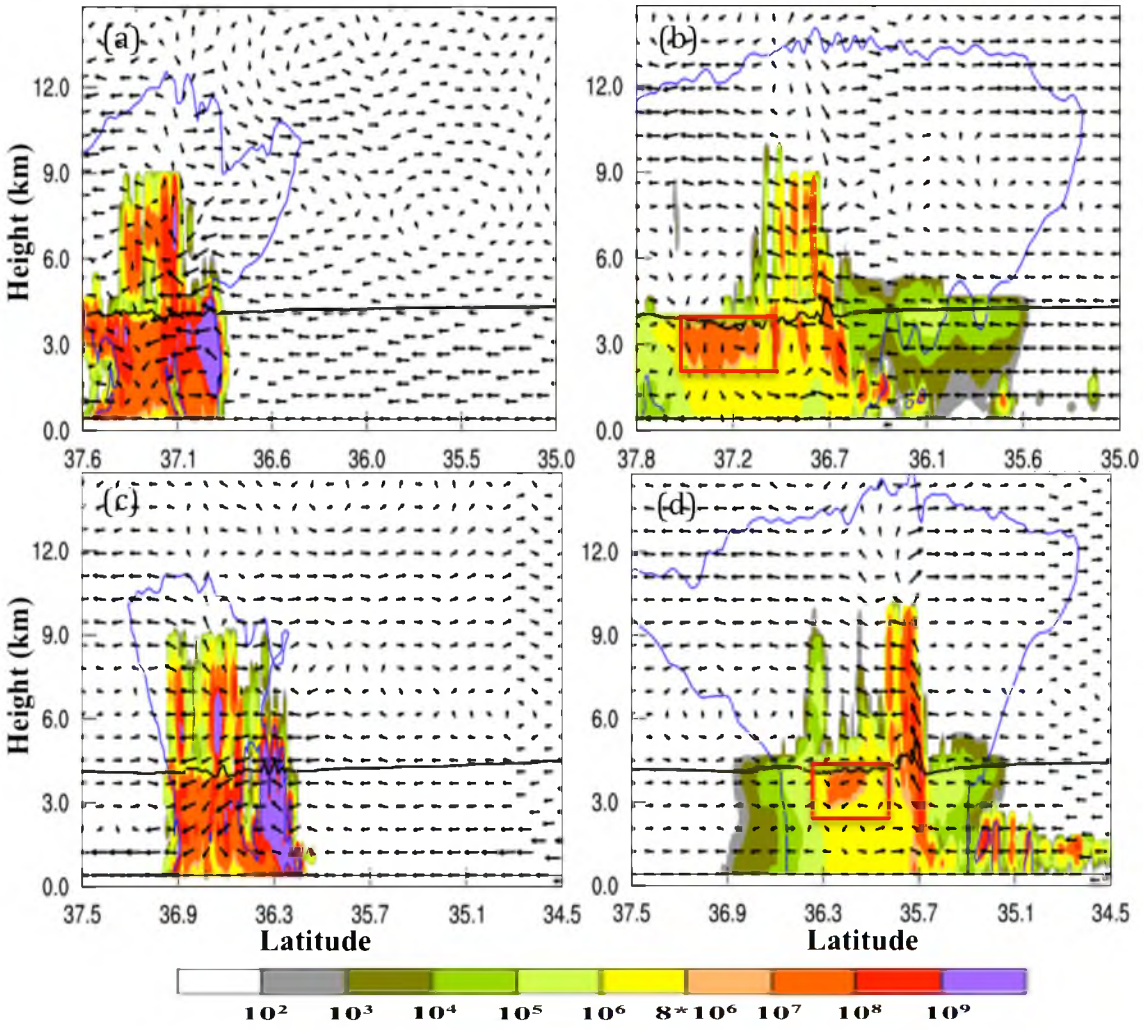

Figure 2.13. Cross-sections of rainwater intercept parameter N_{0r} along the convection system: (a, c) WRF-WDM6; (b, d) WRF-MORR at (a, b) 2300 UTC 23 May 2011 (c, d) and 0100 UTC 24 May 2011.

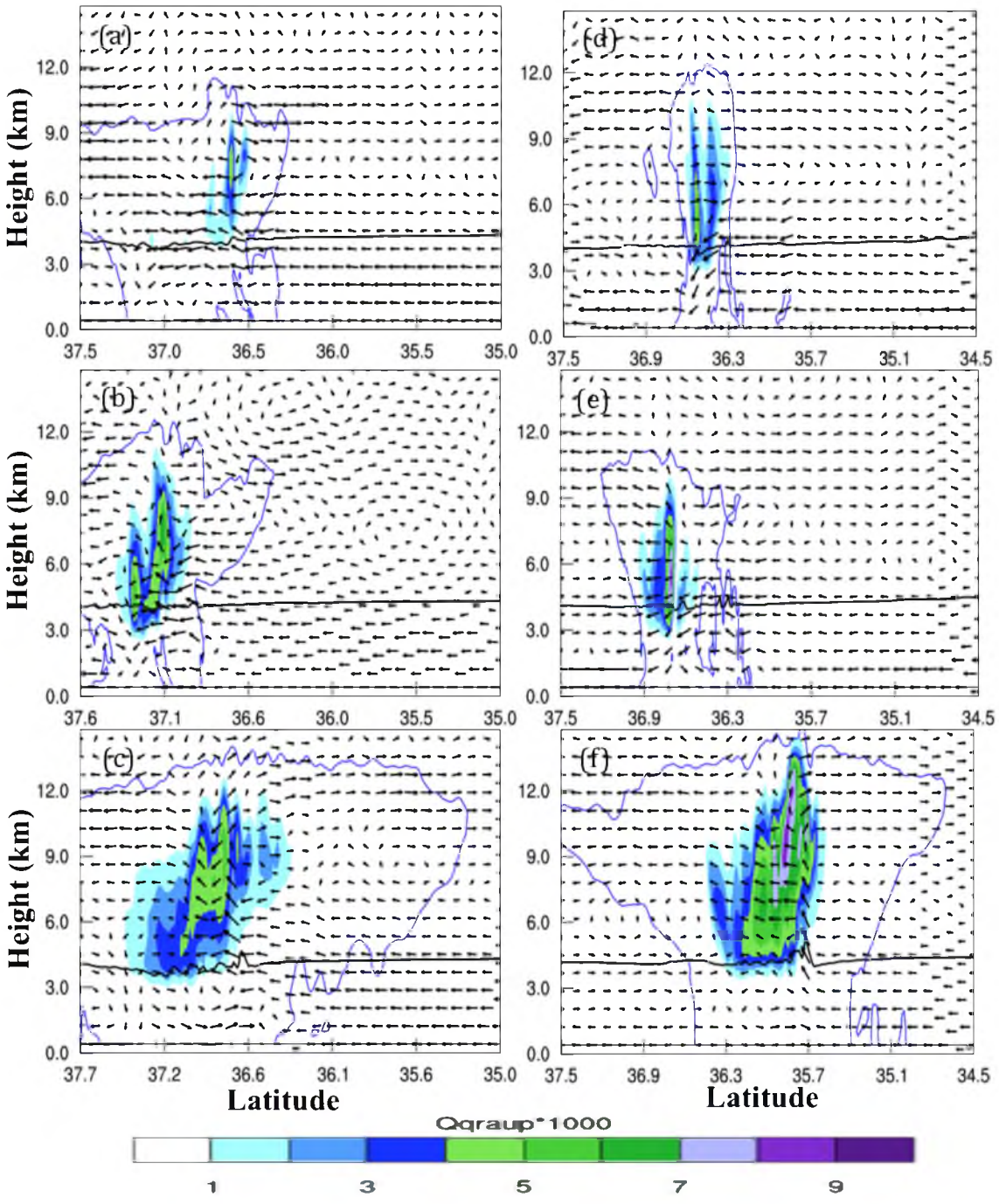

Figure 2.14. Same as Figure 2.13, except for the graupel mixing ratio.

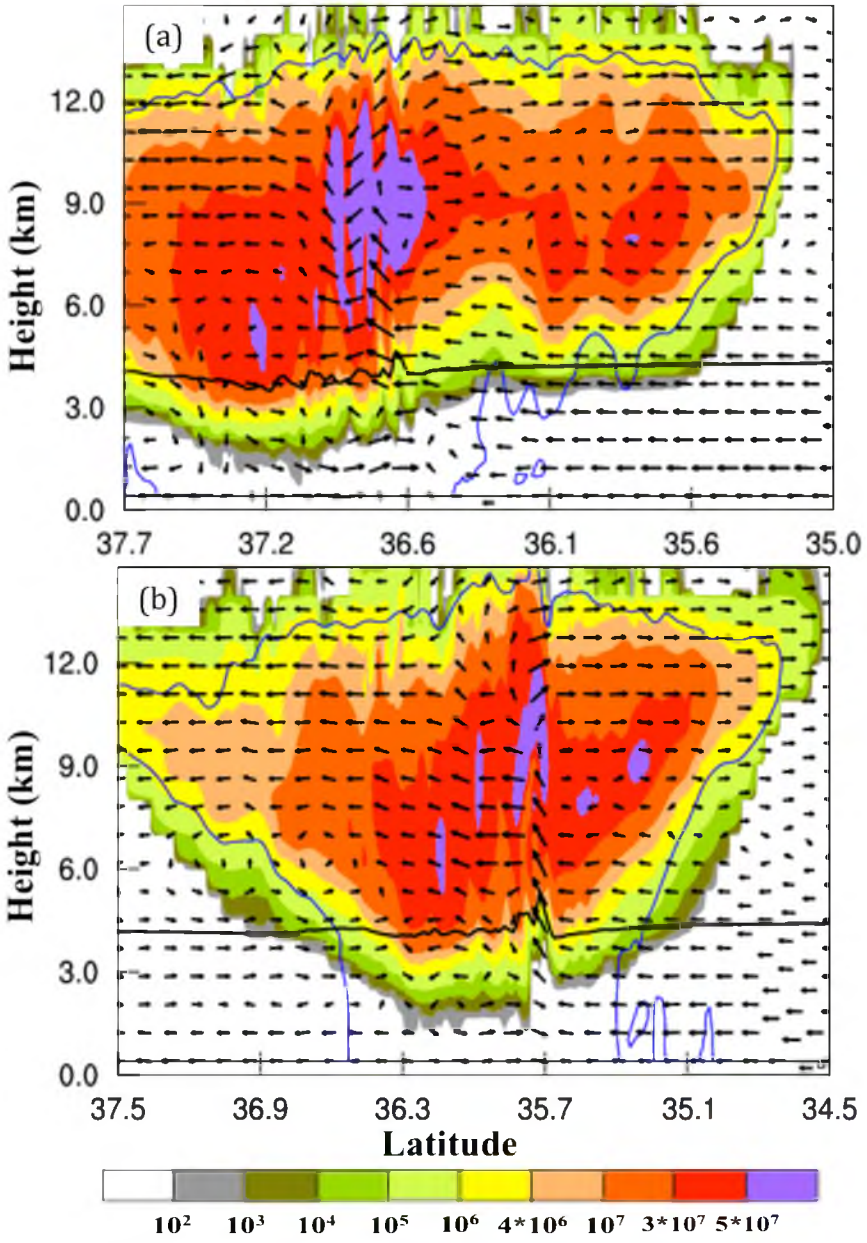

Figure 2.15. Cross-sections of WRF-MORR graupel intercept parameter N_{0g} at (a) 2300 UTC 23 May 2011 and (b) 0100 UTC 24 May 2011.

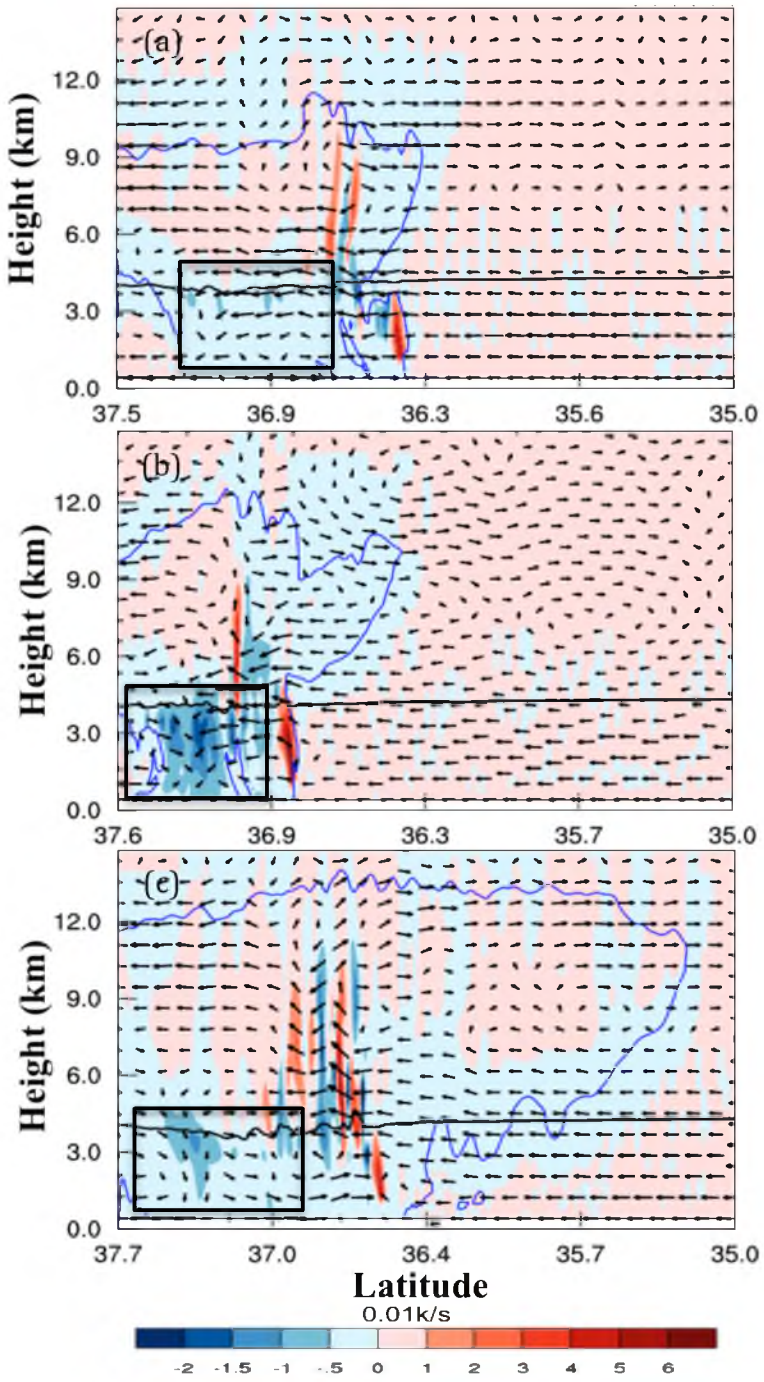

Figure 2.16. Cross-sections of diabatic heating at 2300 UTC 23 May 2011 for (a) WRF-WSM6, (b) WRF-WDM6, and (c) WRF-MORR.

CHAPTER 3

SENSITIVITY TO PRECIPITATING PARAMETERS AND THE TYPE OF THE DENSE ICE

In the previous chapter, we examined the sensitivity of numerical simulations of the MCS to different microphysical schemes. However, as mentioned in the introduction, different microphysical schemes vary in many aspects. For instance, they may utilize different representations of M-D (mass-diameter) and V-D (velocity-diameter) relationships, density of hydrometeors, raindrop breakup, collection efficiency, etc. Uncertainties in all of these aspects could impact the simulations. Thus, an open question is: how are the simulated MCS properties sensitive to the assumptions and parameters used in BMPs? In order to answer this question, in this chapter, we present some additional numerical simulation results.

3.1 Sensitivity to Precipitating Particles Parameters

First, three microphysical schemes (WSM6, WDM6, and MORR) are carefully examined. We found that the main differences (except for the moments representation) among these three schemes are their treatments of the V-D relationship and densities of precipitating particles. Even though all three schemes use the same equation $V=aD^b$ to represent the hydrometeor V-D relationship, they utilize different a and b values (the

empirical efficiencies). The values of a and b, as well as the densities of precipitating particles (graupel, snow, and rain) are listed in Table 3.1 and Table 3.2 for WSM6 and WDM6, and MORR, respectively.

In order to examine the sensitivity of the simulated MCS properties to precipitating particle parameters and also provide additional insights on the reliability of the conclusions in the last chapter, two additional WRF simulations with WSM6 and WDM6 schemes are conducted with the precipitating hydrometeor parameters (V-D relationship, density of ice hydrometeors) provided by the MORR scheme.

Figure 3.1 shows the composite radar reflectivity of these two simulations. Compared with the results in Figure 2.4, the convection intensity, structure, and coverage do not show much difference. Therefore, the different representation of precipitating hydrometeor parameters (V-D relationship, density) does not have much influence on the simulations of the MCS, implying that the differences in moments are the major reasons for the differences in the results presented in Chapter 2.

3.2 Sensitivity to Choices of Dense Ice

In addition, previous studies have shown that the characteristics of the different ice hydrometeors used in cloud-scale simulations can greatly influence the precipitation distribution and the resulting downdraft intensity (Cotton et al. 1982; McCumber et al. 1991; Straka and Anderson 1993). Among 3ice schemes, the use of hail or graupel as dense riming ice also impacts simulations significantly (Bryan and Morrison 2012). Therefore, we also made another simulation to examine the sensitivity of the WRF simulations to the choice of the dense ice in the microphysical schemes.

In the WRF model, the MORR microphysical scheme provides the flexibility of using hail or graupel as the dense riming ice species. The main difference of hail from graupel is that the hail has larger density and faster fall speed. Bryan and Morrison (2012) indicated that the simulation with hail produces more realistic results than that with graupel for a squall line convective system. As we stated in Chapter 2, the largest defect of the WRF-MORR simulation is the unrealistically large CC area with a positive radar reflectivity bias aloft. In order to evaluate the influences of different type of dense ice in the simulations, a new experiment (H-MORR) using the Morrison scheme with hail (instead of graupel as in WRF-MORR) as dense ice species is conducted.

Figure 3.2 shows the snapshots of composite radar reflectivity at the initiation stage (Fig. 3.2a), developing stage (Fig. 3.2b), mature stage (Fig. 3.2c), and dissipating stage (Fig. 3.2d). Compared with the results from WRF-MORR (Fig. 2.4c, f, i and l), H-MORR produces the same convection life cycle, similar convection coverage, but a different intensity distribution. The largest difference between H-MORR and WRF-MORR is the size of the region with the medium to high radar reflectivity values (> 40). The high dBZ zone is much narrower in H-MORR than in WRF-MORR. However, this narrow zone agrees with the NEXRAD observations better (Fig. 2.1). Overall, H-MORR performs better than WRF-MORR for the convection structure, but it still overestimates the dBZ values compared with the NEXRAD observations.

To illustrate the convection's vertical structure, the dBZ cross-sections (along the black lines shown in Fig. 3.2 b and c) are shown in Figure 3.3a and b. Note that there was an issue in the dBZ vertical structure of WRF-MORR: due to the large amount of graupel accumulation caused by the slower fall speed and graupel melting below the melting

level, there are high dBZ values aloft from the melting level to the middle and upper troposphere in the SR region. This problem, however, disappears in H-MORR. The high dBZ in H-MORR is also concentrated into a narrower region but is more realistic compared to NEXRAD observations (Fig. 2.5a and e). The sizes of the convective system produced by H-MORR and WRF-MORR are similar.

Figure 3.4 displays 1-hour accumulated precipitation amounts from WRF-MORR (Fig. 3.4a and b) and H-MORR (Fig. 3.4c and d), compared with Stage-IV precipitation data (Fig. 3.4 e and f). H-MORR produces more intense precipitation than WRF-MORR does, especially over the convective core region. The precipitation coverage produced by H-MORR (Fig. 3.4 c, d) is smaller than WRF-MORR (Fig. 3.4a and b) produced. Compared with the Stage IV data, H-MORR concentrated more precipitation in the CC region and less in the SR region.

It seems that replacing graupel by hail improves the simulated convection structure. Nevertheless, why does the use of hail produce different results compared with the use of graupel? In order to obtain additional insights, the hydrometer amounts and distributions are examined. Figure 3.5 shows the time series of domain-averaged hydrometeor paths produced by WRF-MORR and H-MORR. The hydrometeor path is defined as the vertical integral of the hydrometeors mass per unit area.

$$Hp_i = \int_0^{Z_{top}} \rho_i q_i \, dz = \int_{p_{top}}^{p_{surface}} \frac{p}{RT} q_i \, dp = \sum_{l=0}^{l=n} \frac{p(l)q(l)}{RT_l} [(p(l) - p(l+1))] \qquad (3.1)$$

where "i" represents the specific kind of hydrometeor (rain, graupel, snow, etc.), "l" indicates the model levels. Compared with WRF-MORR (Fig. 3.5a), the snow path in H-

MORR (Fig. 3.5b) is slightly larger (the maximum value is 0.9 kg/m^2 in H-MORR versus 0. 8 kg/m^2 in WRF-MORR). In addition, graupel dominates the ice-phase hydrometeors in WRF-MORR (Fig. 3.5s), while this is not the case in H-MORR (Fig. 3.5b). Specifically, in H-MORR, the hail path is larger than the snow path before the mature stage (about 0000 UTC 24 May 2011), while the snow path became larger at the mature and dissipation stages. These differences may be caused by the different parameters such as V-D relationship and the density among graupel, hail, and snow. The density is 100 kg/m^3 for snow, 400 kg/m^3 for graupel, and 900 kg/m^3 for hail. The V-D relationship for hail is $V=114.5D^{0.5}$, $V=19.3D^{0.37}$ for graupel and $V=11.72D^{0.41}$ for snow. Obviously, hail has a larger fall speed compared with snow and graupel. Hail and graupel are produced mainly by the riming processes in the convective core region. After production, they are transported and advected to the outer regions as they fall. The larger fall speed for hail means it has a shorter suspended time. Once it arrives at the melting level, it will be melted and converted to rain, and a small amount of hail also arrives at the ground. Because of this, the domain-averaged hail hydrometeor path is smaller than graupel, especially during the mature and dissipating stages of the MCS. Large amounts of hail in the CC region contributed to the intense precipitation there (Fig. 3.4c and d). In the SR region, deposition and aggregation are the primary mechanisms for production of ice (Churchill and Houze 1984). Therefore, H-MORR and WRF-MORR produced similar amounts of snow and ice. The hail mixing ratio and intercept parameter N_{0h} in H-MORR (shown in Fig. 3.6) supports this conclusion. The hail is concentrated into a narrow CC region, while its number concentration is less than the number concentration of graupel in WRF-MORR.

The snow mixing ratio (Fig. 3,7a and c) and intercept parameter N_{0s} (Fig. 3.7b and d) for both WRF-MORR (Fig.3.7 a and b) and H-MORR (Fig. c and d) are shown in Figure 3.7. The mixing ratio of snow in H-MORR is larger than that in WRF-MORR. This is reasonable because the primary mechanisms of production of the snow are deposition and aggregation. Most of the snow is produced in the SR region. In WRF-MORR, a large amount of graupel is available in the SR region, while snow and graupel may compete for the supersaturated water vapor; at the same time, graupel will collect some snow by aggregation. As a result, the mixing ratio of snow is smaller in WRF-MORR compared with that in H-MORR. More snow in H-MORR is transported into the outer region by the middle and upper level horizontal wind. As a result, a broad convection structure appears in the middle and upper levels.

Overall, replacing graupel by hail improved the prediction of the convection structure, even though it also overestimated the precipitation, especially in the CC region. The differences between the two simulations appear to be mainly caused by the density and V-D relationship differences between hail and graupel. The faster fall speed of hail made the precipitation concentrated into a narrower CC region. Since the less dense graupel can spread into a larger area, it (WRF-MORR) overestimates the dBZ values. Graupel/hail processes appear to play important roles in determining the storm structure. Wu et al. (2013) suggests that a 4-ice (hail, graupel, snow, ice) MP scheme is needed in order to properly represent MCS properties.

Table 3.1. Parameters of V-D relationship and density of rain, graupel, and snow for the WSM6 and WDM6 scheme.

Species	a	B	Density (kg/m^3)
Rain	841.9	0.8	1000
Graupel	330	0.8	500
Snow	11.72	0.41	100

Table 3.2. Parameters of V-D relationship and density of rain, graupel, and snow for the Morrison scheme.

Species	a	B	Density (kg/m^3)
Rain	841.99667	0.8	997
Graupel	19.3	0.37	400
Snow	11.72	0.41	100

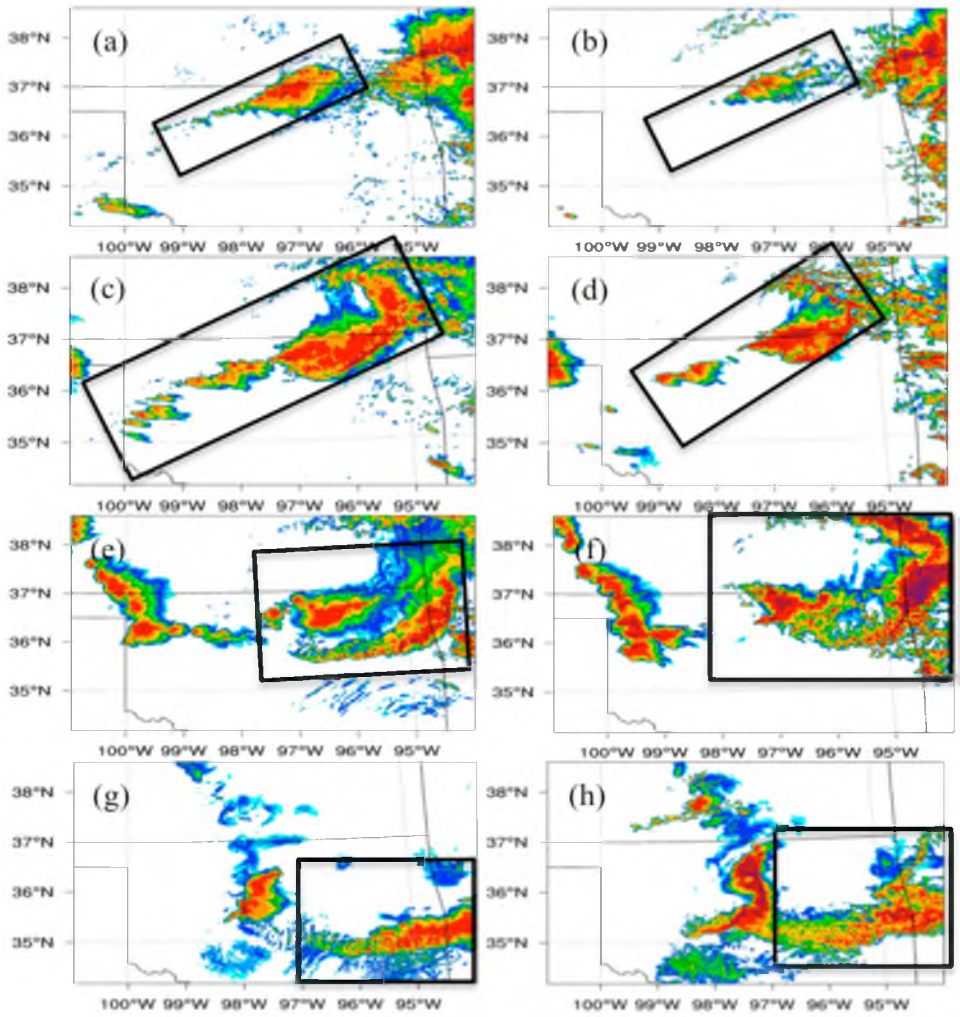

Figure 3.1. The WRF model simulated composite radar reflectivity at (a, b) 2100 UTC 23 May 2011 (c, d) 2300 UTC 24 May 2011; (e, f) 0100 UTC 24 May 2011 and (g, h) 0400 UTC 24 May 2011; Left column figures (a, c, e, g) are from WRF-WSM6, right column figures (b, d, f, h) are from WRF-WDM6.

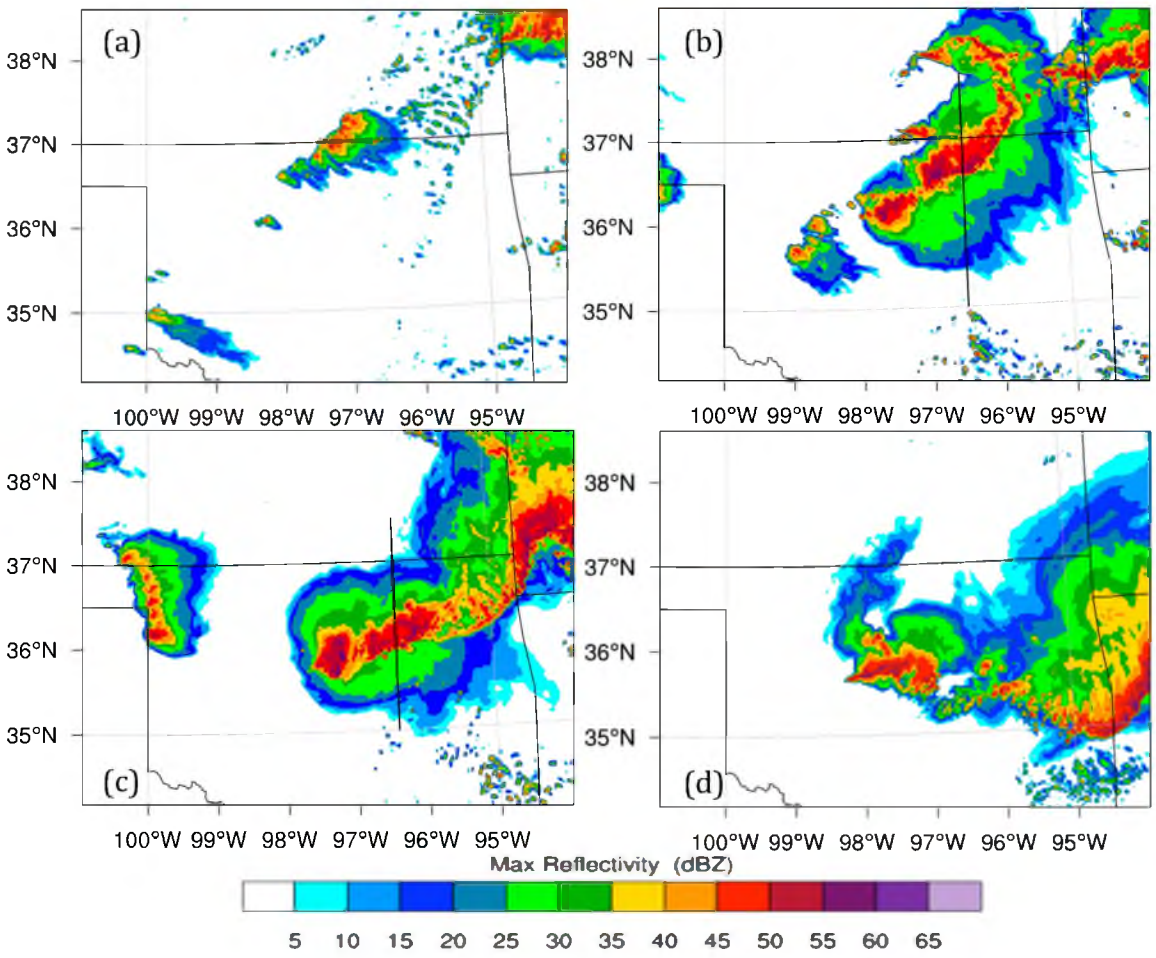

Figure 3.2. Composite radar reflectivity from H-MORR simulation at a): 2100 UTC 23 May 2011, b): 2300 UTC 23 May 2011, c): 0100 UTC 24 May 2011, and d): 0400 UTC 24 May 2011.

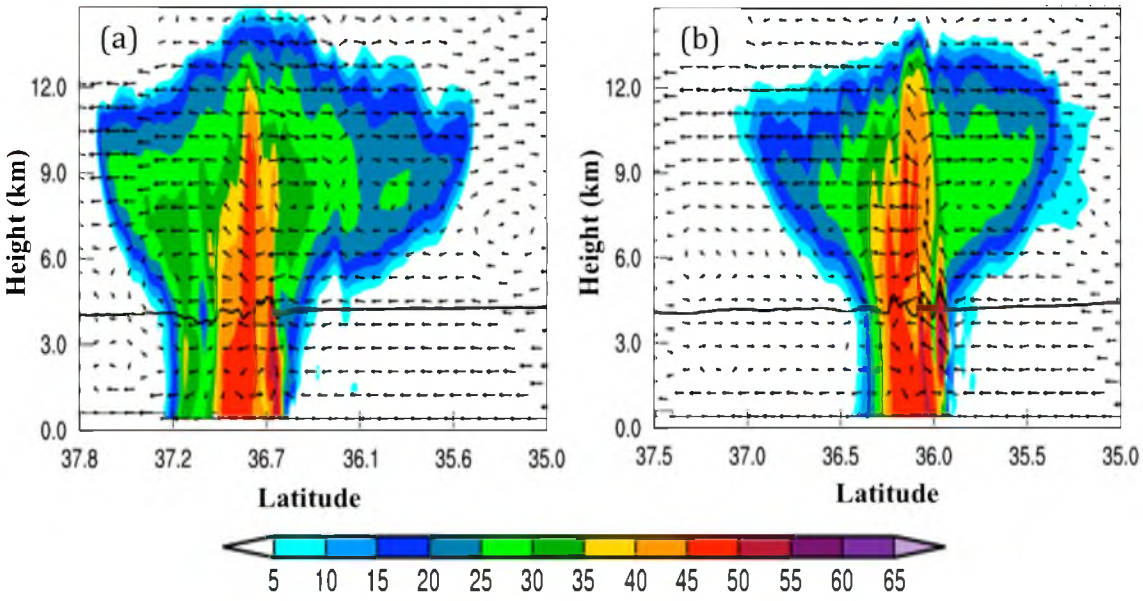

Figure 3.3. The north-south cross-sections of radar reflectivity from H-MORR simulation at a): 2300 UTC 23 May 2011, b): 0100 UTC 24 May 2011.

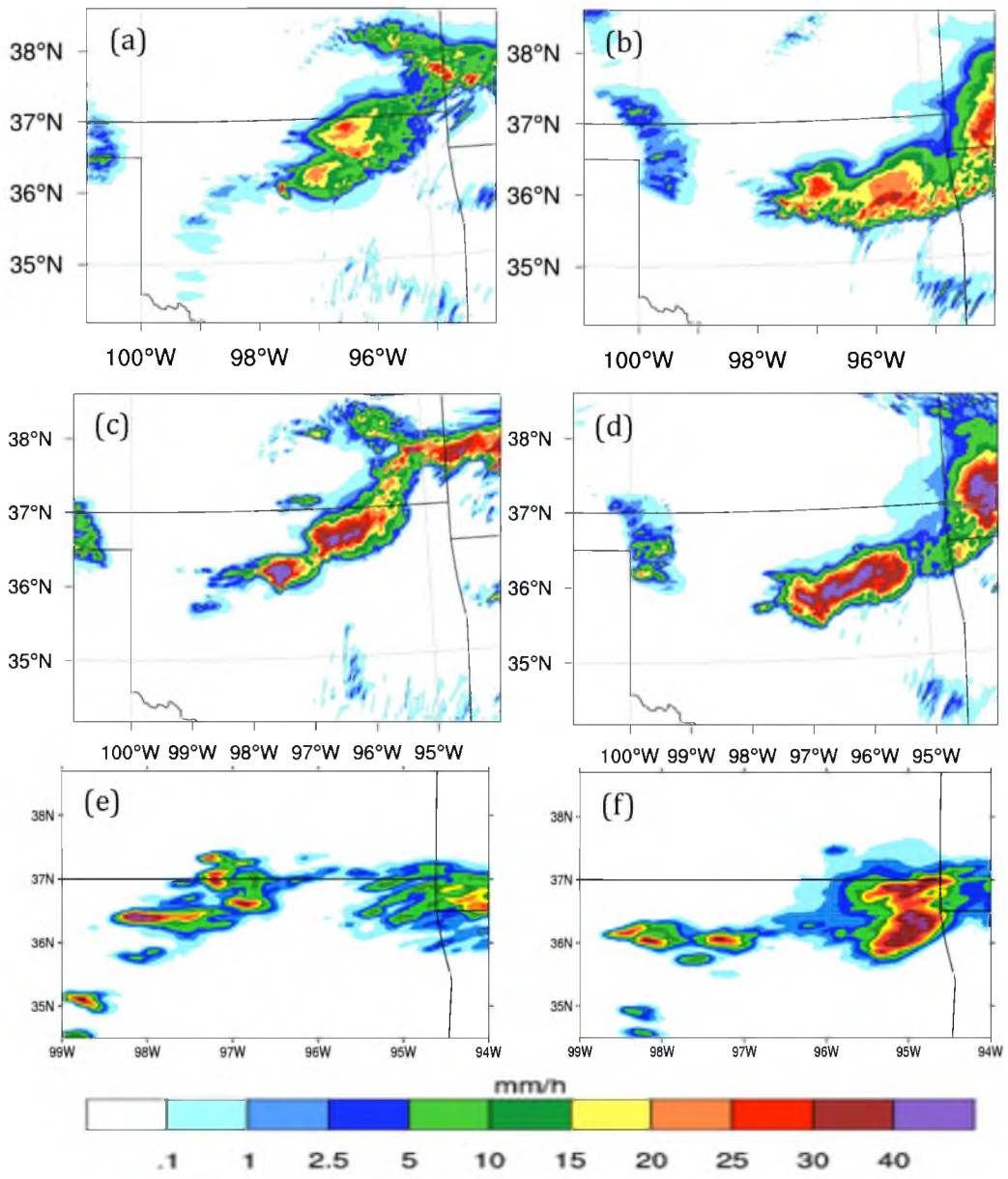

Figure 3.4. Hourly precipitation amount from simulations, WRF-MORR (a, b), H-MORR (c, d), and from Stage-IV rainfall dataset (e, f) at (a, c, and e): 2300 UTC 23 May 2011 and (b, d, and f): 0100 UTC 24 May 2011.

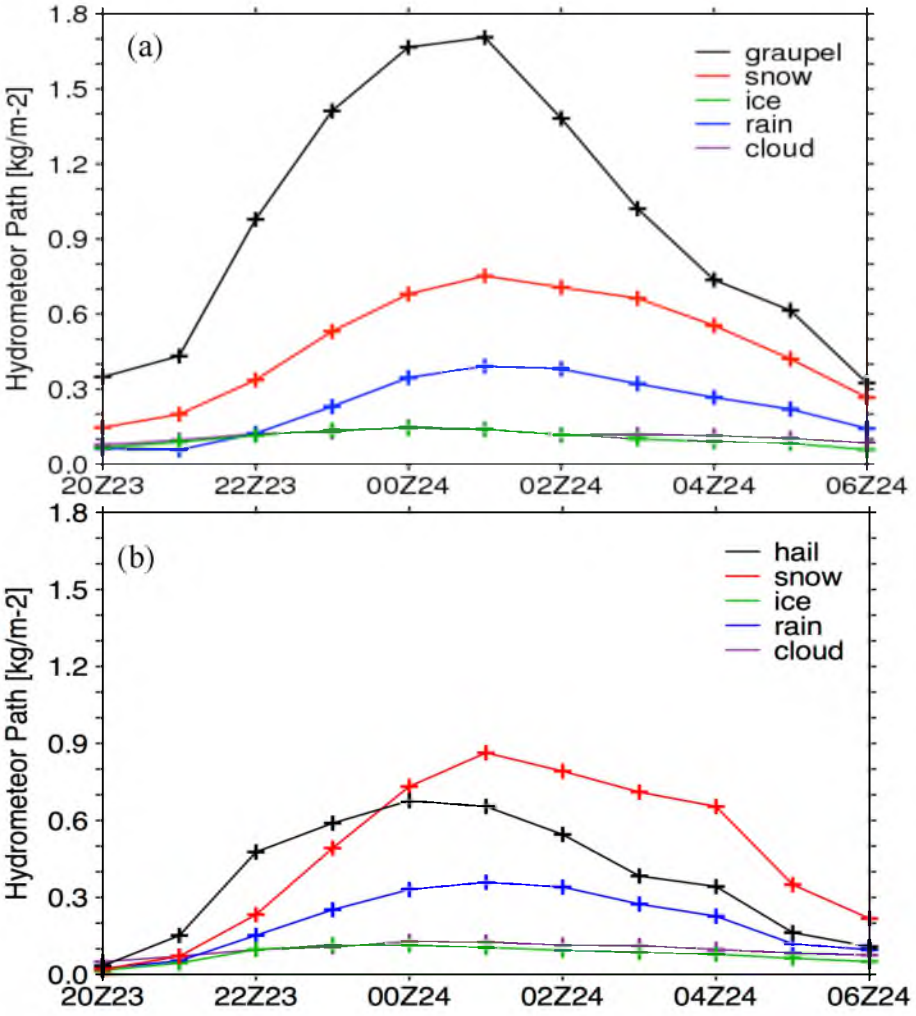

Figure 3.5. Time series of domain-averaged hydrometeor path of hail (black line), snow (red line), ice (green line), rain (blue line), and cloud (purple line) from WRF-MORR (a) and H-MORR (b).

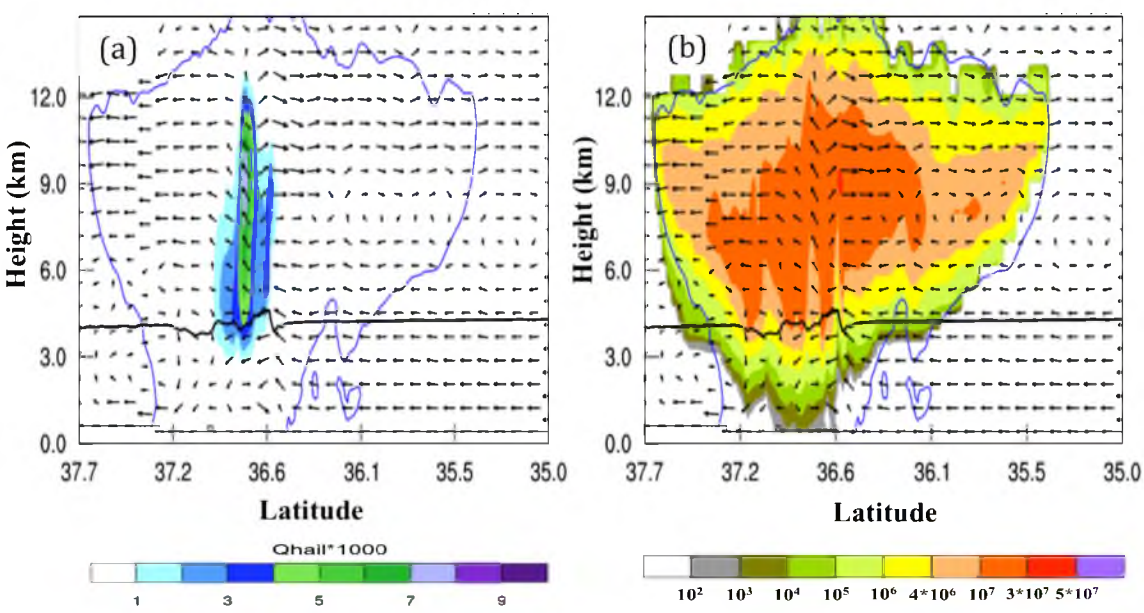

Figure 3.6. Cross-section of hail mixing ratio (a) and intercept parameter N_{0h} (b) at 2300 UTC 23 May 2011.

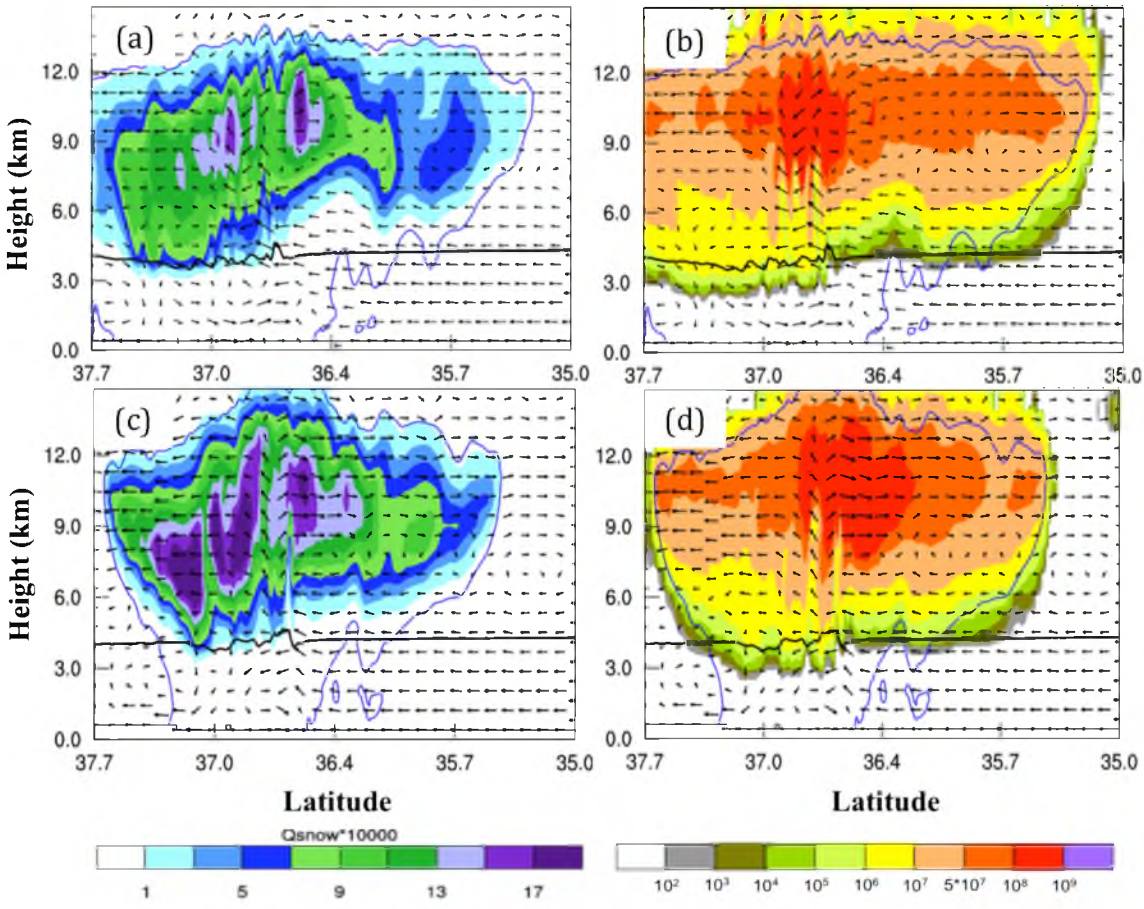

Figure 3.7. Cross-sections of snow mixing ratio (a, c) and intercept parameter N_{0s} (b, d) for H-MORR (a, b) and WRF-MORR (c, d) at 2300 UTC 23 May 2011.

CHAPTER 4

COMPARISON BETWEEN SIMULATION AND UND-CITATION DATA

The evaluations in the previous chapter were done with conventional observations, namely, NEXRAD radar reflectivity, MESONET, and NCEP-Stage IV precipitation data. Results suggest that simulations with the fully 2M scheme (WRF-MORR and WRF-Hail) produce good results with the proper convection lifecycle, precipitation, and cloud components. Because microphysical schemes are the parameterization that deals with the formation and dissipation of raindrops and ice crystals, the direct measurements of hydrometeor properties are very important for their evaluation. Fortunately, the MC3E field campaign leveraged the unprecedented observing infrastructure currently available in the South Great Plains, combined with an extensive sounding array, remote sensing, and in-situ aircraft observations (Jensen et al. 2010). Among these available data, the University of North Dakota Citation (UND-Citation) dataset is one of the most valuable, as it provides hydrometeor distribution with directly measured hydrometeor properties, such as ice mixing ratio, ice water content, and ice particle number concentration in each specific diameter bin. In order to evaluate the performance of microphysical schemes in predicting microphysical properties, we compare the model simulations with the UND-Citation dataset.

4.1 Introduction to Aircraft Data

The UND owns and operates a Cessna Citation jet aircraft for the purpose of atmospheric research. This aircraft is capable of sampling atmospheric state parameters, winds, and turbulence, as well as cloud microphysics. The aircraft operates at altitudes ranging from near-surface to 13 km, and it is certified for its ability to fly into icing conditions (Delene 2010). Measurements from the UND-Citation have been used in many scientific publications (e.g., Prenni et al. 2007; Sukovich et al. 2009).

For the selected convection case in this study (May 23-24), UND-Citation cloud microphysics data are available from 2100 UTC 23 May 2011 to 0030 UTC 24 May 2011 at 1-second intervals, which covers the developing and mature stages of the convection system. The data quality is good for this time period. Considering the variability and coverage of the convection system and UND-Citation dataset, data between 2145 UTC 23 May 2011 and 0015 UTC 24 May 2011 are used for the following evaluations. The aircraft flies at a height of between 7 and 9 km during this period. Figure 4.1 illustrates the three-dimensional (3D) aircraft track of during the period. Figure 4.2 shows the aircraft track height, along with the cross-section of the NEXRAD radar reflectivity. It is clear that the UND-Citation aircraft travels mainly in the stratiform region of the convection system.

The aircraft measures the mixing ratio, ice water content, and number concentration using different instruments. Specifically, the number concentration (in each size bin) is measured by the PMS (particle measuring system) 2DC (33 to above 1000 μm), CPI (cloud particle imager), and HVPS (high volume particle spectrometer) imaging probe, with ice particles size ranging from 200μm to about 6cm. The 2DC and

HVPS probes sample the size of ice particles about 0.007 and $1m^{-3}s^{-1}$, respectively (Heymsfield et al. 2004). The measurements contain records of flight time (UT seconds from midnight) and aircraft latitude, longitude, and altitude. The mixing ratio is measured by the laser hygrometer. The ice water content (IWC) data come from two sources: one is the CPI, with a resolution of about 2 μm and a minimum detectable size of about 20 μm, which provides detailed information on ice particle sizes ranging from 50 to 500 or 600 μm (Heymsfield et al. 2004), or the 2DC and HVPS number concentration dataset. The other data come from the Nevzorov probe, which provides a measurement of TWC (total water content) and LWC (liquid water content), which are fully calculated from first principles of heat transfer on the sensor wire (Korolev et al. 1998; Vidaurre et al. 2011). For the first IWC data source, the IWC is calculated by equation (4.1).

$$IWC = \sum_{D_{\min}}^{D_{\max}} N(D)M(D) \tag{4.1}$$

where D_{min} is the minimum diameter of the particles, D_{max} is the maximum diameter of the particles, N(D) is the number of particles in the specific diameter bin, and M(D) is the corresponding mass of the particle, calculated by: M(D)=0.0061*(D^2.05) (Heymsfied et al. 2004). For the second data source, the Nevzorov probe does not measure IWC directly. Instead, it measures the TWC and LWC. The IWC is the difference between the TWC and LWC.

4.2 Method of Comparison

Figure 4.3 illustrates the time series of the altitude of the aircraft track along the model vertical levels. The aircraft track is located mostly between 7 km and 9 km in height, ranging from the 29th to 32nd model levels. It is apparent that the space between the model levels is sparse (>1 km). Since the microphysical variables vary vertically and the variations are not a specific function of height, their interpolation among those these model levels will introduce additional uncertainties. In order to make the comparison more reliable, we compare the UND-Citation data with the model values at the nearest model vertical level.

We first check the aircraft track to get a basic understanding of the observation positions relative to the characteristics of the convective system. Figure 4.4 shows a series of composite radar reflectivity from both the observations (NEXRAD) and WRF simulations, with the locations of the aircraft. As Figure 4.2 also shows, the aircraft does not fly around the convective core region. It flies in the area where most of the composite radar reflectivity ranges from 20 to 30 dBZ. Meanwhile, compared with the NEXRAD observations, the simulations of the convection system have both position and coverage errors. Specifically, the convective systems produced by the WRF-WSM6 (second column in Figure 4.4) and WRF-WDM6 (third column in Figure 4.4) schemes completely missed the aircraft track. The convection produced by WRF-MORR (right column in Figure 4.4) covers the aircraft track successfully. However, WRF-MORR produces a large positive dBZ bias along the aircraft track. In addition, the three simulations also produce different convection vertical structures. The vertical structures of the radar reflectivity from NEXRAD observations and WRF simulations are examined in Figure

4.5. The two parallel black lines represent the height range within which the aircraft flies. The simulations with the WSM6 (Fig. 4.5b) and WDM6 (Fig. 4.5c) schemes underestimate the echo top (as was discussed in detail in Chapter 2), while WRF-MORR (Fig. 4.5d) overestimates the dBZ value. Owing to the location and structure errors, it is difficult to directly compare the UND-Citation observations with the simulations. A method of comparison is designed based on the following concerns: The convection systems can be classified into different components based on the 3D distribution of radar reflectivity (the algorithm was described in Chapter 2). These convection components differ considerably both dynamically and thermodynamically (Feng et al. 2011; Wu et al. 2013). Although model simulations have position errors, the convective components are statistically comparable with the observations. Therefore, we should be able to compare the UND-Citation data with the average value over each specific convection component that the aircraft flew over. The details of the comparison procedures are described as the following:

Step 1: Classify the convection system into different components (such as convection core, stratiform rain region, transitional anvil region, and anvil region) for both the NEXRAD observations and the WRF simulations based on the 3D radar reflectivity distribution.

Step 2: Average the microphysical properties (such as ice mixing ratio, ice water content, and ice particle number concentration) produced by the simulation over space for different cloud components.

Step 3: Average the UND-Citation data over 5 min time intervals in order to: (1) be able to obtain enough samples to calculate the average, and (2) accommodate the 5 min data intervals in the WRF simulations.

Step 4: Compare the area-averaged values of the WRF simulations for each convection component with the temporal average values of the UND-Citation data.

The convection components derived from both the NEXRAD observations and the WRF simulations as well as the corresponding location of the aircraft tracks are shown in Figure 4.7. Most of the aircraft positions are located in the stratiform rain and transitional anvil regions. The simulations with the WSM6 and WDM6 schemes produce less coverage of the stratiform and transitional anvil regions, introducing some uncertainties in the comparison. The simulation with the MORR scheme produces proper coverage of the stratiform rain and transitional anvil regions. Figure 4.8 illustrates the time series of the number of grid points in the area of each convection component. WRF-MORR (Fig. 4.8c) produces a larger number of grid points of stratiform rain and transitional anvil than are produced by WRF-WSM6 (Fig. 4.8a) and WRF-WDM6 (Fig. 4.8b). However, the number of grid points in WRF-WSM6 (Fig. 4.8a) and WRF-WDM6 (Fig. 4.8b) also provides large enough samples to be averaged and compared with the UND-Citation dataset.

4.3 Results

4.3.1 Mixing Ratio

The MP schemes (e.g., WSM6, WDM6, and MORR) separate the ice particles into three categories: cloud ice, snow, and graupel. The aircraft, however, collects the

mixing ratio of the total ice contributed by these three ice categories. Therefore, the sum of the ice mixing ratios of cloud ice, snow, and graupel from simulations are compared with the UND-Citation data. Figure 4.9 compares the time series of the area-averaged ice mixing ratio over different convection components (Fig. 4.9a over the CC region; b over the SR region; c over the transitional anvil region; and d over the anvil region) and the 5 min averaged mixing ratio measured by the laser hygrometer probe in the UND-Citation aircraft. The simulations reproduce a clear decreasing trend in the ice mixing ratio from the CC region to the anvil region, implying that the convection component classification algorithm captures the microphysical characters of the convection system. WRF-MORR (multiple signs) produces larger ice mixing ratios than either WRF-WSM6 (plus signs) or WRF-WDM6 (star signs) over all the convection components, especially the convection core (Fig. 4.9a) and stratiform rain regions (Fig. 4.9b). The simulations predict a larger mixing ratio in the CC region compared with the observations. This is reasonable because the aircraft flies mostly around the stratiform and transitional anvil regions. In the SR region (Fig. 4.9b), the ice mixing ratios produced by WRF-WSM6 and WRF-WDM6 agree very well with the observations. The WRF-MORR significantly overestimates the mixing ratio, possibly because of the large amount of graupel available in this region.

For the ACtrans region (Fig. 4.9c), WRF-WSM6 and WRF-WDM6 produce a proper mixing ratio compared with the aircraft data, especially WRF-WSM6. WRF-MORR overestimates the mixing ratio. Overall, 1M representations of ice hydrometeors (WSM6 and WDM6) perform better than 2M representations of ice (WRF-MORR). The overestimation of the mixing ratio in WRF-MORR can be attributed to the large amount of graupel.

In order to eliminate the uncertainties due to averaging over area (simulations) and time (UND-Citation), the ice mixing ratio spatial (simulations) and temporal (UND-Citation) probability distributions with percentiles of 75% and 25% in specific convection components are shown in Figure 4.10. The figures confirm that WRF-WSM6 and WRF-WDM6 produce a reasonable ice mixing ratio in the SR (Fig. 4.10d and e) and ACtrans region (Fig. 4.10g and h), while WRF-MORR overestimates the mixing ratio in stratiform rain and transitional anvil regions (Fig. 4.10f and i).

4.3.2 Ice Water Content (IWC)

The IWC data used in the aircraft dataset are not direct measurements. Instead, they are derived from other variables (as discussed in Section 4.1). Similarly, the model simulations do not produce the IWC values directly. These can be calculated from the model variables using equation (4.2).

$$IWC = \rho q \tag{4.2}$$

where ρ is the air density, calculated using the ideal gas law, and q is the ice mixing ratio.

Because the IWC in the UND-Citation data set is derived from the large particles only (diameters larger than 100μm), in order to be consistent with the UND-Citation data, only the IWC values of snow and graupel in model simulations are counted to compare with aircraft observations.

Figure 4.11 compares the averaged IWC over different convection components between simulations and aircraft observations (averaged over time). Relatively large

variability is found in the time series of the IWC. Similar to the mixing ratio, the IWC also shows a decreasing trend from the CC (Fig. 4.11a) to the anvil region (Fig. 4.11d). WRF-MORR produces a larger IWC than WRF-WSM6 and WRF-WDM6. For the stratiform rain region (Fig. 4.11b), WRF-MORR produces a realistic IWC. WRF-WSM6 and WRF-WDM6 underestimate the IWC. The IWC values derived from the simulations in the ACtrans (Fig. 4.11c) and AC (Fig. 4.11d) regions are very smooth and are smaller than the observations, which may be caused by the small amount of graupel in the ACtrans region, because graupel dominates the ice water content.

The spatial probability distributions with the percentiles of 75% and 25% of IWC for different convection components are shown in Fig. 4.12. Large discrepancies are found between observations and simulations in the stratiform rain region (Figure 4.12d, e, and f) and transitional anvil region (Figure 4.12g, h, and i). WRF-WSM6 (Fig. 4.12d) and WRF-WDM6 (Fig. 4.12e) underestimate IWC, while WRF-MORR (Fig. 4.12f) produces a realistic IWC. Similar conclusions are found for the IWC in the ACtrans region. It is apparent that the comparison of ice water content leads to a different conclusion from what we obtained using the ice mixing ratio. This is perhaps partly due to the different methods used in this study for deriving IWC for the observations and simulations.

As stated in Section 4.1, there are two data sources for the IWC. One is the 2DC and HVPS probes; the other is the Nevzorov probe. Figure 4.13 compares these two data sources. It is clear that the 2DC and HVPS3 produce a higher IWC than the Nezvorov probe. Note that the previous IWC comparisons were done with the values derived from the 2DC and HVPS probes. If the simulations are compared with the data collected from the Nevzorov probe, WRF-WSM6 and WRF-WDM6 match the observations better than

WRF-MORR. The difference, arising from the two IWC datasets, illustrates the significant influence of the observation errors, which should be considered in the comparison.

4.3.3 Number Concentration

The number concentration collected by the UND-Citation aircraft is measured by the 2DC and HVPS3 probes. These probes collect the number concentration of the particles with diameters larger than 100μm. In the model simulations, considering the size of ice phase hydrometeors, only the number concentration of snow and graupel are considered. Among the three MP schemes used in this study, the MORR scheme treats the snow and graupel hydrometeors as 2M species, as WRF-MORR predicts the mixing ratio and number concentration of graupel and snow. However, the WSM6 and WDM6 schemes treat snow and graupel as 1M species. The number concentration is diagnosed from the mixing ratio and other parameters. The particle size distribution of snow and graupel used in WSM6 and WDM6 are treated as a gamma function:

$$N(D) = N_0 D^{\mu} e^{-\lambda D} \tag{4.3}$$

where N_0 is the intercept parameter, μ is the shape parameter, which is always set to 0 for snow and graupel, and λ is the slope, which can be derived from the equation (4.4).

$$\lambda = \left[\frac{\pi \rho_i N_0 \Gamma(\mu + 4)}{6 q_i} \right]^{\frac{1}{\mu+4}} \tag{4.4}$$

where Γ is the Euler gamma function.

The number concentration for the specific diameter range is calculated by the integral of the particle size distribution:

$$N_{D=100\,\mu M}^{D=\infty} \int_{D=100\,\mu m}^{D=\infty} N_0 e^{-\lambda D} = -\frac{D}{\lambda} e^{-\lambda D} \Big|_{D=100\,\mu m}^{D=\infty} \tag{4.5}$$

To compare the number concentrations between the model simulations and observations, the spatial/temporal probability distributions with the percentiles of 75% and 25% of the number concentration of the model simulations, and the observations, are shown in Figure 4.14. The UND-Citation shows a very large variability in number concentration, but the average values from the simulations show a steady trend. The model simulations sometimes significantly underestimate the number concentration. The simulated number concentration does not capture the observed large frequency variability in the ice particle number concentration.

4.4 Comparison Summary

In this chapter, the WRF-simulated microphysical properties of the ice mixing ratio, ice water content, and total ice particle number concentration are validated using the UND-Citation aircraft observations in the developing and mature stages of the convective system. Preprocessing of both the simulations (spatial averaging) and observations (temporal averaging) has been done in order to make a consistent comparison. The results suggest that 2M representations of ice hydrometeors (WRF-

MORR) do not improve the prediction of the ice mixing ratios. However, they improve the simulation of the IWC prediction, although there are clear differences in the two types of IWC datasets, with the IWC measured by the Nevzorov probe being clearly smaller than the value derived from the 2DC and HVPS dataset. The total ice number concentrations produced by the model are clearly different from the observations.

Overall, results suggest that 2M representations of ice phase hydrometeors (WRF-MORR) do not outperform the 1M schemes in terms of the prediction of microphysical variables. The reasons may be, but are not limited to, the following:

1. The simulations produce different convection structures compared with NEXRAD observations. As stated in Section 4.2, WRF-WSM6 and WRF-WDM6 underestimate the echo top. WRF-WSM6 also underestimates the radar reflectivity around the 8-10 km height range (aircraft track) in the stratiform and anvil regions. MORR overestimates the radar reflectivity around the 8-10 km heights (aircraft track). These dBZ biases have a significant influence on the comparison, because dBZ is a reflection of the hydrometeors.
2. The errors in the aircraft dataset also play an important role. As shown in Figure 4.13, large discrepancies are found in the different measurements of the IWC.
3. The aircraft data are too sparse to compare with the model, as the aircraft sampled only one point at each specific time. More spatial distribution data are needed, such as those from lidar and satellite datasets, etc.

Regardless of the position error of the simulated convective system, results from this chapter suggest that WRF-WSM6 and WRF-WDM6 produce a better result than WRF-MORR. This conclusion is the opposite of that of the previous chapter, where

traditional evaluation methods (such as precipitation, convection structure, etc.) proved that 2M improved the prediction of the MCS. These two opposite conclusions indicate that coordination between microphysical properties (mixing ratio, IWC, number concentration, etc.) and the dynamic field (which controls the echo top) might be important.

The question now arises: What are fair criteria for evaluating MP schemes? Would it be better to use convection structure, precipitation, and dynamic feedback of the convection system, or to use hydrometeor properties? It seems that among the current three schemes, none of them can outperform the others in every criterion. The opposite conclusions from the evaluations in Chapter 2 and this chapter suggest that the uncertainties in the microphysics schemes could still be a productive area of future research.

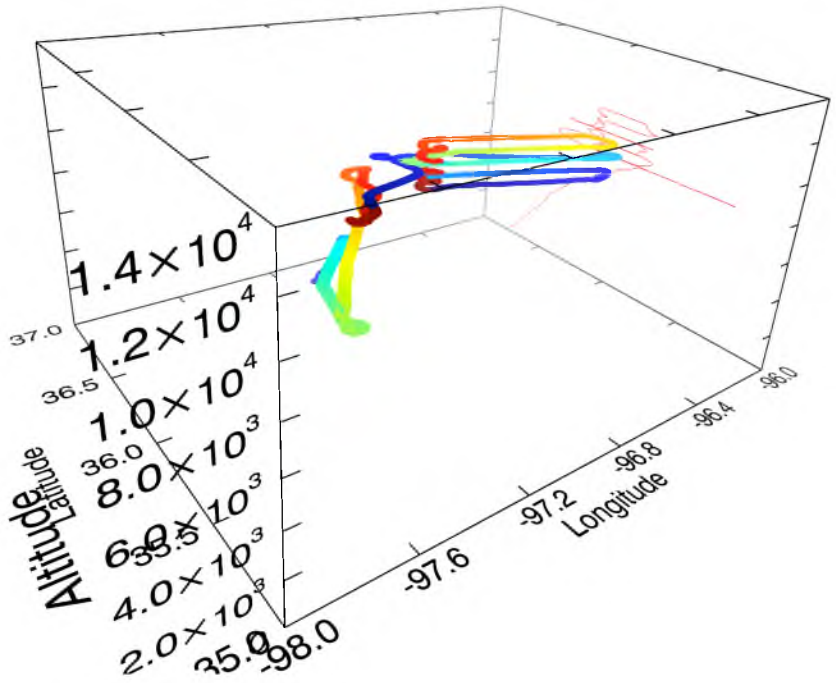

Figure 4.1. Three-dimensional UND-Citation aircraft track from 2100 UTC 23 May 2011 to 0030 UTC 24 May 2011.

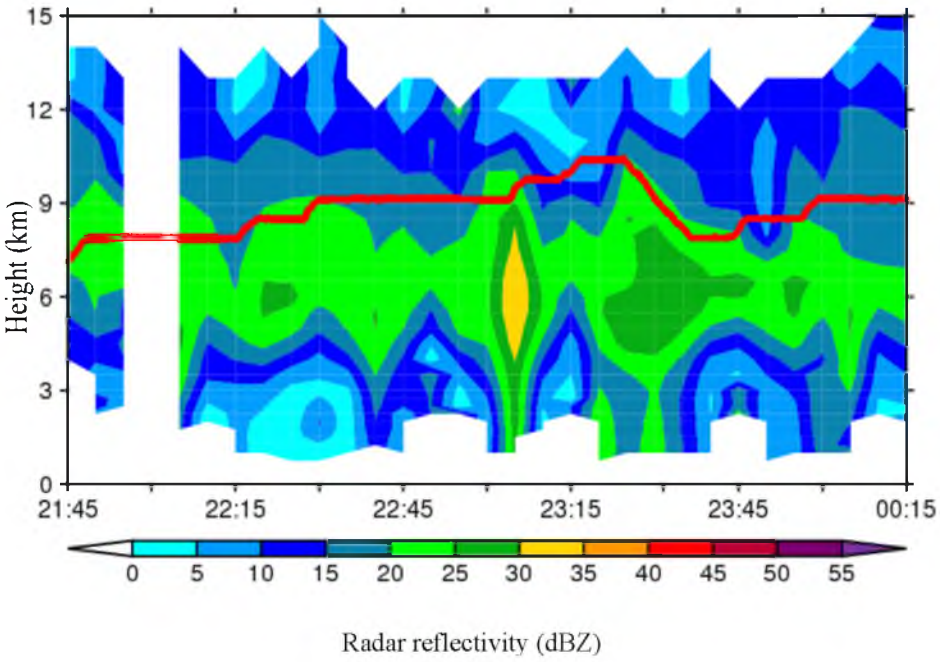

Figure 4.2. The aircraft track (red line) and the vertical structure of radar reflectivity observed by NEXRD networks.

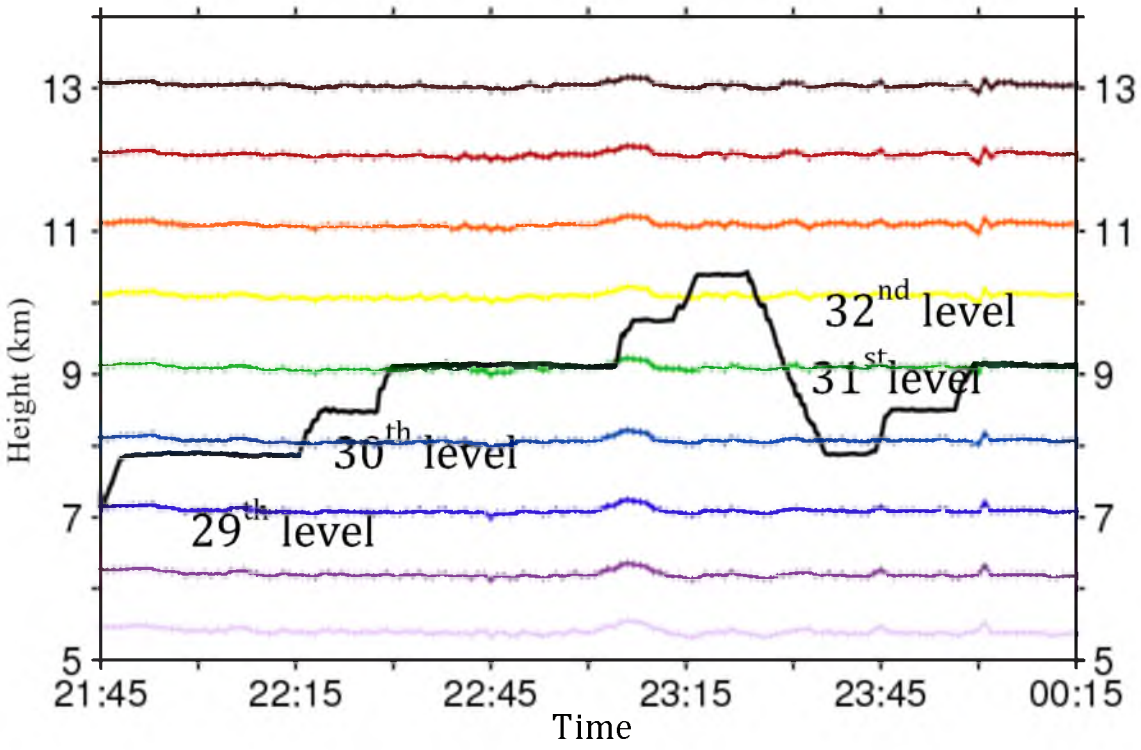

Figure 4.3. Aircraft track (thick black line) along the height and the model vertical levels.

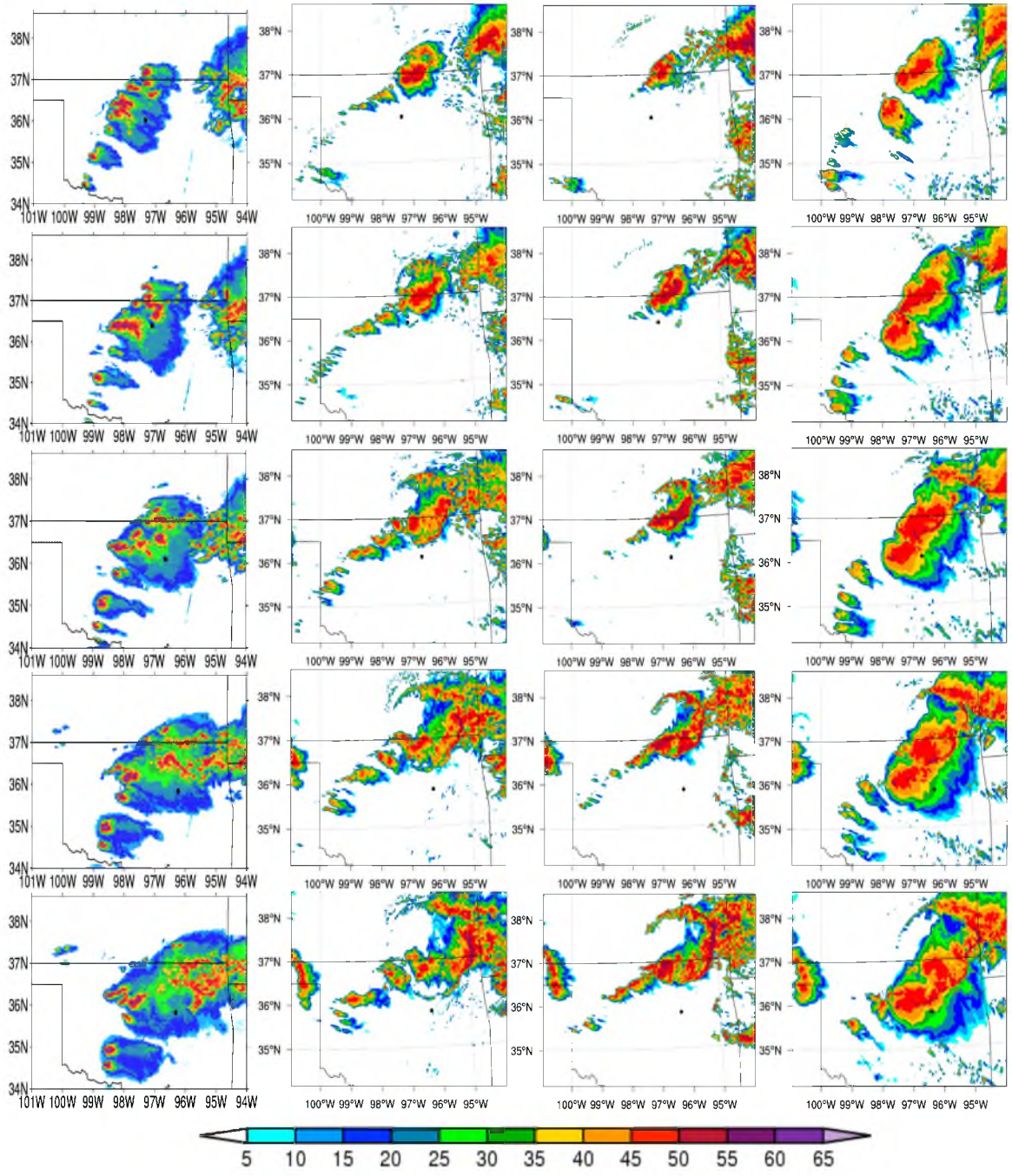

Figure 4.4. The aircraft locations (black dot) at the specific times and the corresponding composite radar reflectivity from NEXRAD observations (left panels), WRF-WSM6 (second column panels), WRF-WDM6 (third column panels), and WRF-MORR (right panels). From upper to bottom are the time from 214500 23 UTC May 2011 to 234500 23 UTC May 2011 in 30 min interval.

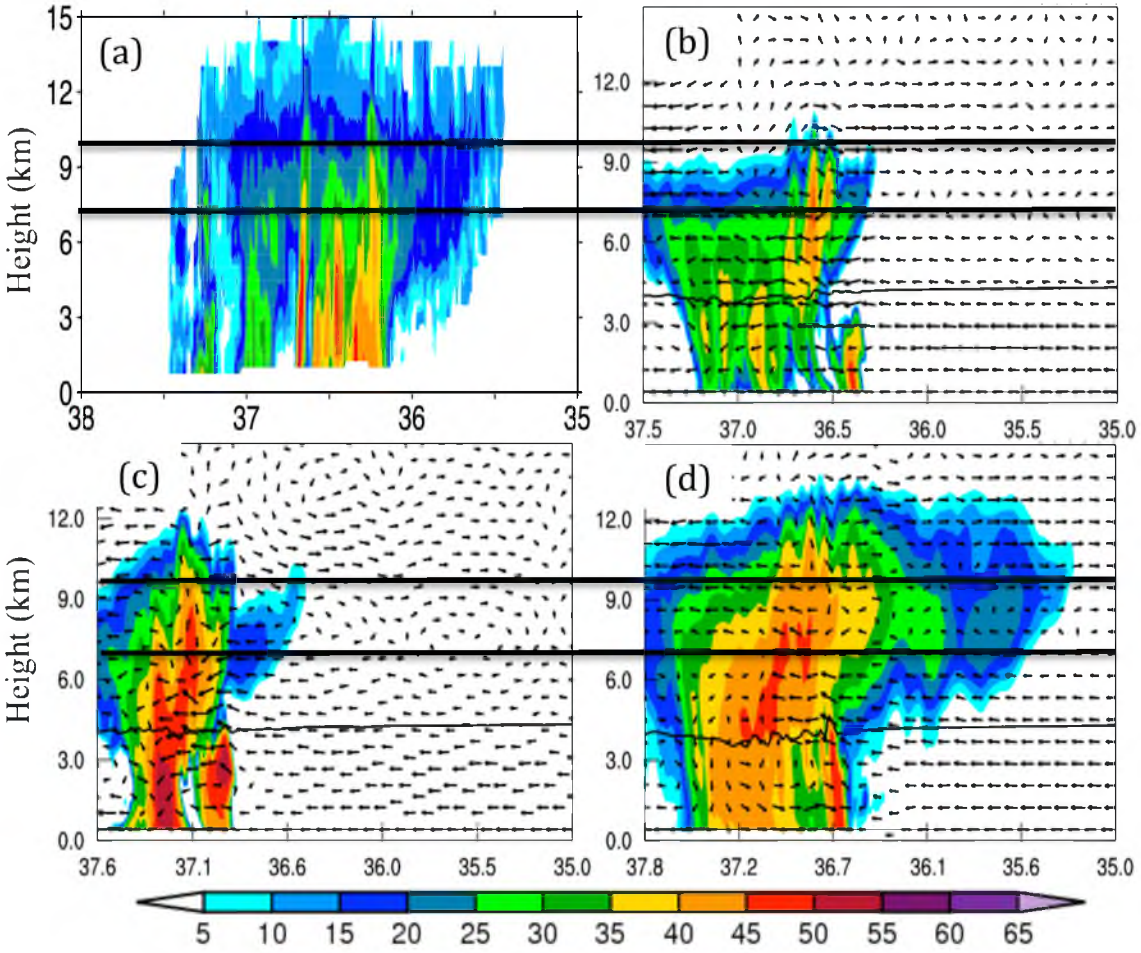

Figure 4.5. North-South vertical cross-section of radar reflectivity at 2300 UTC 23 May 2011 from (a) NEXRAD-observations, (b) WRF-WSM6, (c) WRF-WDM6, and (d) WRF-MORR. The two black line zooms in the height range of the aircraft track locates.

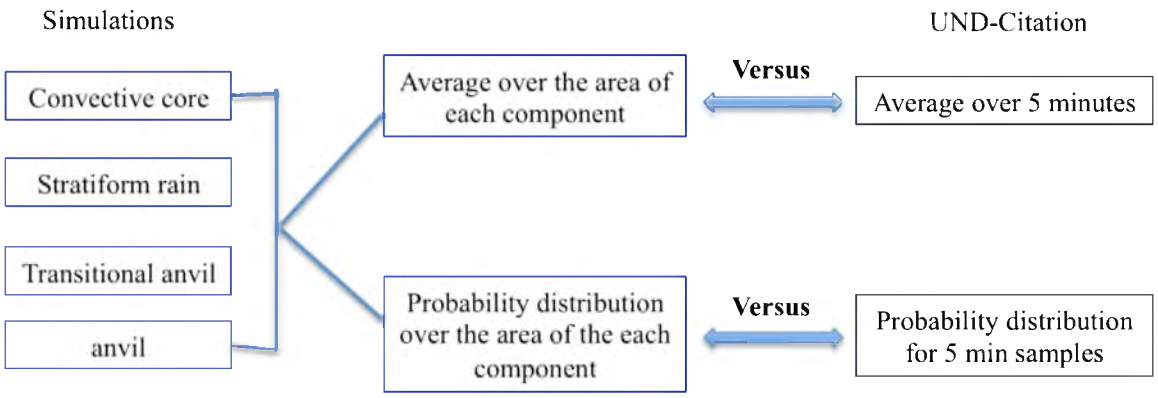

Figure 4.6. Flow chart of the comparison method.

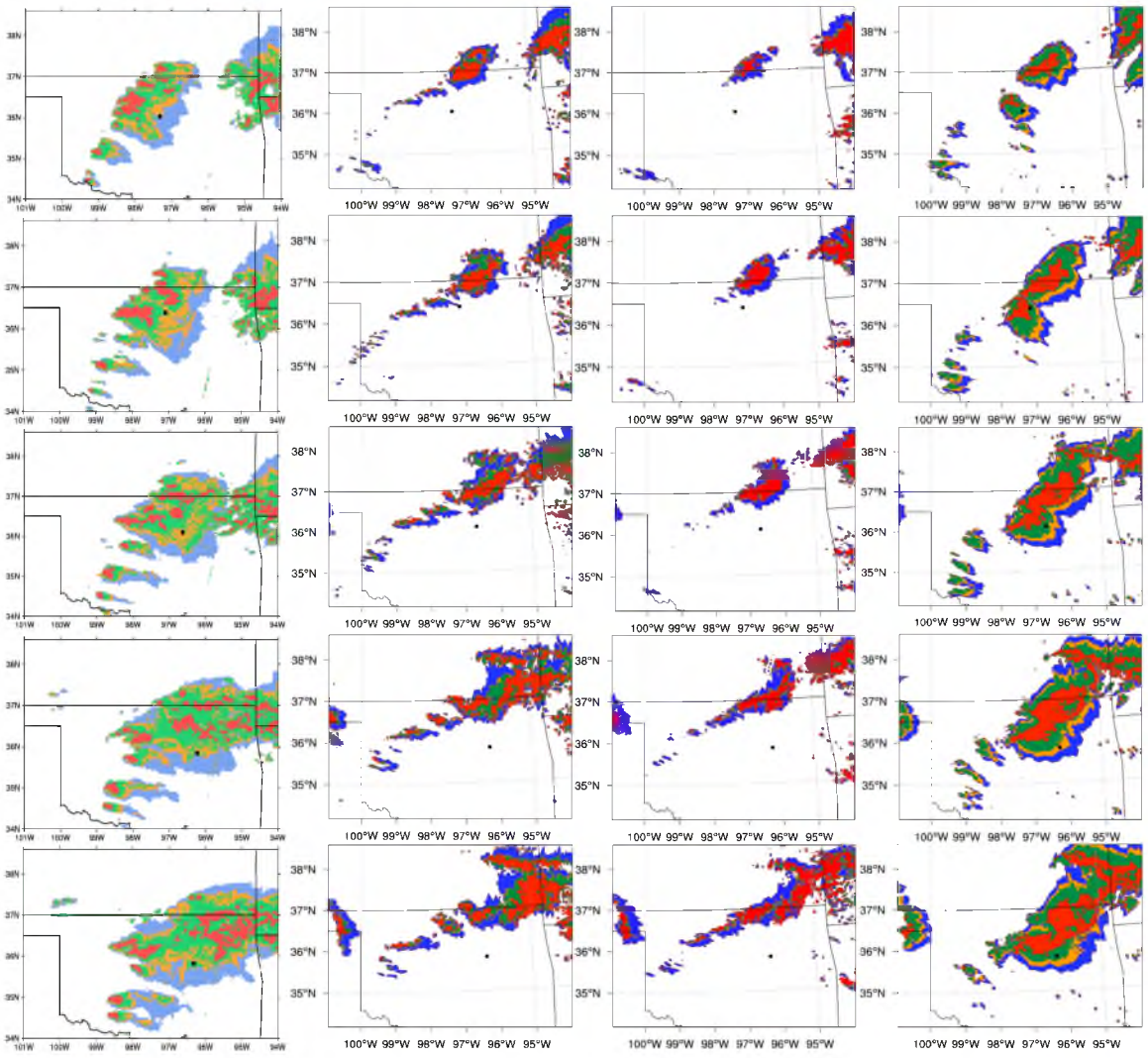

Figure 4.7. Same as Figure 4.4 but the different convection components.

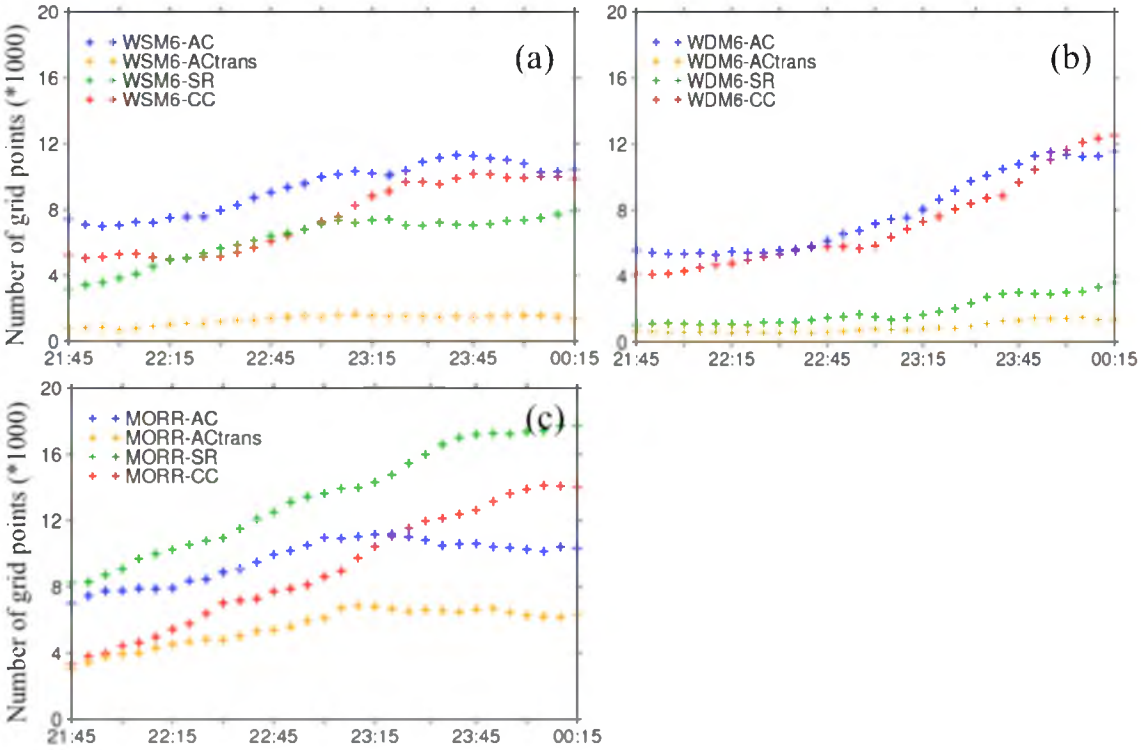

Figure 4.8. Time series of the numbers of grid points in the areas of the different convection components (red dots: CC; green dots: SR; orange dots: ACtrans; blue dots: AC) from (a): WRF-WSM6; (b): WRF-WDM6; and (c): WRF-MORR).

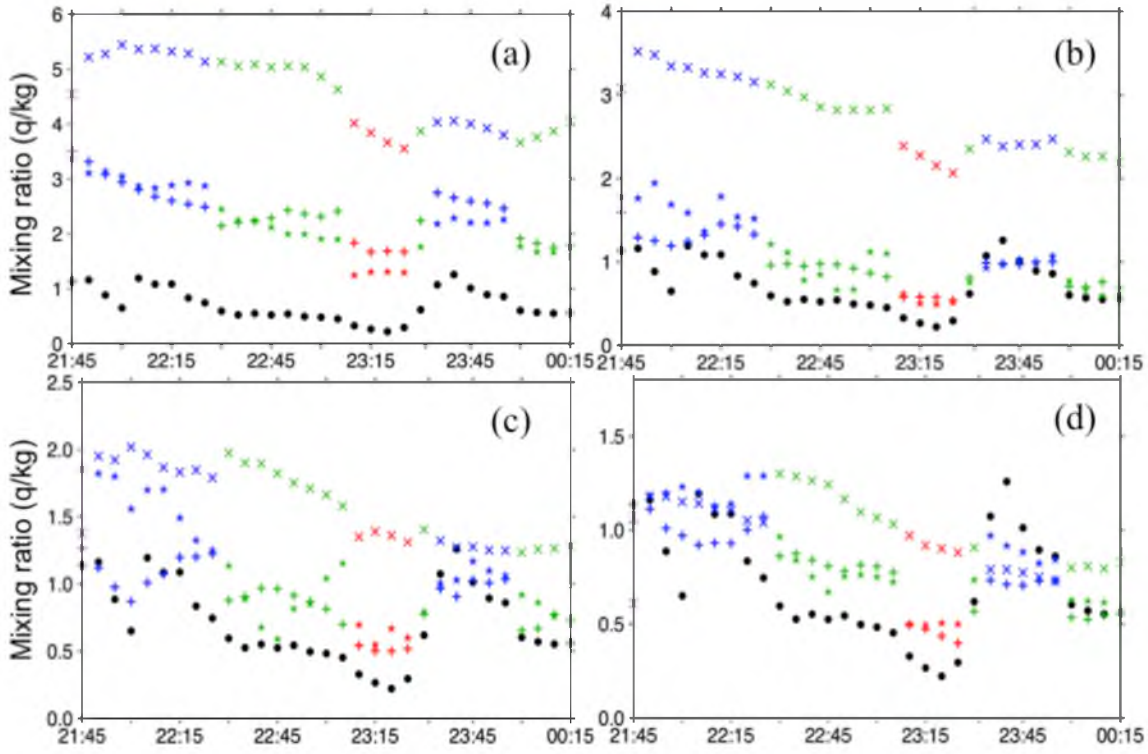

Figure 4.9. Time series of the time averaged mean ice mixing ratio of observation (black dots) and spatial averaged (a: over CC region; b: over SR region; c: over ACtrans region; and d: over AC region) ice mixing ratio of simulations. The different signs indicate the different simulations, plus sign: WRF-WSM6; star sign: WRF-WSM6; multiple sign: WRF-MORR) and the different colors of dots represent the nearest model level, purple: 29th level; blue: 30th; green: 31st level; and red: 32nd level.

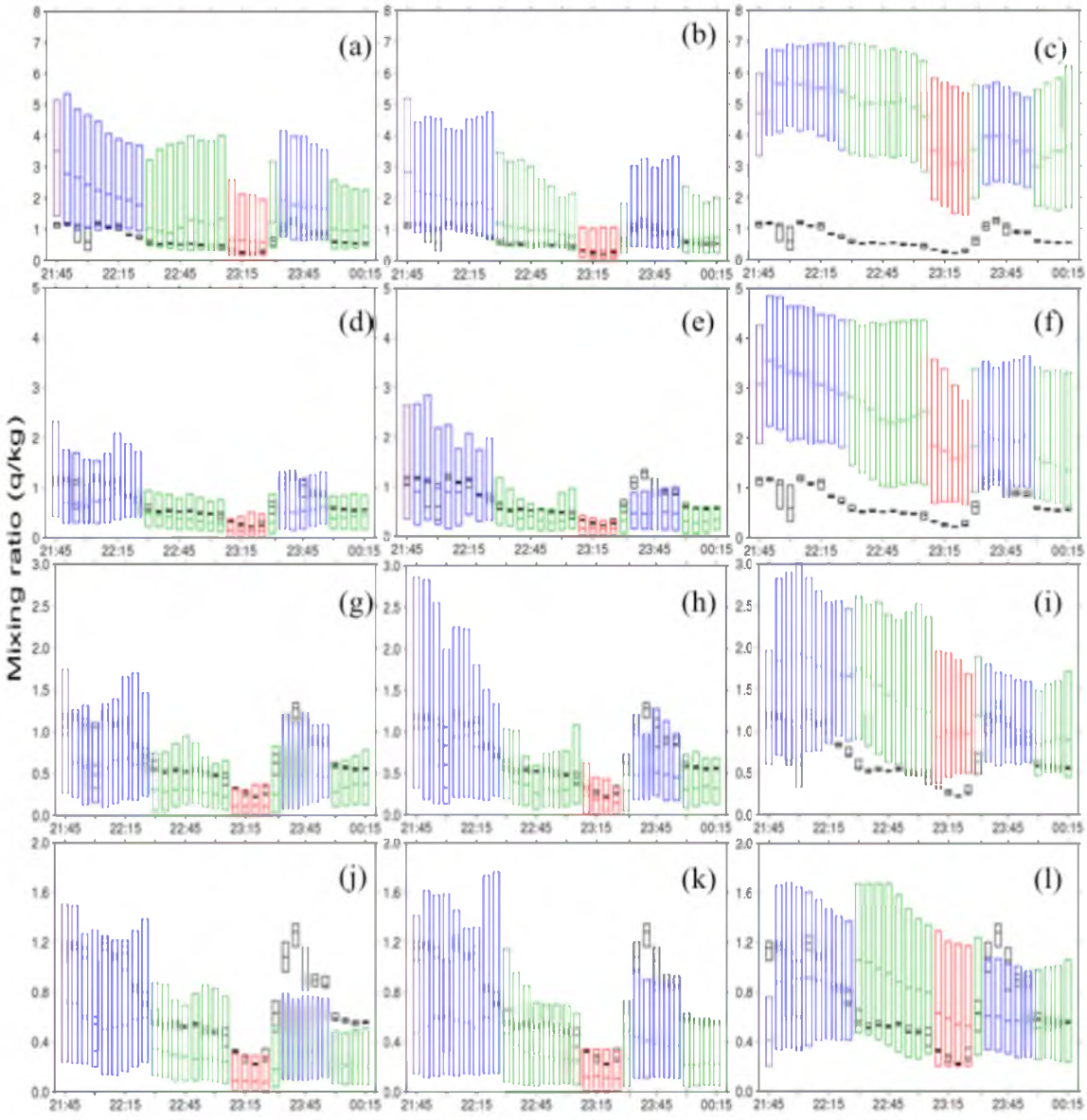

Figure 4.10. The probability distribution with the percentiles of 75% (upper limit), 50% (median), and 25% (bottom limit) for the ice mixing ratio from observation (black) and simulations (left panels: WRF-WSM6; middle panels: WRF-WDM6; and right panels: WRF-MORR). The distribution is countered over space for simulations but over time for the observation. From upper to bottom is the value averaged over different convection components (CC: (a)-(c), SR: (d)-(f), ACtrans: (g)-(i), and AC: (j)-(l)) for simulation.

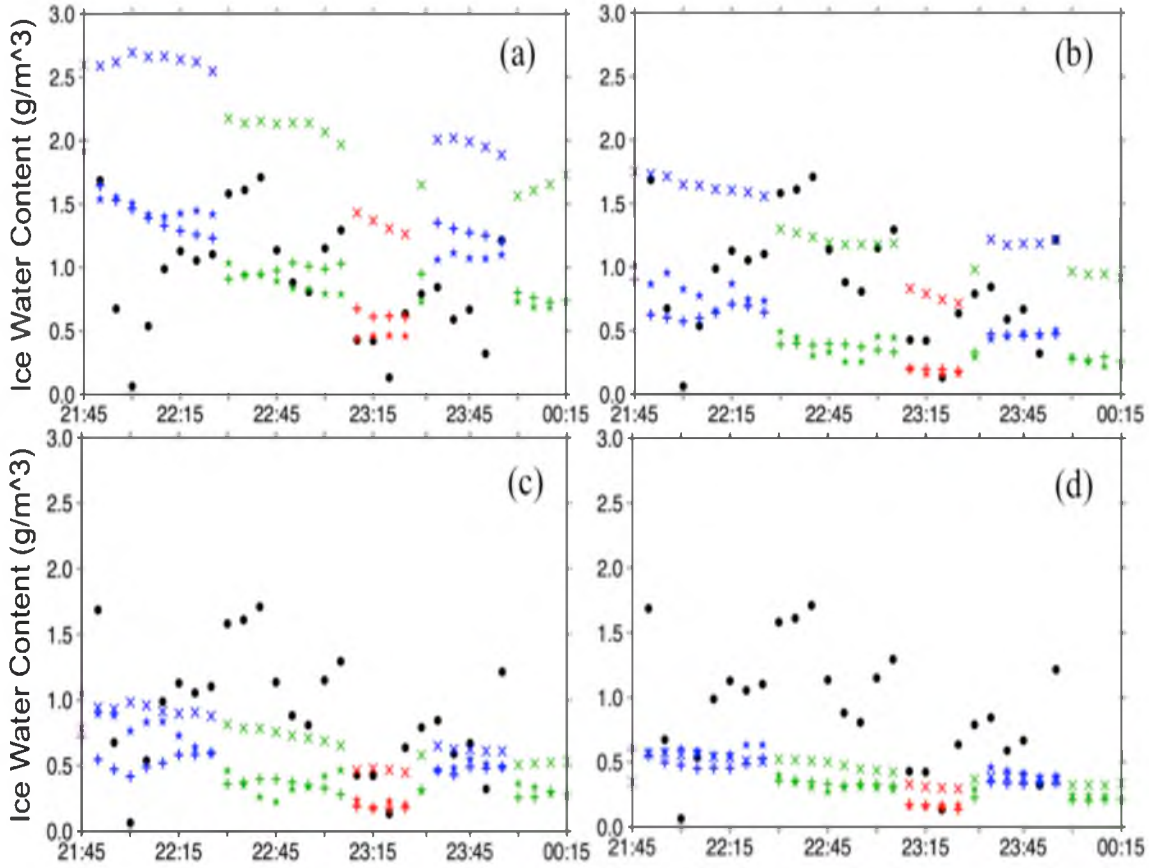

Figure 4.11. Same as Figure 4.9 except the ice water content.

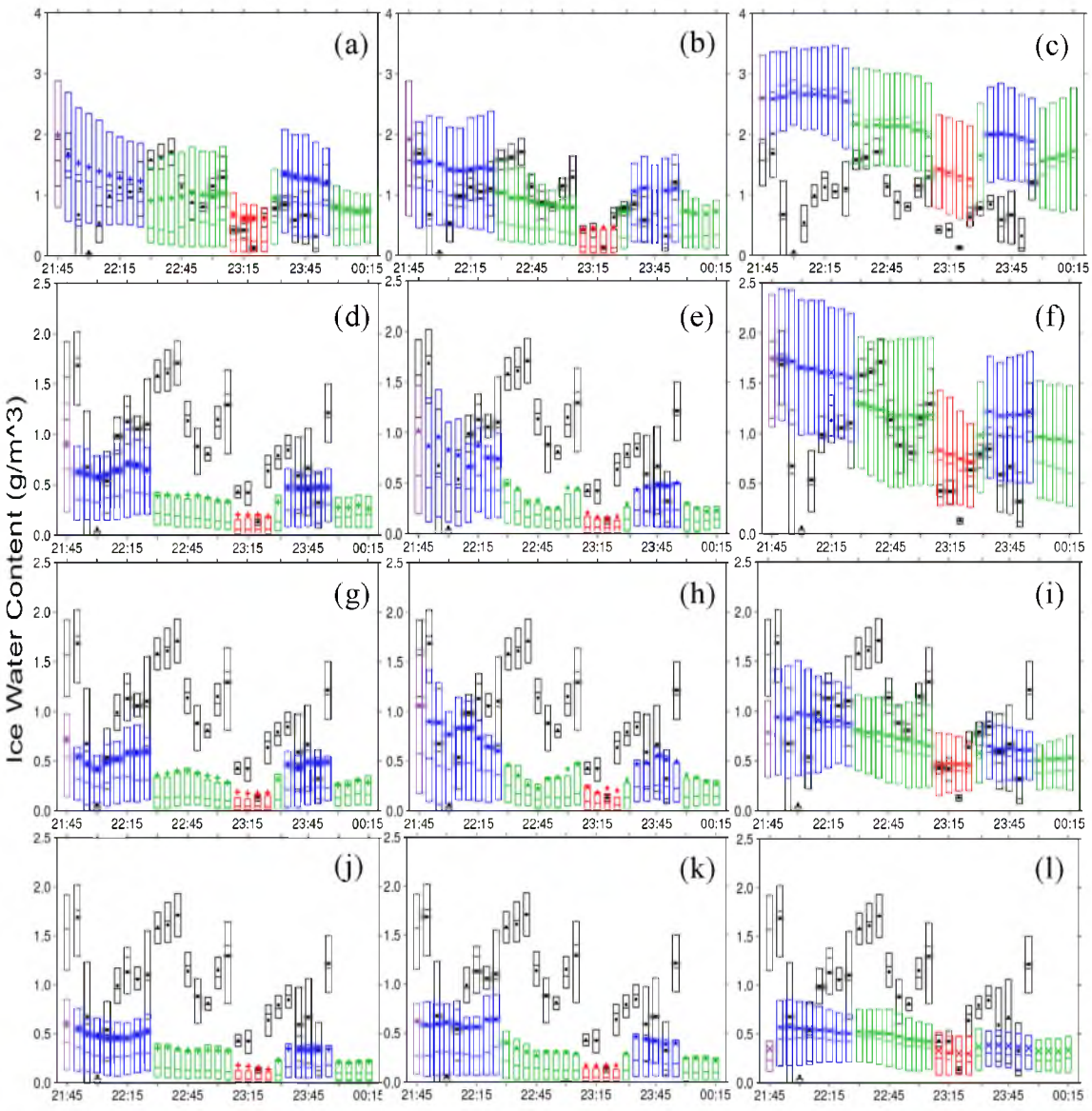

Figure 4.12. Same as Figure 4.10 except the ice water content, and the black dot represents the time-averaged value of observation, multiple sign represents the space-averaged value of different simulations.

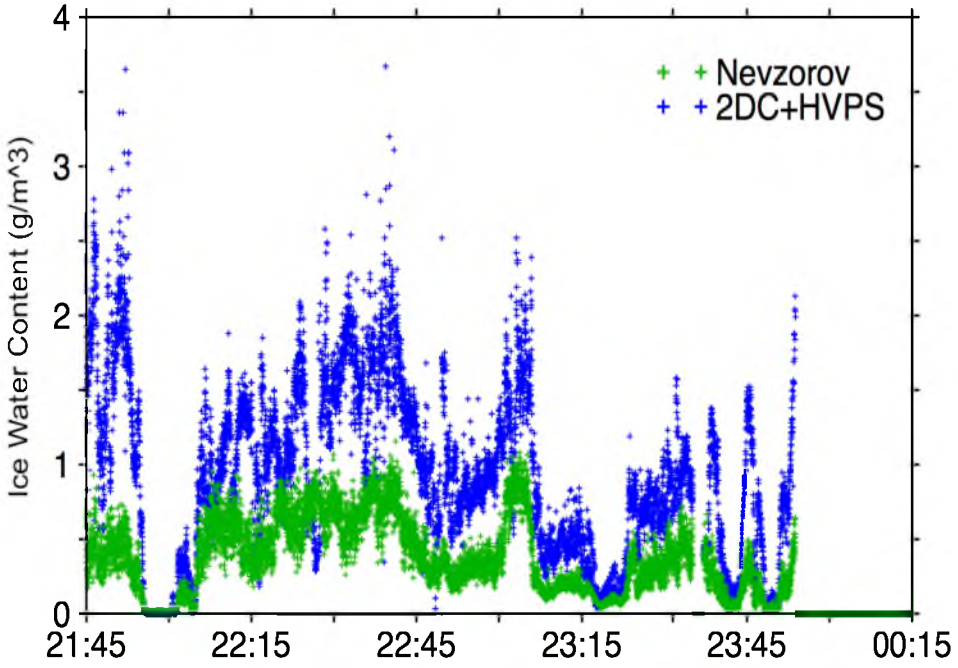

Figure 4.13. Time series of ice water content observed by 2DC and HVPS probes: blue dots and from Nevzorov probe: green dots. The time interval is one second for both datasets.

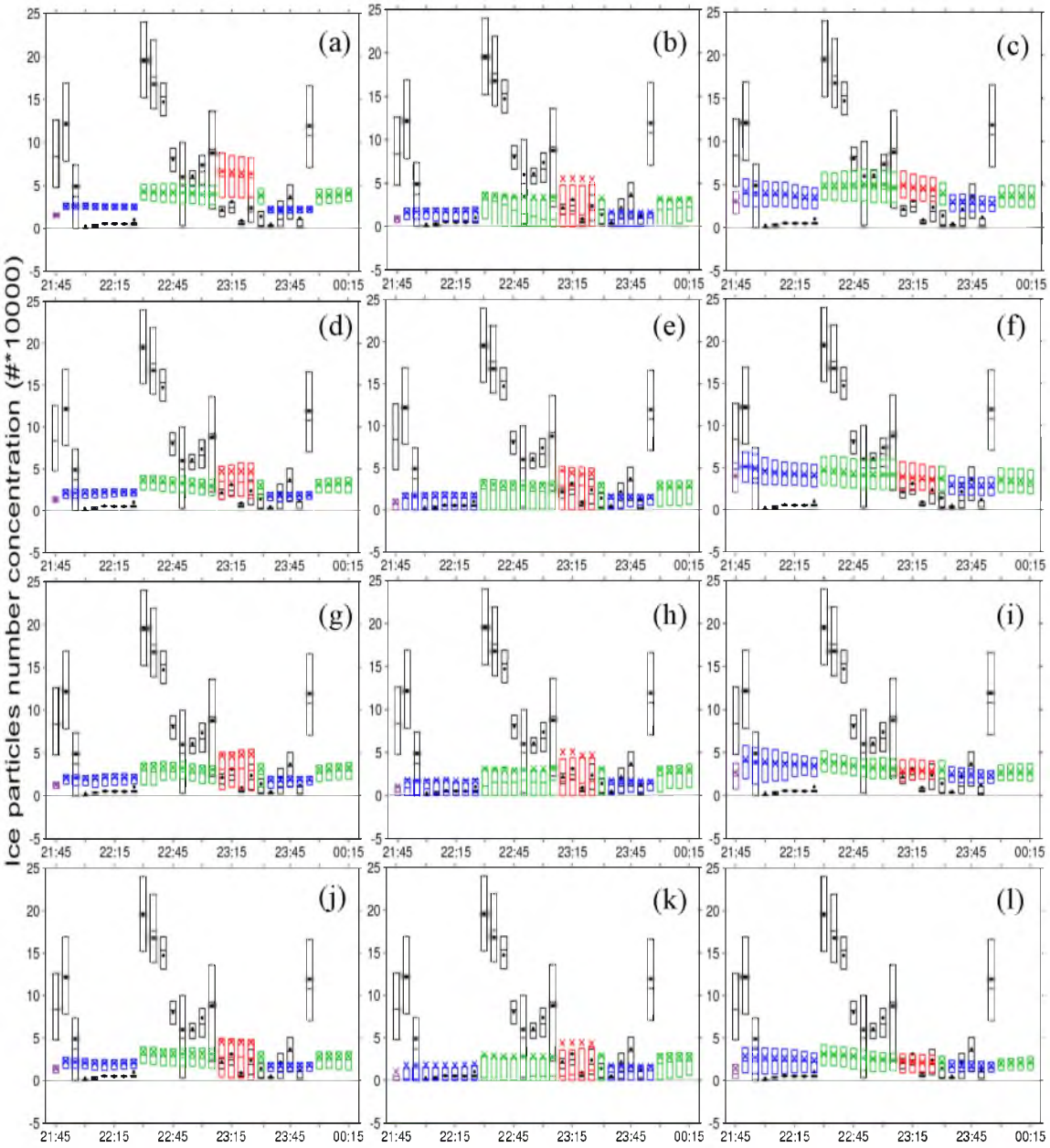

Figure 4.14. Same as Figure 4.10 but for the number concentration of the ice phase particles with diameters larger than 100μm.

CHAPTER 5

SUMMARY AND CONCLUDING REMARKS

In this study, a mesoscale convective case (23-24 May 2011) during MC3E is studied over the Oklahoma region using the WRF model. Three different microphysical schemes including 1M, partial 2M, and full 2M representations of warm-rain and ice hydrometeors are used in the WRF simulations. In addition, the sensitivity of simulated MCS properties to precipitating particle parameters in WSM6 and WDM6 as well as the choice of dense ice species (gruapel/hail) in MORR is also discussed. Results are compared with NEXRAD 3-D radar reflectivity observations, the Oklahoma Mesonet data and the NOAA Stage IV rainfall dataset as well as UND-Citation aircraft observations.

The horizontal and vertical structure, lifetime, cloud fractions, and precipitation rate are analyzed. A NEXRAD radar reflectivity-based cloud classification algorithm is also applied for evaluation of the model's ability to predict cloud components, internal structure, and fractions. The differences between single-moment, partial double-moment, and full double-moment microphysical schemes are investigated in order to understand their impacts on the numerical simulations of the MCS.

All of the simulations reproduce the basic properties of this convective event such as its initiation and development. Compared with NEXRAD observations, the simulation

with the 1M microphysical scheme produces the most discrete convection distribution, the shortest convection lifetime, and the lowest echo top. It also heavily underestimates the precipitation intensity, and the cloud component distribution and ratio are also unrealistic.

By adding the 2M representations of warm-rain hydrometeors, WDM6 shows a clear improvement in simulating the convection properties by producing a realistic convection lifecycle and an organized convection structure. Even though the precipitation amount is larger than in WSM6, it still underestimates this amount. The cloud component distribution and ratio are also unrealistic, and the echo top is also lower than that in NEXRAD observations.

The simulation with the full 2M schemes produces much better results than the simulations with 1M and partial 2M schemes; it predicts a realistic convection lifetime, echo tops, and cloud component distribution and ratio, as well as precipitation.

To further diagnose the effects of 2M treatments of warm-rain and ice hydrometeors on numerical simulations of the MCS, hydrometeor profiles and diabatic heating rates as well as the number concentrations are examined. It is found that the simulation with the 1M scheme (WSM6) specifies a relatively large fixed N_0 and a small mixing ratio of rainwater for the entire convection region. The large number of small particles accelerates low-level evaporation, and as a result, part of the rainwater evaporates before it reaches the ground. WSM6 also produces a small amount of graupel due to the relatively small amount of super-cooled water above the melting level. Owing to the lack of enough ice-phase hydrometeor melting, the cold pool is much shallower than in the other two simulations. The combined effect of greater rainwater evaporation,

less rainwater reaching the ground, and a small amount for graupel means that WSM6 lacks a deep and continuous cold pool source to trigger new cells, and thus it produces the shortest convection system lifecycle and the least precipitation.

With the addition of the double-moment representation of warm-rain hydrometeors, the simulation with the partial 2M scheme (WDM6) produces a clear decreasing trend of N_0 of rainwater from the inner to outer regions, and a larger amount of super-cooled water is available in the convective core (CC) region. The large N_0 and high mixing ratio of rainwater cause the high evaporation rate and large amount of rainwater reaching the ground. Super-cooled water supports the production of graupel; as a result, WDM6 produces a larger qg (graupel mixing ratio) than WSM6 in the CC region. As a combined effect, WDM6 produces a larger precipitation amount than WSM6, and the strong and steady cold pool can trigger new convective cells, thus producing a realistic convection lifetime.

The simulation with full 2M schemes (MORR) also shows a decreasing trend from the CC to the outer region for the number concentrations of both rainwater and graupel. The N_{0r} in the CC region is larger than the fixed value used in WSM6, while it is smaller than that value in the stratiform region (SR). The lower part of the cold pool is produced by the evaporation of rainwater. At the same time, the melting and sublimation of ice-phase hydrometeors around the melting level contribute to the depth of the high cold pool. As a result, the combined effects of rainwater evaporation in the CC region and melting/sublimation of ice-phase hydrometeors in the SR produce a strong, deep cold pool and supply continuous forcing to trigger new cells.

Hydrometeor advection from the CC to the outer regions at the middle to upper

levels is important for the maintenance of large SR and AC regions. The advection is governed by the hydrometer amounts and the relative value of the horizontal wind and particle fall speed. The simulation with the full 2M microphysical scheme (MORR) supplies more ice-phase hydrometeors for advection. Therefore, it predicts a larger SR and AC region, which agrees better with the NEXRAD observations.

Two additional sensitivity experiments, in which the precipitating particle parameters in WSM6 and WDM6 were changed to the parameters used in MORR, did not differ much from the simulations with original WSM6 and WDM6 schemes. Results indicate that: besides the difference in moment treatments, differences in other parameters are not responsible for the discrepancies in the WRF simulations with WSM6, WDM6, and MORR.

The influence of the choice of graupel and hail as the type of dense ice species is also examined. The results demonstrate that using hail as dense ice improves the simulations, with better convection structure compared with that using graupel, although it overestimates the precipitation intensity, especially for the CC region. These differences between the two simulations (H-MORR and WRF-MORR) are caused mainly by density and V-D relationship differences between hail and graupel.

The simulated cloud microphysical properties (such as ice water content, ice mixing ratio, etc.) are also compared with the available UND-Citation aircraft observations for the developing and mature stages of the convective system. Pre-processing of both the simulations (spatial averaging) and observations (temporal averaging) has been done in order to make a consistent comparison. Even though the results suffer from observation uncertainties and simulation errors, they suggest that 2M

representations of ice phase hydrometeors (MORR) do not outperform the 1M schemes in terms of predicting microphysical variables. The opposite conclusion for the evaluations with NEXRAD observation and the UND-Citation dataset suggests that coordination between microphysical properties and dynamics fields is important. The uncertainties in the microphysical schemes could be a productive area of future research.

Future work using more cases is needed to further confirm these conclusions. Observations of hydrometeor distribution over large areas are needed for evaluation purposes, and more complicated microphysical schemes (i.e., 4ice) should be developed and evaluated.

REFERENCES

Adams-Selin, R. D., S. C. ven den Heever, and R. H. Johnson, 2013: Impact of graupel parameterization schemes on idealized bow echo simulations. *Mon. Wea. Rev.*, **141**,1241-1262.

Baldwin, M. E., and K. E. Mitchell, 1996: The NCEP hourly multisensory U.S. precipitation analysis. *Preprints, 11th Conf on Numerical Weather Prediction, Norfolk, VA, Amer. Meteor. Soc.*, J95–J96.

Biggerstaff, M. I., and R. A. Houze Jr., 1991: Kinematic and precipitation structure of the 10–11 June 1985 squall line. *Mon. Wea. Rev.*, **119**, 3034–3064.

Brock, F. V., K. C., Crawford, R. L. Elliott, G. W. Cuperus, S. J. Stadler, H. L. Johnson, and M. D. Eilts, 1995: The Oklahoma Mesonet: a technical overview. *J. Atmos.* Sci., **12**, 5-19.

Bryan, G. H. and H. Morrison, 2012: Sensitivity of a simulated squall line to horizontal resolution and parameterization of microphysics. *Mon. Wea. Rev.*, **140**, 202-225.

Bryan, G. H., and M. J. Fritsch, 2000: Moist absolute instability: The sixth static stability state. *Bull. Amer. Meteor. Soc.*, **81**, 1207-1230.

Caniaux, G., J. L. Redelsperger, and J. P. Lafore, 1994: A numerical study of the stratiform region of a fast-moving squall line. Part I: General description and water and heat budgets. *J. Atmos.* Sci., **51**, 2046-2074.

Churchill, D. D., and R. A. Houze Jr., 1984: Development and structure of winter monsoon cloud clusters on 10 December 1978. *J. Atmos. Sci.*, **41**, 933-960.

Cotton, W. R., M. A. Stephens, T. Nehrkorn, and G. J. Tripoli, 1982: The Colorado State University three-dimensional cloud/mesoscale model-1982. Part II: An ice phase parameterization. *J. Rech. Atmos,* **16**, 295-320.

Delene, D. J., 2011: Airborne data processing and analysis software package. *Earth Science Informatics*, **4**, 29-44.

Del Genfo, A. D., A. A. Lacis, and R. A. Ruedy, 1991: Simulations of the effect of a warmer climate on atmospheric humidity. *Nature*, **351**, 382-385.

Del Genio, A. D., J. Wu, and Y. Chen, 2012: Characteristics of mesoscale organization in WRF simulations of convection during TWP-ICE. *J. Climate*, **25**, 5666-5688

Droegemeier, K.K. and R. B. Wilhelmson, 1987: Numerical simulation of thunderstorm outflow dynamics. Part I: Outflow sensitivity experiments and turbulence dynamics. *J. Atmos. Sci.*, **44**, 1180-1210.

Dudhia, J., 1989: Numerical study of convection observed during the winter monsoon experiment using a mesoscale two-dimensional model. *J. Atmos. Sci.*, **46**, 3077-3107.

Engerer, N. A., D. J. Stensrud, and M. C. Coniglio, 2008: Surface characteristics of observed cold pools. *Mon. Wea. Rev.*, **136**, 4839-4849.

Feng, Z., X. Dong, B. Xi, C. Schumacher, P. Minnis, and M. Khaiyer, 2011: Top-of-atmosphere radiation budget of convective core/stratiform rain and anvil clouds from deep convective systems, *J. Geophys. Res.*, **116**, doi:10.1029/2011JD016451.

Fovell, R. G. and P. S. Dailey, 1995: The temporal behavior of numerically simulated multicell-type storms. Part I. Modes of behavior. *J. Atmos. Sci.*, **52**, 2073-2095.

Fovell, R. G., and Y. Ogura, 1988: Numerical simulation of a midlatitude squall line in two dimensions. *J. Atmos. Sci.*, **45**, 3846– 3879.

Fritsch, J. M., and R. E. Carbone, 2004: Improving quantitative precipitation forecasts in the warm season: A USWRP research and development strategy. *Bull. Amer. Meteor. Soc.*, **85**, 955–965.

Futyan, J. M., and A. D. Del Genio, 2007: Deep convective system evolution over Africa and the tropical Atlantic. *J. Climate*, **20**, 5041-5060.

Gilmore, M. S., J. M. Straka, and E. N. Rasmussen, 2004: Precipitation uncertainty due to variations in precipitation particle parameters within a simple microphysics scheme. *Mon. Wea. Rev.*, **132**, 2610-2627.

Han, M., S. A. Braun, T. Matsui, and C. R. Williams, 2013: Evaluation of cloud microphysics schemes in simulations of a winter storm using radar and radiometer measurements, *J. Geophys. Res. - Atmos.*, **118**, 1401–1419.

Hauser, D., F. Roux, and P. Amayenc, 1988: Comparison of two methods for the retrieval of thermodynamic and microphysical variables from Doppler radar

measurements: Application to the case of a tropical squall line. *J. Atmos. Sci.*, **45**, 1285-1303.

Heymsfield, A. J., A. Bansemer, C. Schmitt, C. Twohy, and M. R. Poellot, 2004: Effective ice particle densities derived from aircraft data. *J. Atmos. Sci.*, **61**, 982-1003.

Hong, S. Y., J. Dudhia, and S. H. Chen, 2004: A revised approach to ice microphysical processes for the bulk parameterization of clouds and precipitation. *Mon. Wea. Rev.*, **132**, 103-120.

Hong, S. Y., and J.- O. Lim, 2006: The WRF single-moment 6-class microphysics scheme (WSM6). *J. Korean Meteor. Soc*, **42**, 129-151.

Houze Jr, R. A., 1982: Cloud clusters and large-scale vertical motions in the tropics. *J. Meteor. Soc. Japan*, **60**, 396-410.

Houze, R. A., 1989: Observed structure of mesoscale convective systems and implications for large-scale heating. *Quart. J. Roy. Meteorol. Soc.*, **115**, 425-461.

Houze, R. A., 2004: Mesoscale convective systems. *Reviews of Geophysics*, **42**.

James, R. P., P. M. Markowski, and J. M. Fritsch, 2006: Bow echo sensitivity to ambient moisture and cold pool strength. *Mon. Wea. Rev.*, **134**, 950-964.

Janjic, Z. I., 1990: The step-mountain coordinate: Physical package. *Mon. Wea. Rev.*, **118**, 1429-1443.

Jensen, M. P., and A. D. Del Genio, 2003: Radiative and microphysical characteristics of deep convective systems in the tropical western Pacific. *J. Appl. Meteor.*, **42**, 1234-1253.

Jensen, M. P., A. Y. Hou, W. A. Petersen, P. Kollias, A. D. Del Genio, B. Orr, SA. Rutledge, MR. Schwaller, and E. Zipser, 2010: Midlatitude Continental Convective Clouds Experiment (MC3E) science plan. U. S. Department of Energy Doc. DOE/SC-ARM/10-004, 31 pp.

Kain, J. S., 2004: The Kain–Fritsch convective parameterization: an update. *J. Appl. Meteor.*, **43**, 170-181.

Kessler, E., 1969: *On the distribution and continuity of water substance in atmospheric circulations. Meteor. Monogr., No.* 32, Amer. Meteor. Soc., 84 pp.

Klazura, G. E., and D. A. Imy, 1993: A description of the initial set of analysis products available from the NEXRAD WSR-88D system. *Bull. Amer. Meteor. Soc.*, **74**, 1293-1311.

Korolev, A. V., J. W. Strapp, G. A. Isaac, and A. N. Nevzorov, 1998: The Nevzorov airborne hot-wire LWC-TWC probe: Principle of operation and performance characteristics. *Journal of Atmospheric and Oceanic Technology*, **15**, 1495-1510.

Lafore, J. P., and M. W. Moncrieff, 1989: A numerical investigation of the organization and interaction of the convective and stratiform regions of tropical squall lines. *J. Atmos. Sci.,* **46**, 521-544.

Lang, S. E., W-K. Tao, X. Zeng and Y. Li, 2011: Reducing the Biases in Simulated Radar Reflectivities from a Bulk Microphysics Scheme: Tropical Convective Systems. *J. Atmos. Sci.,* **68**, 2306-2320.

Leary, C. A., and R. A. Houze Jr., 1979: Melting and evaporation of hydrometeors in precipitation from the anvil clouds of deep tropical convection. *J. Atmos. Sci.,* **36**, 669-679.

LeMone, M. A., G. M. Barnes, and E. J. Zipser, 1984: Momentum flux by lines of cumulonimbus over the tropical oceans. *J. Atmos. Sci.*, **41**, 1914-1932.

Li, X., W.-K. Tao, A. P. Khain, J. Simpson and D. E. Johnson, 2009: Sensitivity of a Cloud-Resolving Model to Bulk and Explicit Bin Microphysical Schemes. Part I: Comparisons. *J. Atmos. Sci.*, **66**, 3-21.

Lim, K-S. S., and S.-Y. Hong, 2010: Development of an effective double-moment cloud microphysics scheme with prognostic cloud condensation nuclei (CCN) for weather and climate models. *Mon. Wea. Rev.*, **138**, 1587-1612.

Lin, Y., and B. A. Colle, 2011: A New Bulk Microphysical Scheme That Includes Riming Intensity and Temperature-Dependent Ice Characteristics. *Mon. Wea. Rev.*, **139**, 1013-1035.

Lin, Y., and K. E. Mitchell, 2005: The NCEP stage II/IV hourly precipitation analyses: Development and applications. *Preprints, 19th Conf on Hydrology*, San Diego, CA, Amer. Meteor. Soc., CD-ROM, 1.2.

Lin, Y. L., R. D. Farley, and H. D. Orville, 1983: Bulk parameterization of the snow field in a cloud model. *Journal of Climate and Applied Meteorology*, **22**, 1065-1092.

Liu, C., M. W. Moncrieff, and E. J. Zipser, 1997: Dynamical influence of microphysics in tropical squall lines: A numerical study. *Mon. Wea. Rev.*, **125**, 2193–2210.

Liu, H. and M. Xue, 2008: Prediction of convective initiation and storm evolution on 12 June 2002 during IHOP. Part I: Control simulation and sensitivity experiments. *Mon. Wea. Rev.*, **136**, 2261-2283.

Mansell, E. R., L. Z. Conrad and C. B. Eric, 2010: Simulated electrification of a small thunderstorm with two-moment bulk microphysics. *J. Atmos. Sci.,* **67**, 171-194.

McCumber, M., W.-K. Tao, J. Simpson, R. Penc, and S.-T. Soong, 1991: Comparison of ice-phase microphysical parameterization schemes using numerical simulations of tropical convection. *J. Appl. Meteor.,* **30**, 985–1004.

Milbrandt, J. A., and M. K. Yau, 2005a: A multimoment bulk microphysics parameterization. Part I: Analysis of the role of the spectral shape parameter. *J. Atmos. Sci.,* **62**, 3051-3064.

Milbrandt, J. A., and M. L. Yau, 2005b: A multimoment bulk microphysics parameterization. Part II: A proposed three-moment closure and scheme description. *J. Atmos. Sci.,* **62**, 3065-3081.

Milbrandt, J. A., and R. McTaggart-Cowan, 2010: Sedimentation-Induced Errors in Bulk Microphysics Schemes. *J. Atmos. Sci.,* **67**, 3931-3948.

Mlawer, E. J., S. J. Taubman, P. D. Brown, M. J. Iacono, and S. A. Clough, 1997: Radiative transfer for inhomogeneous atmospheres: RRTM, a validated correlated-k model for the longwave. *J. Geophys. Res.: Atmospheres*, **102**, 16663-16682.

Morrison, H., 2010: An overview of cloud and precipitation microphysics and its parameterization in models, *WRF Workshop*. 2010, Boulder, CO, NCAR.

Morrison, H., G. Thompson, and V. Tatarskii, 2009: Impact of Cloud Microphysics on the Development of Trailing Stratiform Precipitation in a Simulated Squall Line: Comparison of One- and Two-Moment Schemes. *Mon. Wea. Rev.,* **137**, 991-1007.

Morrison, H., and W. W. Grabowski, 2008: Modeling supersaturation and subgrid-scale mixing with two-moment bulk warm microphysics. *J. Atmos. Sci.,* **65**, 792-812.

Ogura, Y., and Y. L. Chen, 1977: A life history of an intense mesoscale convective storm in Oklahoma. *J. Atmos. Sci.*, **34**, 1458-1476.

Pandya, R., and D. Durran, 1996: The influence of convectively generated thermal forcing on the mesoscale circulation aroundsquall lines, J. Atmos. Sci., **53**, 2924–2951.

Philips, V. T., L. J. Donner, and S. T. Garner, 2007: Nucleation processes in deep convection simulated by a cloud-system-resolving model with double-moment bulk microphysics. *J. Atmos. Sci.*, **64**, 738-768.

Prenni, A. J., DeMott, P. J., Kreidenweis, S. M., Harrington, J. Y., Avramov, A. Verlinde, and P. Q. Olsson, 2007: Can ice-nucleating aerosols affect arctic seasonal climate? *Bull. Amer. Meteor. Soc.*, **88**, 541-550.

Pruppacher, H. R., J. R. Klett, and P. K. Wang, 1998: *Microphysics of clouds and precipitation*. Kluwer Acadenic Publishers, 381-382pp.

Purdom, J. F., 1976: Some uses of high-resolution GOES imagery in the mesoscale forecasting of convection and its behavior. *Mon. Wea. Rev.*, **104**, 1474-1483.

Randall, D. A., M. F. Khairoutdinov, A. Arakawa, and W. W. Grabowski, 2003: Breaking the cloud parameterization deadlock. *Bull. Amer. Meteor. Soc.*, **84**, 1547 – 1564.

Reisner, J., R. M. Rasmussen, and R. Bruintjes, 1998: Explicit forecasting of supercooled liquid water in winter storms using the MM5 model. *Quart. J. Roy. Meteorol. Soc.*, **124**, 1071-1107.

Rotunno, R., J. B. Klemp, and M. L. Weisman, 1988: A theory for strong, long-lived squall lines, *J. Atmos. Sci.*, **45**, 463–485.

Rutledge, S. A., and P. Hobbs, 1983: The mesoscale and microscale structure and organization of clouds and precipitation in midlatitude cyclones. VIII: A model for the "seeder-feeder" process in warm-frontal rainbands. *J. Atmos. Sci.*, ***40***, 1185-1206.

Rutledge, S. A., and R. A. Houze Jr., 1987: A diagnostic modelling study of the trailing stratiform region of a midlatitude squall line. *J. Atmos. Sci.*, **44**, 2640-2656.

Schumacher, C., and R. A. Houze Jr., 2003: Stratiform rain in the Tropics as seen by the TRMM precipitation radar. *J. Climate*, **16**, 1739-1756.

Schmidt, J. M., and W. R. Cotton, 1990: Interactions between upper and lower tropospheric gravity waves on squall line structure and maintenance. *J. Atmos. Sci.*, **47**, 1205-1222.

Skamarock W. C., J. B. Klemp, J. Dudhia, D. O. Gill, D. M. Barker, M. G. Duda, X. Y. Huang, W. Wang and J. G. Powers, 2008: A description of the Advanced Research WRF Version 3. NCAR Tech. Note NCAR/TN-475+STR, 113pp.

Smirnova, T. G., J. M. Brown, S. G. Benjamin, and D. Kim, 2000: Parameterization of cold-season processes in the MAPS land-surface scheme., *J. Geophys. Res.*, **105**, 4077-4086.

Smull, B. F., and R. A. Houze Jr., 1985: A midlatitude squall line with a trailing region of stratiform rain: Radar and satellite observations. *Mon. Wea. Rev.*, **113**, 117-133.

Smull, B. F., and R. A. Houze Jr., 1987: Rear inflow in squall lines with trailing stratiform precipitation. *Mon. Wea. Rev.*, **115**, 2869-2889.

Steiner, M., R. A. Houze Jr., and S. E. Yuter, 1995: Climatological characterization of three-dimensional storm structure from operational radar and rain gauge data, *J. Appl. Meteor.*, **34**, 1978–2007.

Stoelinga, M. T., J. D. Locatelli, and C. P. Woods, 2007: The occurrence of "irregular" ice particles in stratiform clouds. *J. Atmos. Sci.*, **64**, 2740-2750.

Straka, J. M., and J. R. Anderson, 1993: Numerical simulations of microburst-producing storms: Some results from storms observed during COHMEX. *J. Atmos. Sci.*, **50**, 1329-1348.

Sukovich, E. M., D. E. Kingsmill, and S. E. Yuter., 2009: Variability of graupel and snow observed in tropical oceanic convection by aircraft during TRMM KWAJEX. Journal of Applied Meteorology and Climatology, **48**, 185-198.

Szeto, K. K. and H. R. Cho, 1994: A numerical investigation of squall lines. Part II: The mechanics of evolution. *J. Atmos. Sci.*, **51**, 425-433.

Tao, W. K., and J. Simpson, 1989: Modeling study of a tropical squall-type convective line. *J. Atmos. Sci.*, **46**, 177-202.

Tao, W. K., J. Simpson, and M. McCumber, 1989: An ice-water saturation adjustment. *Mon. Wea. Rev.*, **117**, 231-235.

Tao, W.-K., S. Lang, J. Simpson, W. S. Olson, D. Johnson, B. Ferrier, C. Kummerow and R. Adler, 2000: Vertical profiles of latent heat release and their retrieval for TOGA COARE convective systems using a cloud resolving model, SSM/I, and ship-borne radar data. *Journal of the Meteorological Society of Japan*, **78**, 333-355.

Tao, W. K., J. Simpson, C. H. Sui, B. Ferrier, S. Lang, J. Scala, M.-D. Chou, and K. Pickering, 1993: Heating, moisture, and water budgets of tropical and midlatitude squall lines: Comparisons and sensitivity to longwave radiation. *J. Atmos. Sci.*, **50**, 673-690.

Thompson, G., Field, P. R., Rasmussen, R. M., and Hall, W. D., 2008: Explicit forecasts of winter precipitation using an improved bulk microphysics scheme. Part II: Implementation of a new snow parameterization. *Mon. Wea. Rev.*, **136**, 5095-5115.

Thompson, G. P. R. Field, W. D. Hall, and R. M. Rasmussen, 2006: A new bulk microphysical parameterization for WRF (&MM5). *Proc. Seventh Weather Research and Forecasting Model Workshop* (pp. 1-11). 2006, Boulder, CO.

Thorpe, A. J., M. J. Miller, and M. W. Moncrieff, 1982: Two-dimensional convection in non-constant shear: A model of mid-latitude squall lines. *Quart. J. Roy. Meteorol. Soc.,* **108**, 739-762.

Vidaurre, G., J. Hallett, and D. C. Rogers, 2011: Airborne measurement of liquid and total water content. *Journal of Atmospheric and Oceanic Technology*, **28**, 1088-1103.

Wakimoto, R. M., 1982: The life cycle of thunderstorm gust fronts as viewed with Doppler radar and rawinsonde data. *Mon. Wea. Rev.*, **110**, 1060-1082.

Weisman, M. L., W. Wang, and K. Manning, 2009: The use of the RUC DFI initialization for the 2009 WRF-ARW 3 km explicit convective forecasts. *Proceedings of the 10th Weather Research and Forecasting Model Workshop. 2009*, Boulder, CO.

Weverberg K. V. and A. M. Vogelmann, 2012: Sensitivity of Idealized Squall-line simulation to the level of Complexity used in two-moment bulk microphysics schemes. *Mon. Wea. Rev.,* **140**, 1883-1907.

Wilks, D. S., 1995: *Statistical Methods in Atmospheric Sciences*. Academic Press, 467 pp.

Wilson, J. W., and W. E. Schreiber, 1986: Initiation of convective storms at radar-observed boundary-layer convergence lines. *Mon. Wea. Rev.*, **114**, 2516-2536.

Wu, D., X. Dong, B. Xi, Z. Feng, A. Kennedy, G. Mullendore, M. Gilmore,and W.-K. Tao, 2013: Impacts of microphysical scheme on convective and stratiform characteristics in two high precipitation squall line events. *J. Geophys. Res.*, **118**, 11119-11135.

Yao, M. S., and A. D. Del Genio, 1999: Effects of cloud parameterization on the simulation of climate changes in the GISS GCM. *J. Climate*, **12**, *761-799.*

Zelinka, M. D., and D. L. Hartmann, 2010: Why is longwave cloud feedback positive? *J. Geophys. Res.,* **115**, *1984–2012.*